

Real-time monitoring of particulate matter size, concentration, and complex index of refraction

by

Mir Seliman Waez

B.S., Kabul University, 2006
M.S., Kansas State University, 2010

AN ABSTRACT OF A DISSERTATION

submitted in partial fulfillment of the requirements for the degree

DOCTOR OF PHILOSOPHY

Department Mechanical and Nuclear Engineering
College of Engineering

KANSAS STATE UNIVERSITY
Manhattan, Kansas

2019

Abstract

This dissertation focuses on real-time monitoring of particulate matter concentration and sizing, and determining the complex index of refraction of single particles simultaneously. We investigated application of low-cost optical dust sensors GP2Y1010AU0F for monitoring of indoor air quality (IAQ) in buildings; developed a single-particle detector for large, non-absorbing spherical particles so the particles could be sized independently of the refractive index; and developed another sensor to determine the size and complex index of refraction of single particles simultaneously.

We calibrated low-cost optical dust sensors GP2Y1010AU0F using an aerodynamic particle sizer (APS) as a reference instrument. Four sensors were connected in series with the APS and data were collected simultaneously on the downstream of a flow loop where the aerosol concentration was controlled. Sensors' performances were compared to each other as well as to the manufacturer's calibration data. Sensors were also exposed at two different positions in a controlled chamber to collect (1) indoor air data and (2) indoor air data with incense burning; results were compared to the calibration data. Initially, it was found that sensors' data were different from each other by $\pm 15\%$. This percentage was decreased to $\pm 5.9\%$ by adjusting the potentiometer on each sensor. Since the sensors work with light scattering, it was found their outputs were affected by ambient light levels causing uncertainties in the measured values. Sensors' data for indoor air with incense burning were affected by airflow. When connected in series to the APS with 5 L/min airflow passing through them, their data agreed with the calibration data; however, they did not agree when exposed to still air i.e., without airflow.

To determine the size of non-absorbing spherical particles independent of their refractive indices, we found the differential scattering cross-section to be only independent of the real

refractive index at angles near $37 \pm 5^\circ$. We built a device by modifying a Gaussian incident beam profile to a diamond-shaped beam so that the beam transit time of a particle passing through it could determine the true incident intensity for the scattering of the particle. By combining the modified Gaussian incident beam profile with detection of scattered light near $37 \pm 5^\circ$, we demonstrated a refractive-index independent measurement of single spherical particles as they passed through the beam.

In order to simultaneously determine the size and complex index of refraction of single particles, we developed a sensor that measures the scattered-light intensity of particles at three different scattering angles, i.e., $37 \pm 5^\circ$, $80 \pm 5^\circ$, and $115 \pm 5^\circ$, in a diamond-shaped beam. The differential scattering cross-section is only independent of the real part of the refractive index at $37 \pm 5^\circ$; however, in the case of absorbing particles, it depends on the imaginary part. At 115° , particles can be sized independently of the imaginary component; however, at 80° , it depends on both the real and the imaginary components. Although this dependence agrees at several angles, we have chosen 80° because the variation of the differential scattering cross-section at this angle is more consistent compared to other scattering angles.

Real-time monitoring of particulate matter size, concentration, and complex index of refraction

by

Mir Seliman Waez

B.S., Kabul University, 2006
M.S., Kansas State University, 2010

A DISSERTATION

submitted in partial fulfillment of the requirements for the degree

DOCTOR OF PHILOSOPHY

Department of Mechanical and Nuclear Engineering
College of Engineering

KANSAS STATE UNIVERSITY
Manhattan, Kansas

2019

Approved by:

Co-Major Professor
Dr. Christopher M. Sorensen

Approved by:

Co-Major Professor
Dr. Steven J. Eckels

Copyright

© Mir Seliman Waez 2019.

Abstract

This dissertation focuses on real-time monitoring of particulate matter concentration and sizing, and determining the complex index of refraction of single particles simultaneously. We investigated application of low-cost optical dust sensors GP2Y1010AU0F for monitoring of indoor air quality (IAQ) in buildings; developed a single-particle detector for large, non-absorbing spherical particles so the particles could be sized independently of the refractive index; and developed another sensor to determine the size and complex index of refraction of single particles simultaneously.

We calibrated low-cost optical dust sensors GP2Y1010AU0F using an aerodynamic particle sizer (APS) as a reference instrument. Four sensors were connected in series with the APS and data were collected simultaneously on the downstream of a flow loop where the aerosol concentration was controlled. Sensors' performances were compared to each other as well as to the manufacturer's calibration data. Sensors were also exposed at two different positions in a controlled chamber to collect (1) indoor air data and (2) indoor air data with incense burning; results were compared to the calibration data. Initially, it was found that sensors' data were different from each other by $\pm 15\%$. This percentage was decreased to $\pm 5.9\%$ by adjusting the potentiometer on each sensor. Since the sensors work with light scattering, it was found their outputs were affected by ambient light levels causing uncertainties in the measured values. Sensors' data for indoor air with incense burning were affected by airflow. When connected in series to the APS with 5 L/min airflow passing through them, their data agreed with the calibration data; however, they did not agree when exposed to still air i.e., without airflow.

To determine the size of non-absorbing spherical particles independent of their refractive indices, we found the differential scattering cross-section to be only independent of the real

refractive index at angles near $37 \pm 5^\circ$. We built a device by modifying a Gaussian incident beam profile to a diamond-shaped beam so that the beam transit time of a particle passing through it could determine the true incident intensity for the scattering of the particle. By combining the modified Gaussian incident beam profile with detection of scattered light near $37 \pm 5^\circ$, we demonstrated a refractive-index independent measurement of single spherical particles as they passed through the beam.

In order to simultaneously determine the size and complex index of refraction of single particles, we developed a sensor that measures the scattered-light intensity of particles at three different scattering angles, i.e., $37 \pm 5^\circ$, $80 \pm 5^\circ$, and $115 \pm 5^\circ$, in a diamond-shaped beam. The differential scattering cross-section is only independent of the real part of the refractive index at $37 \pm 5^\circ$; however, in the case of absorbing particles, it depends on the imaginary part. At 115° , particles can be sized independently of the imaginary component; however, at 80° , it depends on both the real and the imaginary components. Although this dependence agrees at several angles, we have chosen 80° because the variation of the differential scattering cross-section at this angle is more consistent compared to other scattering angles.

Table of Contents

List of Figures	x
List of Tables	xv
Acknowledgements	xvi
Dedication	xvii
Chapter 1 - Introduction	1
Chapter 2 - Literature Review	5
2.1 Low-Cost Sensors	8
2.1.1 Sharp Dust Sensor	8
2.1.2 Shinyei Model PPD42NS Dust Sensor	9
2.1.3 PMS 1003 Particle Concentration Sensor	11
2.1.4 Low-Cost Optical Particle Counter (OPC)	12
2.2 Particulate-Matter Measuring Equipment	14
2.2.1 Scanning Mobility Particle Sizer (SMPS)	14
2.2.1.1 Condensation Particle Counter (CPC)	15
2.2.1.2 Electrostatic Classifier	16
2.2.2 Aerodynamic Particle Sizer (APS)	18
2.2.3 Optical Particle Sizer (OPS)	19
2.3 Discussion	23
Chapter 3 - Application of Low-Cost Particle Sensors for Air-Quality Monitoring in Buildings	24
3.1 Experimental Setup	25
3.2 Calibration Methods	26
3.3 Calibration Results	27
3.4 Sensors' Data for Indoor Air	29
3.5 Discussion	33
3.6 Conclusions	34
Chapter 4 - A Refractive-Index and Position-Independent Single-Particle Detector for Large, Non-Absorbing Spherical Particles	35
4.1 Correction for the Gaussian Beam	35
4.2 Optimum Scattering Angle for Refractive-Index Independency	39

4.3 Uncertainty Analysis.....	45
4.4 Experimental Setup.....	47
4.5 Results and Discussion	51
4.6 Conclusions.....	56
Chapter 5 - Determination of Size and Complex Index of Refraction of Single Particles	57
5.1 Optimum Scattering Angles.....	57
5.2 Experiments	63
5.2.1 Measuring the Imaginary Part of the Refractive Index, κ	64
5.2.2 Light-Scattering Experimental Setup.....	70
5.3 Results and Discussion	74
5.4 Conclusions.....	86
Chapter 6 - Summary and Conclusions	88
References.....	93
Appendix A - Experimental Data at 37° Scattering Angle	98
Appendix B - Permission from the American Association for Aerosol Research to Reproduce Figures 2.4 and 2.5.....	102
Appendix C - TSI Confirmation to Reuse Figures	103

List of Figures

Figure 2.1 Sharp GP2Y1010AU0F optical dust sensor ("GP2Y1001AU,")	9
Figure 2.2 Shinyei PPD42NS dust sensor ("Specification sheet of PPD42NS,")	10
Figure 2.3 PMS 1003 sensor ("plantower-pms1003-manual_v2-5,")	12
Figure 2.4 Schematic of a low-cost OPC (Gao et al., 2013).....	13
Figure 2.5 Schematic of CPC (Hering, Stolzenburg, Quant, Oberreit, & Keady, 2005).....	15
Figure 2.6 Schematic of TSI electrostatic classifier ("Model 3080-Series Electrostatic Classifiers,").....	17
Figure 2.7 Schematic of TSI aerodynamic particle sizer (APS) ("Aerodynamic Particle Sizer, Model 3321,").....	19
Figure 2.8 Schematic of TSI optical particle sizer (OPS) ("Optical Particle Sizer Model 3330,")	20
Figure 3.1 Experimental setup	25
Figure 3.2 (a) Sharp dust sensor, (b) Sensor container	26
Figure 3.3 Calibration setup.....	27
Figure 3.4 Initial calibration data.....	28
Figure 3.5 Calibration data after adjusting the initial output to 0.6 V	29
Figure 3.6 Controlled chamber	30
Figure 3.7 Baseline for indoor air concentration	30
Figure 3.8 (a) Sensors' data for position A (5 L/min airflow), (b) Calibration data	31
Figure 3.9 (a) Sensors' data for position A (no airflow), (b) Calibration data	32
Figure 3.10 (a) Sensors' data for position B (5 L/min airflow), (b) Calibration data.....	32
Figure 3.11 (a) Sensors' data for position B (no airflow), (b) Calibration data	33
Figure 4.1 Intensity-distribution percentage in a Gaussian laser beam	36
Figure 4.2 Diamond-shaped beam aperture, replotted (Waez et al., 2018)	37
Figure 4.3 Total scattering cross-section for spherical particles scattering light with a wavelength of 0.532 μm , replotted (Waez et al., 2018)	40
Figure 4.4 Average differential-scattering cross-section over a 10° scattering angle for four different refractive indices and three different particle diameters (10,100 and 1000 μm), replotted (Waez et al., 2018).....	41

Figure 4.5 Average differential-scattering cross-section over a 10° scattering angle for four different refractive indices (200-μm particle diameter).....	42
Figure 4.6 Average differential-scattering cross-section over a 10° scattering angle for four different refractive indices (50-μm particle diameter).....	42
Figure 4.7 Average differential-scattering cross-section over a 10° scattering angle for four different refractive indices (20-μm particle diameter).....	43
Figure 4.8 Average differential-scattering cross-section over a 10° scattering angle for four different refractive indices (5-μm particle diameter).....	43
Figure 4.9 Average differential-scattering cross-section over a 10° scattering angle for four different refractive indices (2-μm particle diameter).....	44
Figure 4.10 Average differential-scattering cross-section over a 10° scattering angle for four different refractive indices (1-μm particle diameter).....	44
Figure 4.11 Comparison of actual to predicted differential-scattering cross-sections, replotted (Waez et al., 2018).....	46
Figure 4.12 Uncertainty in predicted particle size, replotted (Waez et al., 2018).....	47
Figure 4.13 Schematic diagram of the experimental setup, dimensions (mm), replotted (Waez et al., 2018).....	48
Figure 4.14 Picture of the experimental apparatus.....	49
Figure 4.15 Portion of the apparatus to show the particles on the ramp.....	49
Figure 4.16 Diamond-shaped aperture.....	50
Figure 4.17 Connection of the devices.....	50
Figure 4.18 Experimental data for 500-μm particles at 37° scattering angle. Each symbol indicates a different particle — (a) BTGC (m = 1.9), (b) glass (m = 1.5), replotted (Waez et al., 2018).....	52
Figure 4.19 Experimental data for 500-μm particles at a 90° scattering angle. Each symbol indicates a different particle — (a) BTGC (m = 1.9), (b) glass (m = 1.5), replotted (Waez et al., 2018).....	53
Figure 4.20 Experimental data for 500-μm particles at five different positions in the beam.....	54
Figure 4.21 Experimental data for 600-μm particles at five different positions in the beam.....	55

Figure 5.1 Average differential-scattering cross-section over a 10° scattering angle for $m = 1.33 + i\kappa$ and three different particle diameters (5-, 17- and 170- μm), the legend in orange is also valid for the same line types in black and green.	58
Figure 5.2 Average differential-scattering cross-section over a 10° scattering angle for $m = 1.5 + i\kappa$ and three different particle diameters (5-, 17- and 170- μm), the legend in orange is also valid for the same line types in black and green.	58
Figure 5.3 Average differential-scattering cross-section over a 10° scattering angle for $m = 1.7 + i\kappa$ and three different particle diameters (5-, 17- and 170- μm), the legend in orange is also valid for the same line types in black and green.	59
Figure 5.4 Average differential-scattering cross-section over a 10° scattering angle for $m = 2 + i\kappa$ and three different particle diameters (5-, 17- and 170- μm), the legend in orange is also valid for the same line types in black and green.	59
Figure 5.5 Variation of coefficient, C_I vs. κkR for particle diameters ($d = 17, 170, \text{ and } 500 \mu\text{m}$), and different refractive indices	60
Figure 5.6 $(dC/d\Omega)/[d^2(\kappa kR)^{-0.38}]$ vs $(n - 0.33)$ at 80° scattering angle for 17-, 170-, and 500- μm particles with $\kappa kR = (0.01, 0.1, 0.3, 1 \ \& \ 3)$	61
Figure 5.7 $(dC/d\Omega)/d^{1.9}$ vs $(n-1)$ at 115° scattering angle for (17-,170- and 500- μm) particles... ..	62
Figure 5.8 Schematic of the setup for measuring κ , (a) without solution, (b) with solution	64
Figure 5.9 Picture of the setup for measuring κ , (a) without solution, (b) with solution.....	65
Figure 5.10 Imaginary part of the refractive index, κ vs. nigrosine solution-to-water concentration ($\kappa \pm 9\%$).....	66
Figure 5.11 Imaginary part of the refractive index, κ vs. nigrosine powder-to-toluene concentration ($\kappa \pm 9\%$).....	67
Figure 5.12 Percent difference between actual and predicted values of κkR for a 100- μm particle with $m = 1.6 + i\kappa$	68
Figure 5.13 κkR vs. droplet diameter for different nigrosine solution-to-water concentrations... ..	69
Figure 5.14 κkR vs. droplet diameter for different nigrosine-to-toluene concentrations	69
Figure 5.15 Schematic diagram of light-scattering experimental setup, dimensions (mm)	70
Figure 5.16 Picture of the light-scattering experimental apparatus	71
Figure 5.17 Portion of the light-scattering experimental apparatus.....	72
Figure 5.18 Portion of the experimental apparatus (top view)	72

Figure 5.19 Portion of the experimental apparatus (side view).....	73
Figure 5.20 Photodiodes outputs vs. time of flight for a 300- μm droplet of nigrosine solution to water (1:150).....	75
Figure 5.21 Photodiodes outputs vs. time of flight for a 300- μm droplet of nigrosine solution to water (1:150).....	75
Figure 5.22 Photodiodes outputs vs. time of flight for a 300- μm droplet of nigrosine solution to water (1:150).....	76
Figure 5.23 Photodiodes outputs vs. time of flight for a 300- μm droplet of nigrosine solution to water (1:150).....	76
Figure 5.24 Photodiodes outputs vs. time of flight for a 300- μm droplet of nigrosine solution to water (1:150).....	77
Figure 5.25 Photodiodes outputs vs. time of flight for a 300- μm droplet of nigrosine solution to water (1:200).....	77
Figure 5.26 Photodiodes outputs vs. time of flight for a 300- μm droplet of nigrosine solution to water (1:200).....	78
Figure 5.27 Photodiodes outputs vs. time of flight for a 300- μm droplet of nigrosine solution to water (1:200).....	78
Figure 5.28 Photodiodes outputs vs. time of flight for a 300- μm droplet of nigrosine solution to water (1:200).....	79
Figure 5.29 Photodiodes outputs vs. time of flight for a 300- μm droplet of nigrosine solution to water (1:200).....	79
Figure 5.30 Photodiodes outputs vs. time of flight for a 220- μm droplet of nigrosine-to-toluene solution (1:1350).....	81
Figure 5.31 Photodiodes outputs vs. time of flight for a 220- μm droplet of nigrosine-to-toluene solution (1:1350).....	81
Figure 5.32 Photodiodes outputs vs. time of flight for a 220- μm droplet of nigrosine-to-toluene solution (1:1350).....	82
Figure 5.33 Photodiodes outputs vs. time of flight for a 220- μm droplet of nigrosine-to-toluene solution (1:1350).....	82

Figure 5.34 Photodiodes outputs vs. time of flight for a 220- μm droplet of nigrosine-to-toluene solution (1:1350).....	83
Figure 5.35 Photodiodes outputs vs. time of flight for a 220- μm droplet of nigrosine-to-toluene solution (1:800).....	83
Figure 5.36 Photodiodes outputs vs. time of flight for a 220- μm droplet of nigrosine-to-toluene solution (1:800).....	84
Figure 5.37 Photodiodes outputs vs. time of flight for a 220- μm droplet of nigrosine-to-toluene solution (1:800).....	84
Figure 5.38 Photodiodes outputs vs. time of flight for a 220- μm droplet of nigrosine-to-toluene solution (1:800).....	85
Figure 5.39 Photodiodes outputs vs. time of flight for a 220- μm droplet of nigrosine-to-toluene solution (1:800).....	85
Figure A.1 Photodiodes outputs for 13 glass beads 500 μm in diameter	98
Figure A.2 Photodiodes outputs for 11 glass beads 500 μm in diameter	99
Figure A.3 Photodiodes outputs for 11 barium titanate glass compound (BTGC) beads 500 μm in diameter.....	99
Figure A.4 Photodiodes outputs for 11 barium titanate glass compound (BTGC) beads 500 μm in diameter.....	100
Figure A.5 Experimental data for 500- μm barium titanate glass compound (BTGC) beads at five different positions in the beam.....	100
Figure A.6 Experimental data for 500- μm glass beads at five different positions in the beam .	101

List of Tables

Table 4.1 Comparison of actual to predicted particle diameters	52
Table 4.2 Comparison of actual to predicted particle diameters for 500- μm particles passed at five different positions	54
Table 4.3 Comparison of actual to predicted particle diameters for 600- μm particles passed at five different positions	55
Table 5.1 Comparison of actual to predicted values of droplet diameter, d , κkR , and n for nigrosine solution-to-water	80
Table 5.2 Comparison of actual to predicted values of droplet diameter, d , κkR , and n for nigrosine-to-toluene solution	86

Acknowledgements

I would like to express my sincere gratitude to my advisors, Dr. Steve Eckels and Dr. Chris Sorensen for their guidance and support in my research during my Ph.D. studies. I would like to thank Dr. Eckels for his continuous help and advice, not only on the academic side but also on the personal side. I would like to express my special thanks to Dr. Sorensen for his extraordinary advice and recommendations. Their support and guidance played a major role toward my Ph.D. degree accomplishment.

I would also like to thank Dr. Ronaldo Maghirang and Dr. Amy Betz for being members of my supervisory committee and for providing their support. Additionally, I would like to thank Dr. Christer Aakeroy for serving as a chairperson on my committee.

This research was funded by the Biosecurity Research Institute (BRI). Its financial support for this project allowed me to pursue my Ph.D. degree, which would not be possible without its funding.

Finally, I would like to thank my friends and family, especially my wife, for their continuous encouragement, and support.

Dedication

To my parents, my wife, my children, and to the rest of my family.

Chapter 1 - Introduction

This dissertation reports on the study and improved accuracy of particle detection, size, and complex index of refraction measurement for particles larger than one micron. Supra-micron particles, often referred to as coarse-mode particles, occur as dust — such as wind-blown mineral dusts that represent the largest mass fraction of aerosol in the Earth’s atmosphere, grain and coal dusts, bio-aerosols, indoor cooking aerosols, large combustion particles from wildfires, and volcanic ash. Given their prevalence, it is important to be able to detect and accurately measure the size and index of refraction of the particles because particulate matter (PM) has adverse effects on human health (Kelly et al., 2017; Pope , Ezzati , & Dockery 2009), and harm to human beings from PM is related to its size (Tianhua & Ying, 2014) as well as to its type and material (composition). According to the United States Environmental Protection Agency (EPA), particles of sizes 10 μm in diameter or less (PM_{10}) are the most harmful for human health. PM causes various respiratory and cardiovascular diseases when there is long-term exposure to it (Gorai, Tuluri, & Tchounwou, 2014; Nandasena, Wickremasinghe, & Sathiakumar, 2012). For example, it can cause problems such as decreased lung function, lung cancer, heart attack, irregular heartbeat, asthma, irritation of the airways, coughing, and difficulty breathing.

Type and material of PM in optical systems can be predicted by determining its index of refraction, which is defined as the ratio of the speed of light in a vacuum to the speed of light in a particular material. Once aerosol particles are illuminated by a beam of light, they scatter and absorb some of that light, thereby diminishing the intensity of the beam (Hinds, 1999). While all aerosol particles scatter light, only those made of absorbing material will absorb light. Therefore, the index of refraction will have two components, i.e., $m = n + i\kappa$. The real component, n , is related to the scattering, while the imaginary component, κ , is related to absorption. A non-absorbing

material, e.g., glass, will only have the real component; however, an absorbing material, e.g., mineral dust, will have both the real and imaginary components.

The research in this dissertation comes from our peer-reviewed journal papers and conference papers, which are divided into three main chapters. In Chapter 3, we demonstrate the application of low-cost particle sensors for air-quality monitoring in buildings by calibration of low-cost particulate sensors using an aerodynamic particle sizer (APS) as a reference instrument. In Chapter 4, we have built a refractive-index and position-independent single-particle detector for large, non-absorbing spherical particles by obtaining an optimum scattering angle of $37 \pm 5^\circ$ for refractive index independency and making a correction for the Gaussian laser beam profile by considering a diamond-shaped beam aperture so that time of flight of the particle passing through the beam can control the precise position of the particle in the beam. In Chapter 5, we have developed a sensor that determines the size and complex index of refraction of single particles simultaneously by measuring the scattered-light intensity of particles at three different scattering angles, i.e., $37 \pm 5^\circ$, $80 \pm 5^\circ$, and $115 \pm 5^\circ$.

In considering the scattered-light intensity at three angles, we have developed three mathematical models so that we could solve for the three unknowns, i.e., particle size, and real and imaginary components of the refractive index. At 37° and 115° , the differential-scattering cross-section of a particle is relatively independent of the real and the imaginary components, respectively; however, at 80° , it depends on both the real and the imaginary components. Although this dependence agrees at several different angles, we have chosen 80° because the variation of the differential scattering cross-section at this angle is more consistent compared to other scattering angles.

This research is useful in a variety of applications such as designing new PM sensors with low-cost, accurate particle sizing and complex refractive index determination capability; sorting and identifying type and material of poly-disperse solid particles to get highly mono-disperse particles out of them and reducing their production costs; and sizing fuel particles that can be used in advanced nuclear reactors.

One of the most important applications of our research can be detection of PM in bleed air of aircraft. Bleed air is brought into the cabin in order to maintain the quality of the air for passenger and crew health and comfort. It has been reported on several occasions that bleed air can be contaminated by oil due to oil-seal leaks in the compressor. The particulates could be potentially hazardous oil droplets from the oil-seal leaks, water droplets due to the presence of fog generated by the cooling system, and so on. Health effects for passengers and crew during these incidents are diverse, ranging from eye and throat irritation and blurred vision to disorientation, nausea, vomiting, dizziness, or even loss of consciousness (Winder & Balouet, 2001). When the contamination is high, it creates a fume event that emits an obvious odor, or sometimes visible smoke or mist in the aircraft (Jones, Amiri, Roth, Hosni, & 2017).

To provide air representative of oil-contaminated bleed air, a bleed-air simulator was developed to show what would be expected in the case of aircraft cabin contamination (Eckels, Jones, Mann, Mohan, & Weisel, 2014). To analyze and characterize the contaminants that would likely be present in the bleed air during an incident, multiple papers have been published identifying chemicals present in the oil, and discussing their health risks and effects (Bartl, Völkl, & Kaiser, 2008; Chris van Netten, 2005; Winder & Balouet, 2002). Moreover, volatile organic compounds (VOCs) generated by the pyrolysis of the lubricating oil at high temperatures expected

in the bleed-air system have been studied and identified as well (C. van Netten, 1999; C. van Netten & Leung, 2000, 2001).

While considerable work has been done to improve air quality in aircraft cabins by identifying and characterizing contaminants that would be present in the bleed air, as mentioned above, real-time detecting, sizing, and distinguishing the type and material of single particles in bleed air is still missing from the bulk of research. Therefore, one might use our newly developed device to detect, size, and identify the type and material of PM on a real-time basis in bleed air. Considering the health effects of PM present in bleed air, this will help the cabin crew members make the right decision on whether or not an emergency landing is required should an incident with cabin air occur.

Chapter 2 - Literature Review

Airborne and inhalable particulate matter (PM) of various sizes is widely found in the environment. PM is the major contributor to indoor and outdoor air pollution and can be either in the form of liquid droplets or dry dust in a variety of sizes and shapes, as well as a wide range of physical and chemical properties (Cooper & Alley, 2010). It is also classified as one of the criteria pollutants by the National Ambient Air Quality Standards (NAAQS). PM has significant effects on human health. According to the U.S Environmental Protection Agency (EPA), particles of sizes 10 μm or less (PM_{10}) are the most harmful for human health as they can pass into the lungs. The smaller the particle size the greater the risk of them getting into the respiratory system. Once the particles are in the lungs, they can cause various kinds of health problems such as decreased lung function, heart attack, irregular heartbeat, asthma, irritation of the airways, coughing, and difficulty breathing. Moreover, polluted brain is another health concern that can occur from air pollution (Underwood, 2017).

To measure PM size and concentration, various technologies have been used. For example, light-scattering is the most common technology used for this purpose. The application of light-scattering to measure particle sizes began more than a century ago. Mie (1908) developed the basic theory for scattering by spheres. Following the Mie theory, early optical particle counters (OPCs) were developed. Gucker, O'Konski, Pickard, and Pitts (1947) built the first modern OPC in 1940s. Since then, there have been gradual improvements in this field. For example, X. Wang et al. (2009) described a light-scattering instrument that combined photometry and single-particle sizing into one optical device that could detect photometric signal and single-particle scattering at the same time, but analyzed only one of the mentioned signals. While previous studies have

explored a variety of particle-sizing technologies, little is known about determination of the refractive index of PM, especially for single particles.

The estimation of the optical properties and particle-size distributions has attracted considerable attention in the recent years. Some techniques have been developed to predict particle-size distribution and index of refraction (Kolgotin, Müller, Chemyakin, & Romanov, 2016; Pfeifer et al., 2014; Ren, Qi, Chen, Ruan, & Tan, 2015; Ren, Qi, Yu, & Ruan, 2017; Sun, Tang, & Dai, 2007; Ye et al., 1999; Zarzana, Cappa, & Tolbert, 2014; Zhu et al., 2011). Kolgotin et al. (2016) developed an explicit method to determine optical constants (complex refractive indices) of aerosols based on the measurement data of Lidar, but the particle-size distribution was assumed to be known. Eidhammer, Montague, and Deshler (2008) developed a twin-angle optical particle counter (OPC) that measured forward scattering at 40° and 74° to determine particle size and refractive index, respectively. They used the aerosol particle number concentration ratio at 40° and 74° to determine the complex index of refraction, but their method could give only an average complex index of refraction for a sample containing many particles. Measurement uncertainties for size here were between 4% and 10% for particles greater than $3\ \mu\text{m}$ in diameter. This uncertainty was measured for a small range of refractive indices, i.e., 1.35 – 1.60. However, for a larger range of refractive indices, for example, 1.33 – 3.0, the range of uncertainty would be larger as well. According to Budde, El Masri, Riedel, and Beigl (2013), even certified optical measurements show a deviation of within $\pm 10\%$ uncertainty.

Likewise, Hu, Li, Zhang, and Li (2006) developed a dual-scattering-angle optical particle counter that measured light-scattered intensities at 60° and 90° , and thus it was called $60^\circ + 90^\circ$ OPC. Their device measured the imaginary part of the refractive index by predicting the particle number ratio at two angles. A multi-angle, aerosol spectrometer probe (MASP) was developed by

Baumgardner et al. (1996) that collected scattered light from each particle passing through a focused laser beam over two discrete regions of forward ($30^\circ - 60^\circ$) and backward ($120^\circ - 150^\circ$) scattering angles. The MASP used the ratio of the forward and back-scattered light and their sum (total scattering) as a unique function of particle size and index of refraction. Using this combination, first an average refractive index was determined and then the refractive index was used to convert the total scattering to a diameter. With these devices, there was not enough evidence of how they picked these scattering angles. A study by Ebert, Weinbruch, Hoffmann, and Ortner (2004) determined the chemical composition and average complex refractive index of rural and urban aerosol particles by total x-ray fluorescence and high-resolution scanning electron microscopy. First they analyzed the chemical composition of each material and classified these into different particle groups of known indices of refraction. Then the average complex index of refraction was determined by summing the product of the refractive index and volume of each particle group and dividing them by the total volume, i.e., sum of the volume of each particle group.

Currently, most optical particle-sizing instruments from expensive to low-cost sensors are used to measure the size and concentration of PM. An important aspect of any optical detector is to know the incident intensity on the particle. Most light sources, a laser beam for example, have an intensity profile across the beam. For many laser sources, the profile is Gaussian. Thus the position of the particle in that profile must be known and controlled. To determine the position of the particle in the beam and accurately size the particle, Waez, Eckels, and Sorensen (2018) modified the Gaussian laser beam into a diamond-shaped beam at which the position of the particle was controlled by the beam transit time. Some advanced instruments introduce a sheath flow to keep the particle stream centered as it passes through the beam. The disadvantage of sheath flow

is that it can contribute to the dilution of the actual aerosol concentration and it adds cost to the detector. Another tactic is to detect the scattered light at two or more angles and then use the ratio of the scattering for size determination; see, for example, the work of (Hirleman Edwin D, 1980). The ratio eliminates the uncertainty of the incident intensity. The drawback with these particle-sizing techniques is that the predicted particle size may vary significantly from reality due to the dependence of light-scattering on the refractive index.

In order to detect particulate matter and improve air quality, some applications with complex and expensive systems have been used to precisely measure PM mass concentration and number concentration in air. However, portable and low-cost particle sensors are available and have recently become popular for monitoring air quality. Johnson, Bergin, Russell, and Hagler (2016) used some of these low-cost sensors to measure ambient PM concentrations and on-road emissions factors, and found them to be potentially useful for high-concentration applications in developing countries and for use in generating emission factors. The low-cost sensors are not only cheaper but also more compact compared to other conventional particle-detection methods. Since the expensive devices are more accurate than low-cost sensors, they are commonly used as reference instruments in evaluation and calibration of low-cost sensors. Some of these low-cost sensors and expensive instruments are briefly discussed as follows.

2.1 Low-Cost Sensors

2.1.1 Sharp Dust Sensor

The Sharp dust sensor, “GP2Y1010AU0F,” is an optical-sensing device used to detect house dust, smoke, etc. An infrared-emitting diode (IRED) and a phototransistor are diagonally

arranged into this device. It detects the reflected light of dust in air. Figure 2.1 shows a picture of this sensor.



Figure 2.1 Sharp GP2Y1010AU0F optical dust sensor ("GP2Y1001AU,")

Dimensions of this device are 46.0 x 30.0 x 17.6 mm. It operates with a supply voltage of 4.5 to 5.5 V and a current of 20 mA. It has a pulse cycle of 10 ± 1 ms with a pulse width of 0.32 ± 0.02 ms. Presence of dust can be detected by the photometry of only one pulse with a sensitivity of $0.5 \text{ V}/(0.1 \text{ mg}/\text{m}^3)$. Also, it should be noted, when the inside of the sensor is moisturized, it does not maintain its proper function. Therefore, it is important to design the application so there is no moisturization of the sensor.

2.1.2 Shinyei Model PPD42NS Dust Sensor

The Shinyei particle sensor, “PPD42NS,” is an optical-sensing device used to create digital (LO-Pulse) output to PM. LO-Pulse occupancy time (LPO time) is in proportion to PM

concentration. The output is for PM around 1 micro meter or larger in size. A light beam is provided by an infrared LED that is in diagonal arrangement to the phototransistor. Light scattered by particles is detected by a PIC1 photodiode. The picture of this sensor is shown in Figure 2.2.



Figure 2.2 Shinyei PPD42NS dust sensor ("Specification sheet of PPD42NS,")

Dimensions of this device are 59 x 45 x 22 mm. Its detectable range of concentration is 0 to 28,000 pcs/liter with a pulse-width range of 10 ms to 90 ms. It operates with a supply voltage of DC 5V \pm 10% and a current of 90 mA. Time for stabilization is 1 minute after the power is turned on. The operating humidity range for this device is 95% rh or less (without dew condensation).

Both GP2Y1010AU0F (GP2Y) and PPD42NS (PPD) sensors were evaluated experimentally (Austin, Novosselov, Seto, & Yost, 2015; Y. Wang et al., 2015). It was found these sensors may not be as accurate as more complicated and expensive PM measurement devices in clean environments. Experiments have shown the sensors' performances can be increased when there is an active airflow passing through them, especially in clean environments. Tianhua and

Ying (2014) modified the original design of GP2Y1010AU0F by considering an electrical fan to circulate air through its airflow channel. The fan caused every dust particle in the air stream to pass through the sensing volume. Relying on these newly available off-the-shelf sensors may greatly improve our capacity to characterize aerosol concentrations with high spatial and temporal resolution and low system cost, especially when many such devices can be deployed concurrently (Holstius, Pillarisetti, Smith, & Seto, 2014).

2.1.3 PMS 1003 Particle Concentration Sensor

PMS 1003 is a particulate-matter concentration sensor that measures particle number concentrations in the air. It has a fan that draws the air sample into the sensor and a laser that illuminates particles passing through the scattering chamber. Then the scattered light by particles is collected in a certain degree. Once the scattered light is collected, equivalent particle diameter and particle number concentration can be calculated based on the MIE theory ("plantower-pms1003-manual_v2-5,").

According to the manufacturer, this sensor can detect particle sizes in the range of 0.3 – 10 μm in diameter with a counting efficiency of 50% for 0.3 μm and 98% for particles greater than 0.5 μm . It reports particle counts in five bins with mean sizes of 0.3, 0.5, 1, 2.5, 5, and 10 μm . It requires a DC power supply of 5 ± 0.5 volts. Working temperature range of this device is -10~+60 $^{\circ}\text{C}$. Its dimensions are 65 x 42 x 23 mm. The PMS 1003 sensor is commercially available with a relatively low price of less than \$50. Figure 2.3 shows the picture of this device.



Figure 2.3 PMS 1003 sensor ("plantower-pms1003-manual_v2-5,")

The PMS 1003 sensor was evaluated in a laboratory by Kelly et al. (2017), and it was found the sensor underestimates particle counts by a factor of 80% or more compared to GRIMM for PM smaller than 10 μm in diameter, but slightly overestimates particle counts compared to GRIMM at the 10- μm size bin by a factor of 2.5.

2.1.4 Low-Cost Optical Particle Counter (OPC)

Optical particle counters are conventionally used to detect particles and provide number concentration of PM in specific size ranges. The design and schematic of a low-cost OPC is shown in Figure 2.4 (Gao et al., 2013).

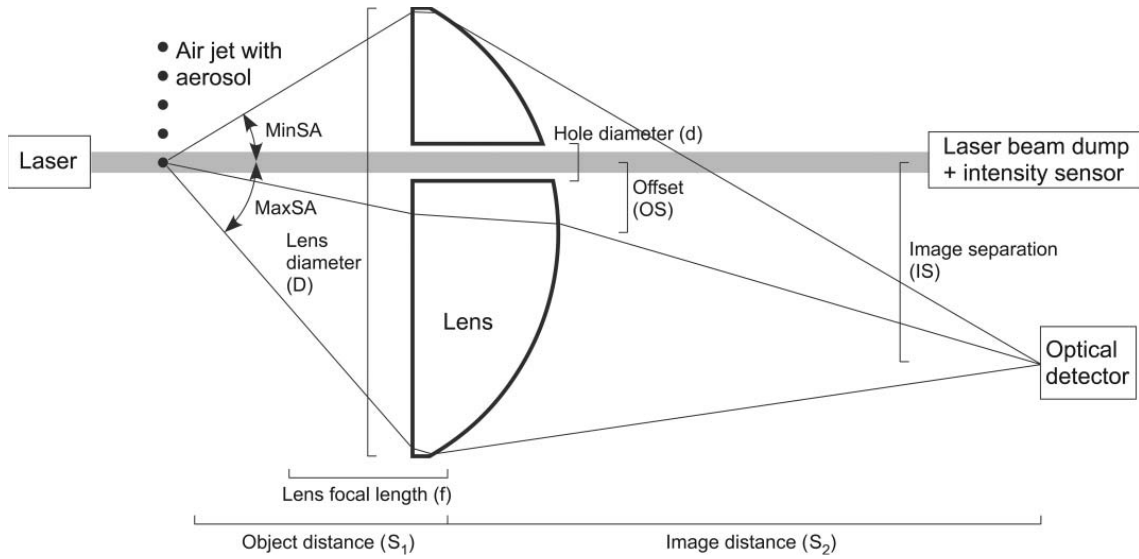


Figure 2.4 Schematic of a low-cost OPC (Gao et al., 2013)

Reproduced with permission from the American Association for Aerosol Research

In this design, a laser beam crosses an imaging lens parallel to its optical axis via a hole drilled on the lens. The hole is located off-axis from the lens optical axis. The direct laser beam light is passed through the hole, which is then collected by a beam dump. Particles are passing through the laser beam outside the lens' focal plane. Laser light forward-scattered by a particle is imaged to a point that is offset from the laser beam. An optical detector detects the scattered light at the image point. If the refractive index of the particle is known, the scattered-light signal can be related to the size of the particle (Gao et al., 2013).

In low-cost sensors, particles move to the sensitive volume without any control over the aerosol sample. In a study by Y. Wang (2014), it was assumed that particles had passed through the center of the beam. However, if a small particle passes through the center of the beam and a large particle passes through the edge of the beam, their light-scattered intensity will be comparable, which makes it difficult to accurately size the particle. This problem with a laser system is due to the Gaussian intensity distribution in the beam.

In a Gaussian laser beam, the intensity of the beam decreases with radius. As a result, large particles travelling through the edge of the beam and small particles travelling through the center of the beam will have similar scattered intensities (Mallik, 2014). Therefore, it will be difficult to accurately size the particles. To overcome this problem, Waez et al. (2018) made a correction for the Gaussian beam by using a diamond-shaped aperture, which could detect and size each single particle independent of the beam position and index of refraction.

2.2 Particulate-Matter Measuring Equipment

In order to properly measure particles, it is important to not only detect the existence of particles but also determine their sizes (Roth, 2015). Although it is not easy to accurately size the particles, even using the more expensive devices, some statistical analysis can be done to counter for possible errors that may arise due to accuracy and resolution of the equipment, and corrections can be made accordingly.

2.2.1 Scanning Mobility Particle Sizer (SMPS)

The SMPS is regarded as the gold standard for submicron aerosol size-distribution measurement (HEE-SIEW, 2014). It measures particle-size distribution in the range of 10 nm to 1 μm , based on the particles' electric mobility. It gives the particles an electric charge and passes them through an electric field to separate them into streams of like diameter (Mann, Eckels, & W. Jones, 2014). Then a separate condensation particle counter (CPC), which condenses butanol, counts the particle-number concentration in each diameter by measuring the reflected light. An SMPS is basically composed of an electrostatic classifier (EC) and a CPC.

2.2.1.1 Condensation Particle Counter (CPC)

Condensation particle counters (CPCs) have been used for many decades to measure airborne particle number concentrations (Mordas et al., 2005). These instruments enlarge particles by condensation so they can be detected optically. The CPC measures the particle-number concentration. A schematic of this device is shown in Figure 2.5.

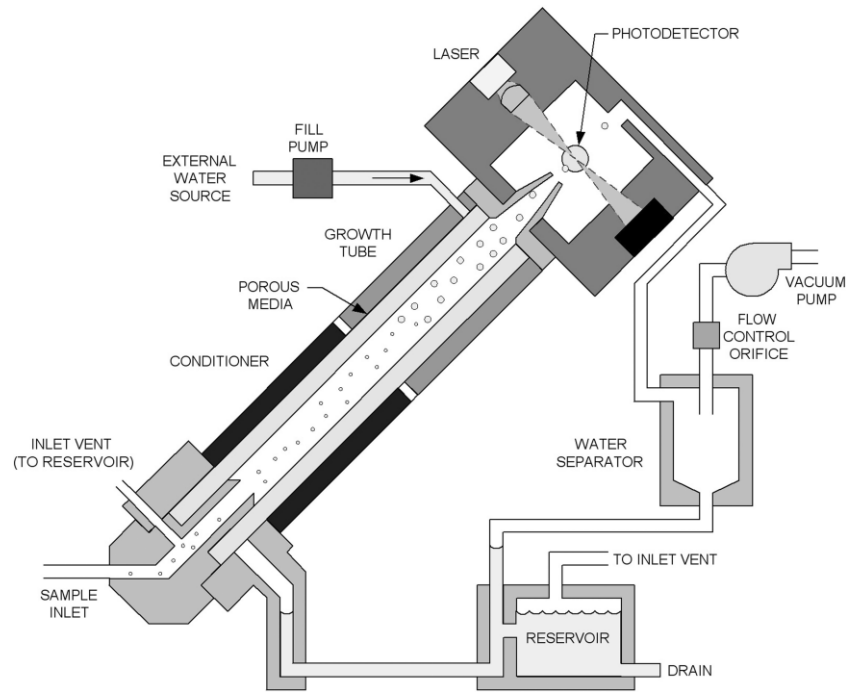


Figure 2.5 Schematic of CPC (Hering, Stolzenburg, Quant, Oberreit, & Keady, 2005)

Reproduced with permission from the American Association for Aerosol Research

This device has an inlet, conditioner, growth tube, and optical head. The conditioner is used to normalize the temperature and relative humidity of the entering airflow. The growth tube is used to enlarge the particles. The grown particles are detected optically by passing them through the waist of a focused laser beam. Light scattered from the particles is collected by an elliptical mirror and is focused onto a silicon photo-detector. A water separator drains the flow to a reservoir. The

flow is monitored by a pressure transducer that measures the pressure drop across the downstream metering orifice where the temperature is held constant (Hering et al., 2005). The CPC (TSI Model 3775) detects particle sizes in the range of 4 nm to 3 μm in diameter. The uncertainty of this device specified by the manufacturer is $\pm 10\%$ at $< 5 \times 10^4$ particles/ cm^3 and $\pm 20\%$ at $< 5 \times 10^7$ particles/ cm^3 .

2.2.1.2 Electrostatic Classifier

An electrostatic classifier separates submicron particle sizes in the range of 10 to 1000 nm in diameter from the incoming aerosol sample. The separation is performed in a series of steps until finally reaches to a nearly monodisperse aerosol sample. The separated aerosol particles then exit the electrostatic classifier and pass into a condensation particle counter that measures the particle-number concentration. The basic component of an electrostatic classifier is the differential mobility analyzer (DMA) that selects particles of a specific size out of the aerosol sample. Another component of the electrostatic classifier is the impactor, which has one or a series of impaction plates where the larger particles are separated out due to their higher inertia. Then only the smaller particles will be able to follow the aerosol streamline. Figure 2.6 shows a schematic of the electrostatic classifier.

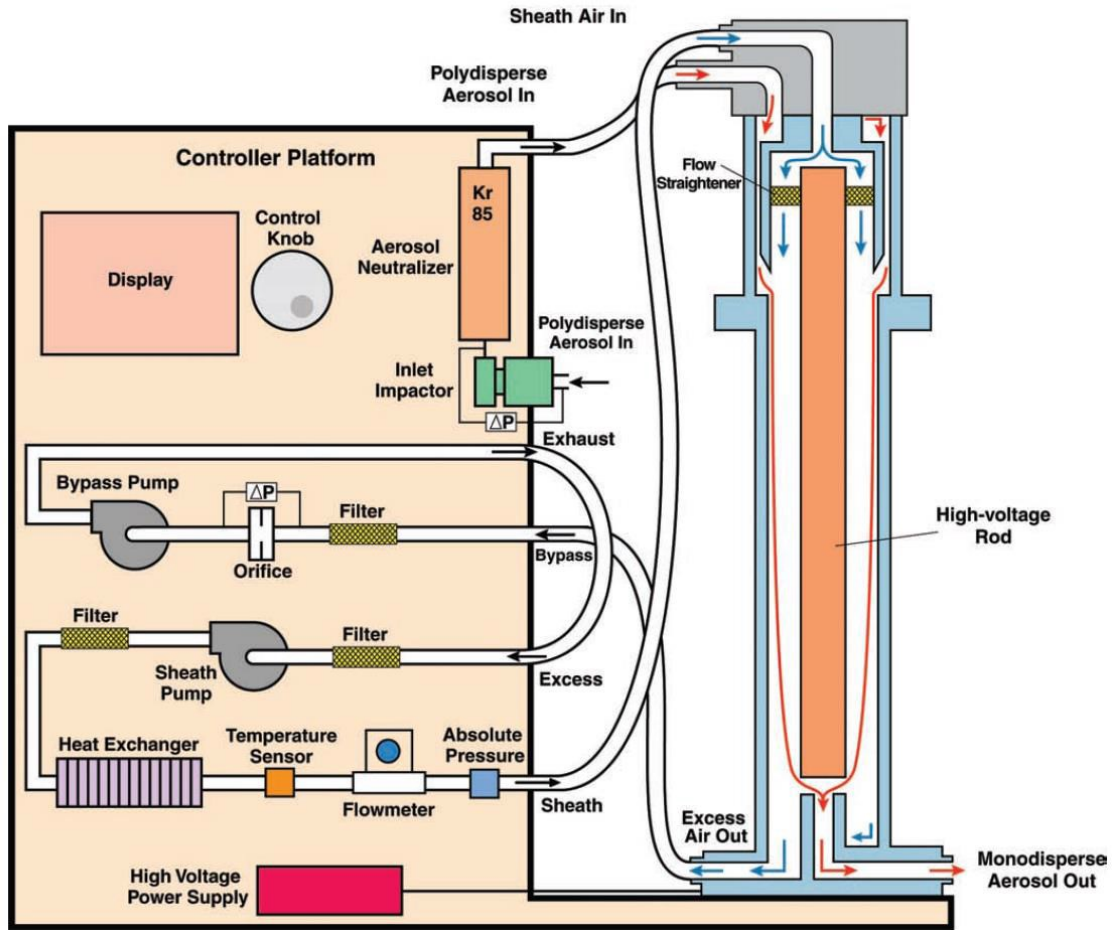


Figure 2.6 Schematic of TSI electrostatic classifier ("Model 3080-Series Electrostatic Classifiers,")

Once the larger particles are separated out, the aerosol is passed through a radioactive bipolar charger where the particles get either single positive, single negative, or zero charge. The particles then enter the DMA and are separated according to their electric mobility ("Model 3080-Series Electrostatic Classifiers,"). The DMA has an inner cylinder connected to a negative-power supply source that affects the trajectory of the charged particles. This cylinder has a repulsive force for the negatively charged particles, which makes them go on the outer wall. Only particles with positive charge get into the negatively charged cylinder where they can follow the correct path and exit as monodisperse aerosol.

The electrostatic classifier can size particles in the range of 10 to 1000 nm in diameter with a maximum input concentration of 10^8 particles/cm³. It displays the data output up to 64 channels. According to the manufacturer, uncertainties are between 3 to 3.5 % for sizing.

2.2.2 Aerodynamic Particle Sizer (APS)

An aerodynamic particle sizer (APS) measures the size distribution and concentration of particles in the size range of 0.5 μm to 20 μm in diameter with uncertainties of $\pm 10\%$ for concentration reading and $\pm 0.03 \mu\text{m}$ for sizing as specified by the manufacturer ("Aerodynamic Particle Sizer, Model 3321,"). It records the time of flight from the light-scattering intensity of each particle as it passes through two laser beams in an accelerated flow field. Then the time of flight is converted into an aerodynamic particle size. The particle size is binned into 52 channels on a logarithmic scale. A sheath flow keeps the particles flow-centered as they pass through the focused laser beams. The maximum recommended particle concentration for this instrument is 1,000 particles/cm³ at 0.5 μm with less than 5% coincidence, and the same maximum concentration is true at 10- μm particle size with less than 10% coincidence. A schematic of this device is shown in Figure 2.7.

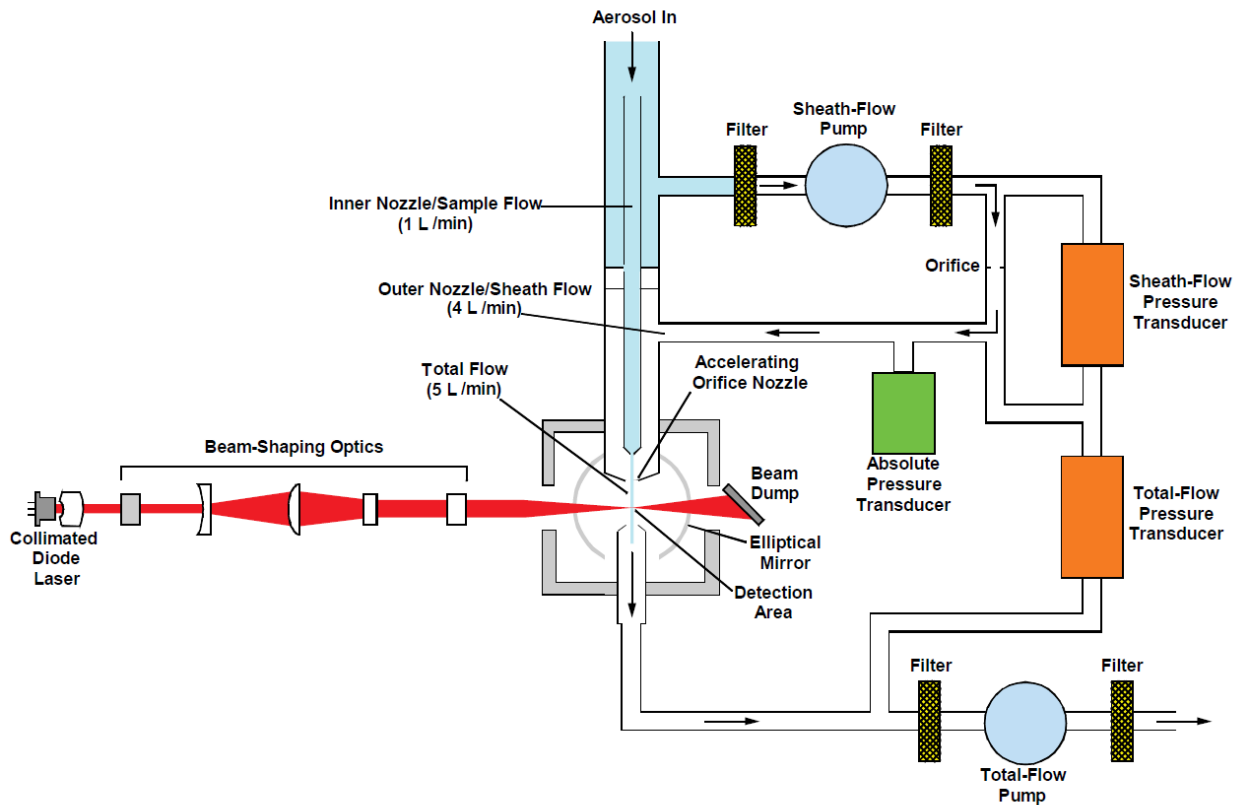


Figure 2.7 Schematic of TSI aerodynamic particle sizer (APS) ("Aerodynamic Particle Sizer, Model 3321,")

2.2.3 Optical Particle Sizer (OPS)

The optical particle sizer (OPS) is an instrument that measures aerosol mass and/or number concentrations in the size range of 0.3 – 10 μm in diameter in up to 16 user-adjustable size channels. Its concentration measurement range is 0 to 3,000 particles/ cm^3 . The particle density and refractive index can be adjusted by the user. It takes an aerosol sample of 1.0 L/min and a sheath air-flow rate of 1.0 L/min. The sheath air is used to stabilize and focus the aerosol in order to enhance the size resolution. The focused aerosol passes through the laser beam and scatters light. An elliptical mirror collects the scattered light at a $90^\circ \pm 60^\circ$ scattering angle and focuses it on a

photo detector. The particles are then counted and sized based on the scattered-light intensity. According to the manufacturer, there is a 5% size resolution at 5- μm particle size.

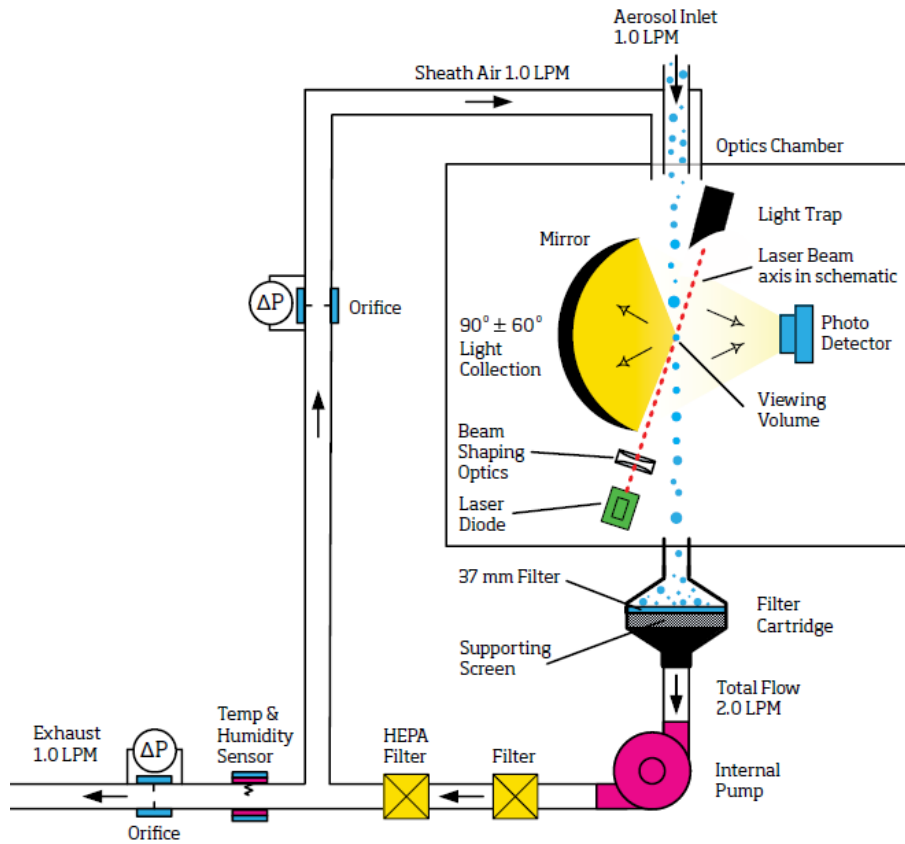


Figure 2.8 Schematic of TSI optical particle sizer (OPS) ("Optical Particle Sizer Model 3330,")

Complex and expensive instruments definitely measure PM concentration in a more precise manner compared to low-cost sensors. These complex and advanced instruments keep the particle flow centered as it passes through the focused laser beam. The sheath flow can stabilize the particle stream and make the particle traverse through the focused beam; however, in the meantime, it can contribute to the dilution of the actual particle concentration. In low-cost sensors, there is no particle-flow control mechanism to stabilize the particle stream.

The uncertainty in PM number or mass concentration measurement could be larger in low-cost sensors since they disregard the effect of the refractive index in their light-scattering systems; however, most of the expensive instruments ask for the refractive index as an input. If no information is available about the refractive index, they just determine the particle-size distribution based on the refractive index of water as a default value, which may lead to some uncertainty on the measurement as well.

To ensure the accurate performance of PM devices, not only low-cost sensors, but also expensive instruments require periodic calibrations. Volckens and Peters (2005) calibrated the expensive TSI aerodynamic particle sizer (Model 3321) independently by collecting fluorescent, polystyrene latex (PSL) spherical particles ranging from 1 μm to 4 μm in diameter on a filter in parallel with APS measurements. Error bars in the calibration plots indicated an uncertainty of 3% to 8% in the number concentration measurements. Most of these calibrations are performed based on NIST and /or ISO standards.

To minimize the uncertainty to some extent, and increase particle-sizing accuracy, Hirleman Edwin D (1980) proposed a system that utilized the ratios of the scattered-light intensities at two or more scattering angles. In this system, a laser light source was used to illuminate the particles. The laser beam was focused by a lens on the sensitive volume. A light stop was used to prevent direct light from propagating through the sensitive volume. Another lens collimated the scattered light to pass it through an annular iris system. The scattered light was then collected by an array of photodetectors at different scattering angles through the annular iris system. A data-acquisition system was used to get the readings of the scattered intensity out of the photodetectors to compute their ratios and compare them to the reference values. The ratio of scattered light for at least one other pair of angles was simultaneously analyzed for each particle

passing through the sensitive volume- or particle-sampling zone. This second ratio then provided a consistency check on each particle analyzed. If the ratio measured at the second pair of angles corresponded to that predicted for the particle size within the valid range of the counter designed, as indicated by the ratio measured at the primary pair of angles, then the particle would be counted. Otherwise, the particle would be ignored as being of a size outside the range of the counter where particles could be accurately sized.

This system might be useful in particle sizing since it eliminates the effect of the Gaussian intensity distribution, but in order to accurately size the particles of each type, the intensity-ratio-calibration curves for each type of particle should be available, corresponding to their particular refractive indices. Since this system uses many photodetectors, it will be costly, may require a larger space, and the rate of power consumption will be higher as well.

Beam shaping has also been used to minimize particle-sizing uncertainty. Leander Molter (1998) used a T-shaped diaphragm aperture with the T-leg oriented in the particle-flow direction. The scattered-light pulse of particles flying through close to the edge of the wider diaphragm area (i.e., T-crossbar) had a shorter time period than particles flying centrally through the diaphragm. Therefore, the first-mentioned particles were excluded during the measurement.

The drawback with the T-shaped diaphragm aperture is that it excludes most of the particles from the measurement, which makes the algorithm complicated as well. However, in our diamond-shaped beam aperture, not only the size but also the complex refractive index of any particle can be measured regardless of its type and material, or the beam position the particle is passing through. There will be no particle exclusions at all.

2.3 Discussion

We studied various PM sizing and index of refraction determination methods ranging from low-cost sensors to expensive instruments. Most of the devices commonly used for air quality monitoring, only measure the size and concentration of PM; however, in the recent years, estimation of the optical properties (complex refractive indices) and particle-size distribution has attracted considerable attention. A method was developed to determine the complex index of refraction of aerosols based on the measurement data of Lidar, but the particle-size distribution was assumed to be known. Twin-angle and multi-angle OPCs were developed that measured the particle size and refractive index, but the methods could give only an average complex index of refraction for a sample containing many particles.

The drawbacks with the above methods can be summarized as (1) particle-size distribution has to be measured by an extra device before the index of refraction can be determined, (2) with twin-angle and multi-angle OPCs, there is not enough evidence of how they picked the scattering angles, and (3) Their methods cannot determine the complex index of refraction of a single particle, so they determine only an average complex refractive index for an aerosol sample.

In our device, we can measure the size and complex index of refraction of single particles simultaneously. We found the three scattering-angles $37\pm 5^\circ$, $80\pm 5^\circ$ and $115\pm 5^\circ$ based on the functionality of differential-scattering cross-section of particles on real and imaginary components of refractive index. This allowed us to create mathematical models to be very efficient and accurate.

Chapter 3 - Application of Low-Cost Particle Sensors for Air-Quality Monitoring in Buildings

In this section, we have calibrated low-cost optical dust sensors GP2Y1010AU0F using an aerodynamic particle sizer (APS) as a reference instrument. A container was built in a 3D printer for each sensor to make it air tight, protect it from ambient light effects, and to connect it to the APS. Four sensors were connected in series with the APS, and data were collected simultaneously on the downstream of a flow loop where the aerosol concentration was controlled. Sensors' performances were compared to each other as well as to the manufacturer's calibration data. Sensors were also exposed at two different positions in a controlled chamber to collect (1) indoor air data and (2) indoor air data with incense burning; these results were compared to the calibration data. Initially, it was found that sensors' data were different from each other by 15%. This percentage was decreased to 5.9% by adjusting the potentiometer on each sensor. Since the sensors work with light-scattering, it was found that their outputs were affected by the ambient light levels causing uncertainties in the measured values. Sensors' data for indoor air (IA) with incense burning were affected by airflow. When connected in series to the APS with 5 L/min airflow passing through them, their data agreed with the calibration data; however, they did not agree when exposed to the still air i.e., without airflow.

Dimensions of a Sharp GP2Y1010AU0F dust sensor are 46 x 30 x 18 mm. It has an operation voltage of 5 ± 0.5 V with a current consumption of (< 20 mA) ("GP2Y1001AU,"). The output signal of this sensor is voltage. An infrared-emitting diode (IRED) and a phototransistor, along with their focusing lenses, are diagonally arranged into this device. When the particles pass through the sensor, they scatter light and the intensity of scattered light detected by the phototransistor is directly correlated to the concentration of the particles.

3.1 Experimental Setup

An experimental setup was developed to calibrate the low-cost sensors using an APS as a reference instrument as shown in the following figure.

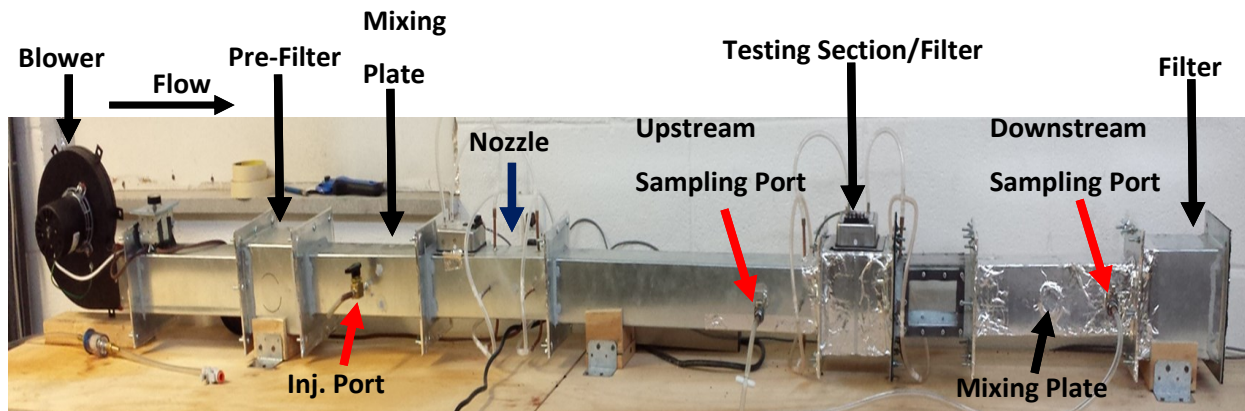


Figure 3.1 Experimental setup

This experimental setup contains the following components:

- A blower that circulates air inside the flow loop
- A high-efficiency particulate air filter (HEPA) pre-filter that prevents particulates in the air stream from penetrating into the flow loop
- An injection port that can be connected to an aerosol generator to inject aerosol particles
- A mixing plate that mixes the aerosol stream to get a uniform concentration
- A nozzle to measure the pressure drop
- An upstream sampling port to measure the aerosol concentration before it penetrates the filter
- Testing section/HEPA filter containing a differential pressure transducer to measure the pressure drop across the filter
- A mixing plate to make the aerosol concentration uniform on the downstream side

- A downstream sampling port used to measure aerosol concentration on the downstream side
- Another HEPA filter at the end of the loop to prevent the particles from entering the chamber

3.2 Calibration Methods

The Sharp dust sensor GP2Y1010AU0F could not be directly connected to the APS for calibration. Therefore, a sensor container with dimensions of 60 x 30 x 25 mm, as shown in Figure 3.2, was built in a 3D printer for each sensor to make it air tight, protect it from ambient light effects, and to make it connect in series with the APS.

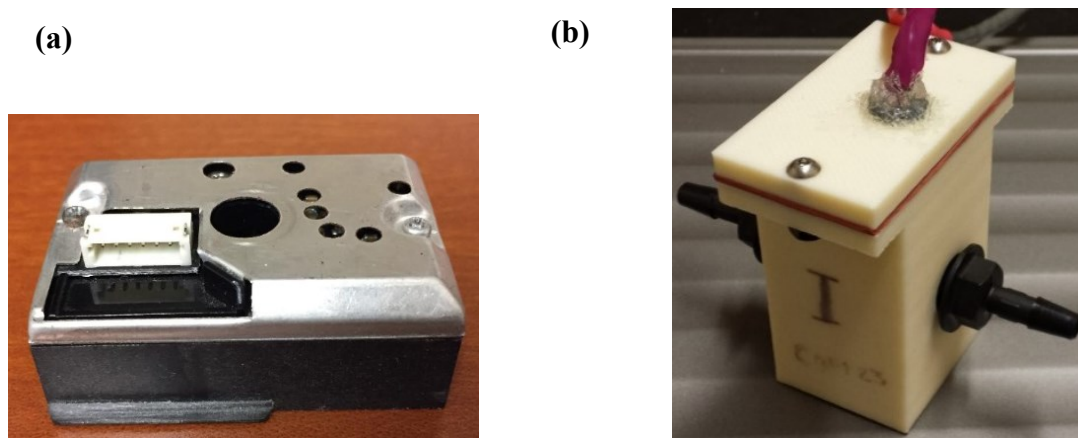


Figure 3.2 (a) Sharp dust sensor, (b) Sensor container

Poly alpha olefin (PAO-4) oil was used in the aerosol generator to inject aerosol particles inside the loop. Four sensors were connected in series with APS on the downstream of the flow loop as shown in Figure 3.3. Sensors were challenged at different aerosol concentrations by poking holes into the HEPA filter at the testing section. Data were collected simultaneously by the sensors

and APS. Sensors provided an output voltage for each concentration that the APS measured. Then the output voltages of the sensors were plotted vs. APS concentration to develop calibration curves.

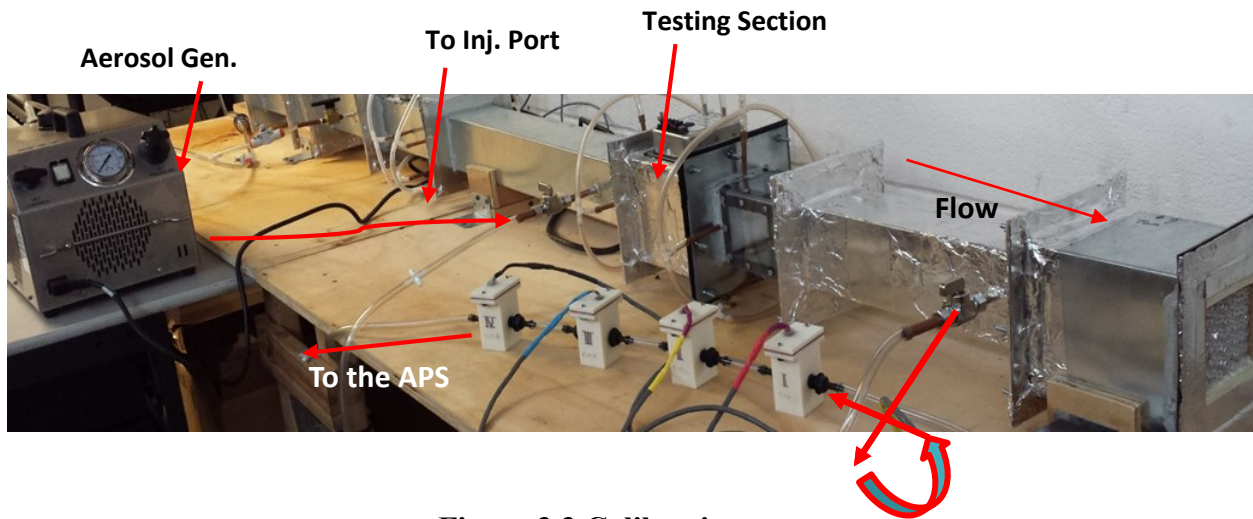


Figure 3.3 Calibration setup

3.3 Calibration Results

Figure 3.4 shows the data obtained for four Sharp dust sensors using the above calibration setup. Initially the sensors' performances were different from each other. The average signal of the sensor with the lowest output was different by 15% and 21% from that of the sensor with the highest output and the manufacturer's data, respectively.

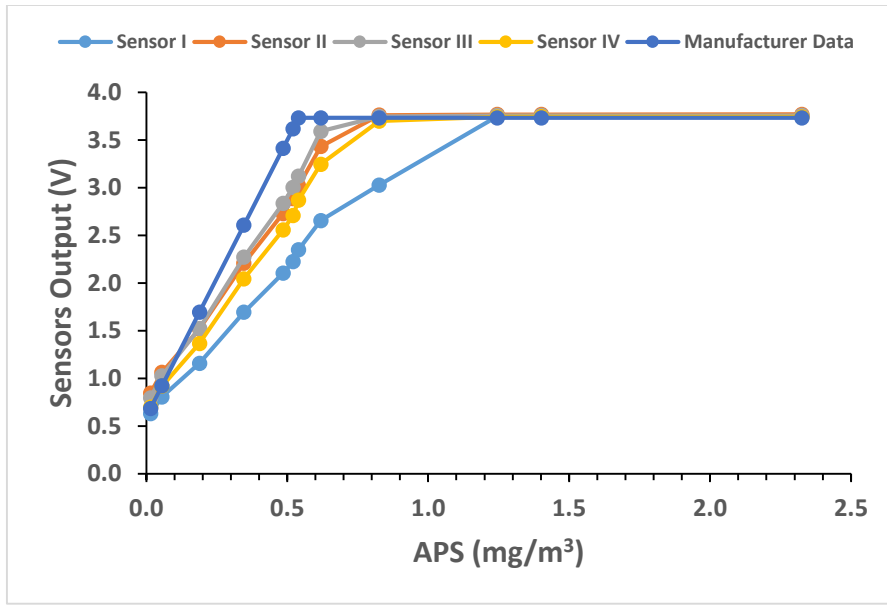


Figure 3.4 Initial calibration data

To decrease the above percent differences, the sensors' initial outputs for indoor air were adjusted to 0.6 V using the potentiometer on each sensor as recommended by the manufacturer. This means each sensor gave an output of 0.6 V due to background noise, regardless of any particles being present inside. Figure 3.5 shows the new data set obtained after adjusting initial outputs of the sensors.

By adjusting the background signal of each sensor to 0.6 V, the percent difference between the signal of the sensor with the lowest output and that of the sensor with the highest output was decreased from 15% to 5.9%. Similarly, it was decreased from 21% to 15% between the lowest sensor output and the manufacturer's data.

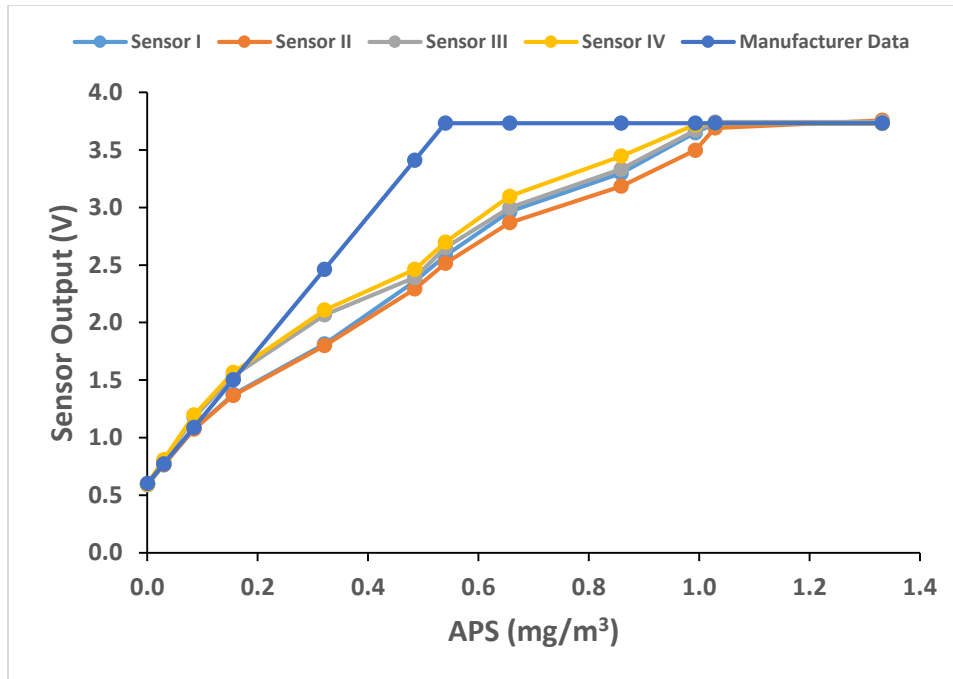


Figure 3.5 Calibration data after adjusting the initial output to 0.6 V

3.4 Sensors' Data for Indoor Air

Sensors were exposed at two different positions (position A, close to the center) and (position B, close to wall) in a controlled chamber as shown in Figure 3.6. Data were collected at positions A and B for two different cases, (1) sensors with containers removed (i.e., no connection with the APS and no airflow passing through them), and (2) sensors connected in series with the APS.

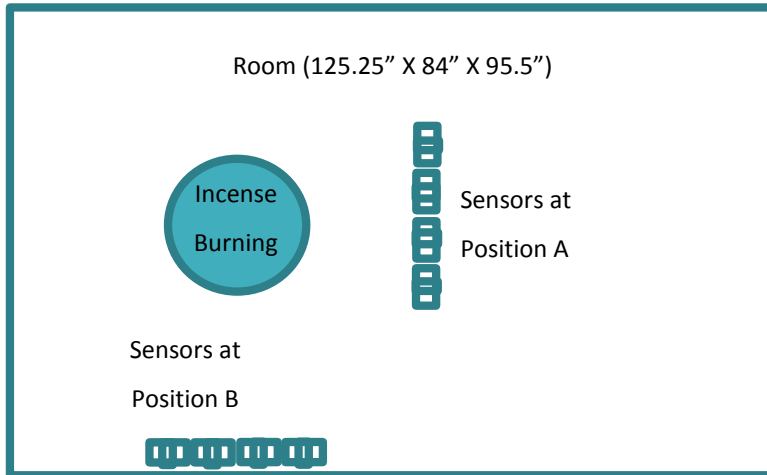


Figure 3.6 Controlled chamber

The initial set of data were obtained without incense burning to determine a baseline for the indoor air concentration. The concentration read by the APS was 0.00114 mg/m^3 and sensors' outputs were around 0.6 V as shown in Figure 3.7.

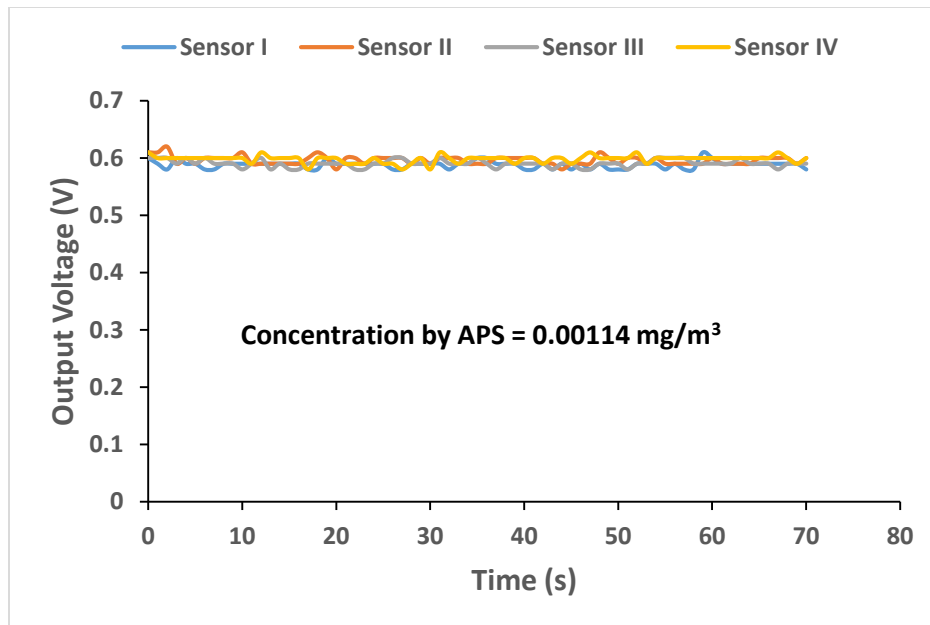


Figure 3.7 Baseline for indoor air concentration

Figure 3.8 (a) shows the sensors' data for position A when the sensors were connected in series with the APS. A 5-L/min airflow was passing through them when they were connected with the APS. We collected the data when incense was burning inside the chamber. The average output voltage of the four sensors was 0.93 V for a concentration of 0.081 mg/m³ measured by the APS. Then the average output voltage and the concentration were compared to the calibration data as shown in Figure 3.8 (b). We can see that measured data agreed well with the calibration data.

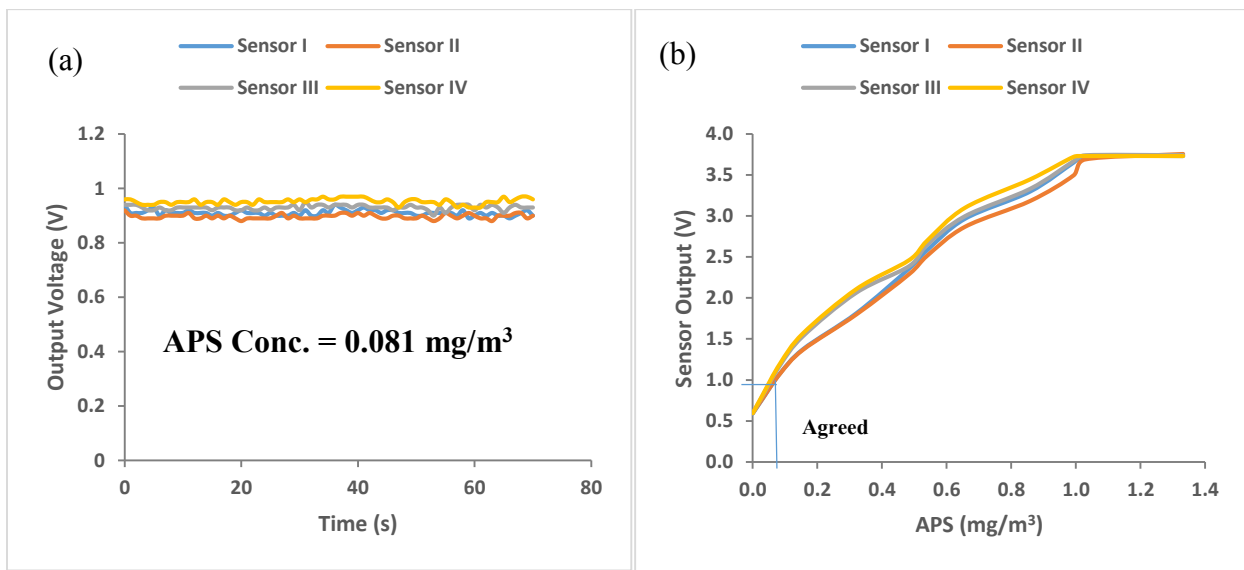


Figure 3.8 (a) Sensors' data for position A (5 L/min airflow), (b) Calibration data

Same experiments were repeated in Figure 3.9 (a) but no airflow was passing through the sensors as they were not connected in series with the APS when data were collected. The measured data did not agree with the calibration data as shown in Figure 3.9 (b).

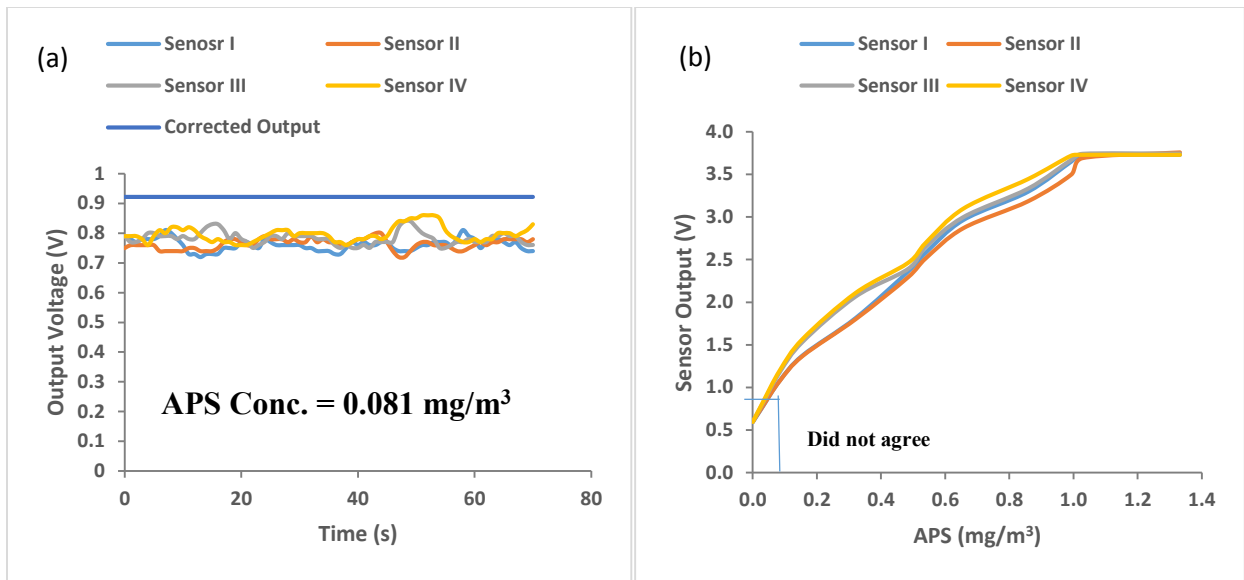


Figure 3.9 (a) Sensors' data for position A (no airflow), (b) Calibration data

In Figure 3.10 we conducted the same experiments as we did in Figure 3.8 but for position B. We can see in Figure 3.10 (b) that the measured data agreed well with the calibration data.

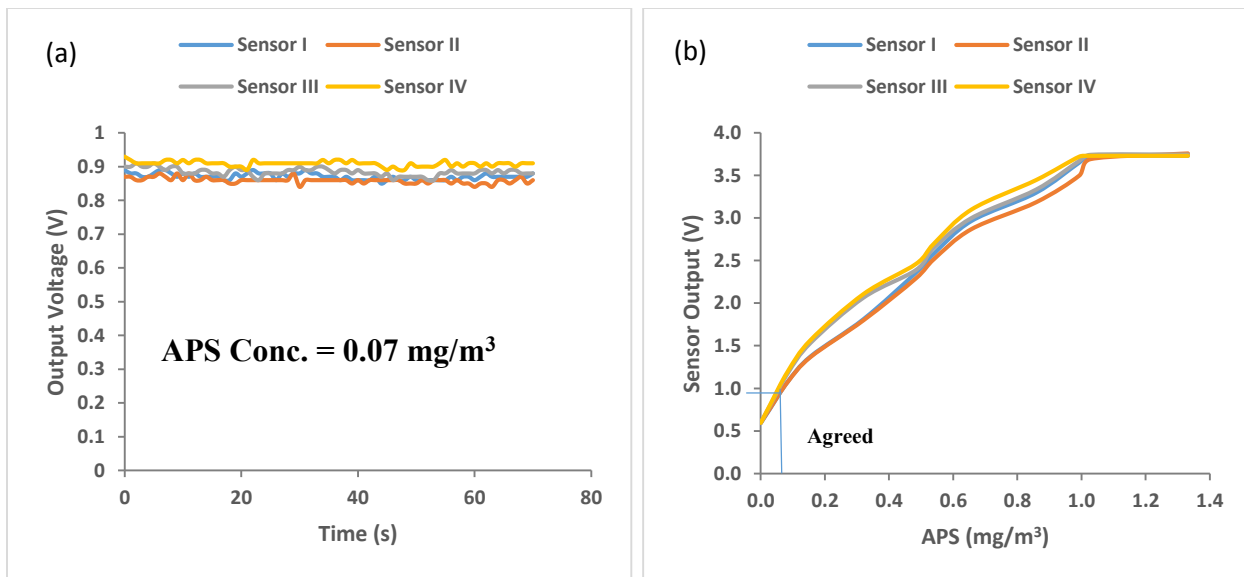


Figure 3.10 (a) Sensors' data for position B (5 L/min airflow), (b) Calibration data

In Figure 3.11, we repeated the same experiments as we did in Figure 3.10 but no airflow was passing through the sensors when data were collected. The measured data did not agree with the calibration data as we can see in Figure 3.11 (b)

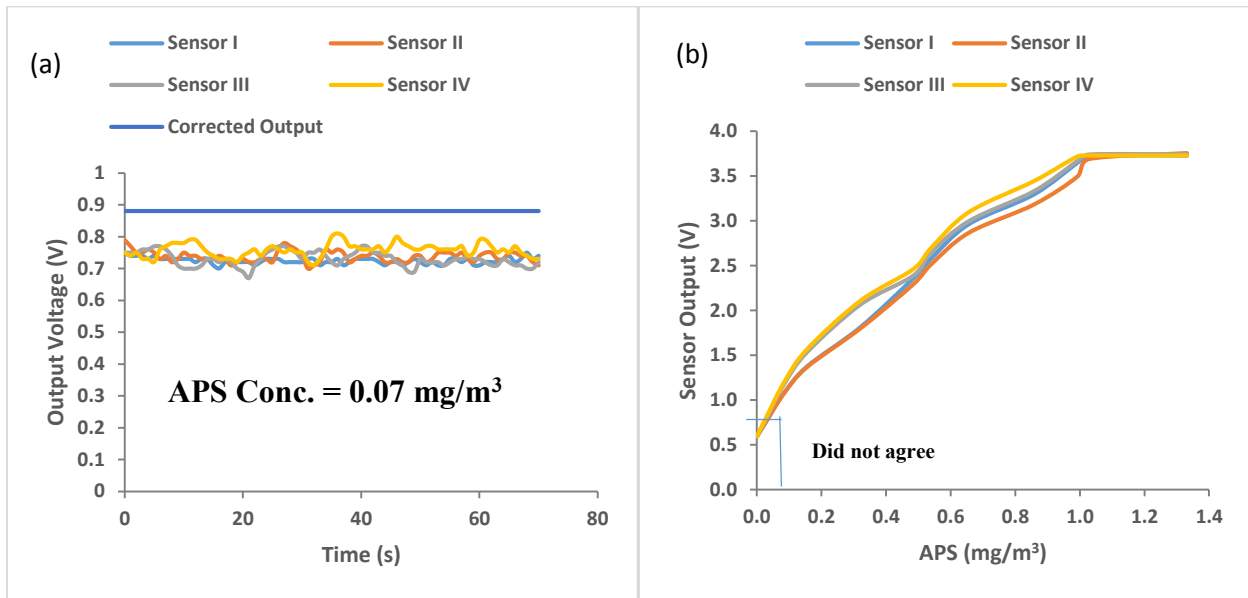


Figure 3.11 (a) Sensors' data for position B (no airflow), (b) Calibration data

3.5 Discussion

Figures 3.8 (a) and 3.10 (a) show the sensors' data agreed with the calibration data when 5 L/min of airflow was passing through them; however, Figures 3.9 (a) and 3.11 (a) show the sensors' data did not agree with the calibration data when no airflow was passing through them.

The percent difference between the sensors' outputs was decreased from 15% to 5.9%. Sensors' data were different from the manufacturer's data by 21.1%; however, it was decreased to 15% after adjusting the potentiometer to 0.6 V.

Sensors' data were affected by airflow as shown in Figures 3.8 - 3.11. The data obtained by the sensors agreed well with the calibration data when they were exposed to airflow; however,

they underestimated the indoor air concentration when no airflow was passing through them and the signals were fluctuating as well.

3.6 Conclusions

To use these sensors for monitoring of the actual indoor air PM concentration, each sensor should be calibrated with a reliable PM instrument. During the calibration, these sensors will be exposed to the same amount of airflow as will be passing through the reference instrument and the calibration curves will be developed accordingly. Therefore, in order to measure the indoor air concentration accurately, these sensors should be adjusted to an air-circulation mechanism, preferably equal to the same amount of airflow that was passing through them during the calibration.

Chapter 4 - A Refractive-Index and Position-Independent Single-Particle Detector for Large, Non-Absorbing Spherical Particles

In this chapter we show that for spherical particles with real refractive index and diameters greater than ca. 10 microns, the differential scattering cross-section is only independent of the refractive index at angles near $37 \pm 5^\circ$. We built a device with a modified Gaussian incident beam profile so that the beam transit time of a particle passing through the beam can determine the true incident intensity for the scattering of the particle. By combining the modified Gaussian incident beam profile with detection of scattered light near $37 \pm 5^\circ$, we demonstrated a refractive-index independent measurement of single-spherical particles as they pass through the beam.

We limit this work to spheres. Calculations for non-spherical particles are more labor intensive and will be pursued in the future. Nevertheless, it is worthwhile to note that non-spherical-particle light-scattering has many properties semi-quantitatively similar to those of spheres including a strong forward-scattering diffraction regime, a hump regime as uncovered by Q-space analysis (Sorensen, 2013), and enhanced backscattering. See for example (Heinson et al., 2016).

4.1 Correction for the Gaussian Beam

The intensity of a Gaussian laser beam decreases with radius as $\exp(-r^2)$, with the peak intensity being at the center as $r = 0$. Figure 4.1 shows this intensity-distribution percentage.

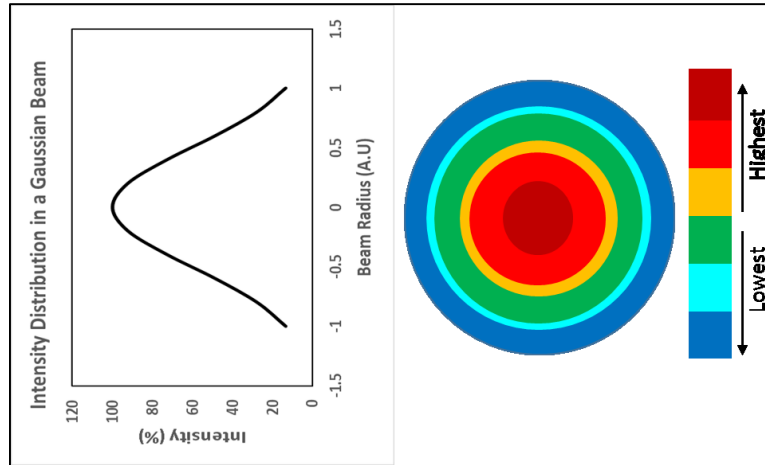


Figure 4.1 Intensity-distribution percentage in a Gaussian laser beam

The nature of a radial Gaussian laser beam profile can make the light-scatter of a large particle passing through the edge of the beam, and a small particle passing through the center of the beam, indistinguishable. This non-uniform profile significantly contributes to the uncertainty or cost of sizing particles based on light-scattering.

One might think that for a particle passing through a cylindrical beam, time of flight would indicate whether or not the particle passed through the center of the beam along a diameter, or along a cord of the cylindrical cross-section. However, for a true Gaussian beam, all particle paths have the same time of flight; in fact, the Gaussian profile is unique in this respect. Here we modify the Gaussian shape with a diamond-shaped aperture so that time of flight can indicate the precise position of the particle, and hence the precise incident intensity. The diamond profile is shown in Figure 4.2.

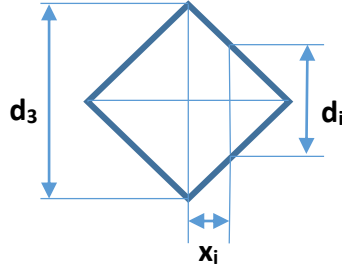


Figure 4.2 Diamond-shaped beam aperture, replotted (Waez et al., 2018)

In Figure 4.2, assuming particles move vertically through any position x_i for a given average velocity, time of flight varies linearly from the center towards the edge. Using time of flight and the known velocity, the cord length d_i can be found and then x_i calculated. Light-scattering intensity is maximum on the x axis at any position x_i where the particles are dropped.

To accurately predict particle size, not only the intensity distribution in a Gaussian beam, but also many other parameters, can play a role. These parameters can be related to the laser, cut-beam geometry, photodiode, photodiode amplifier, and so on. In this section, all parameters are related to each other in order to present a general equation for predicting particle size. For a Gaussian beam,

$$I(r) = I_0 e^{-(2r^2/w^2)} \quad (4.1)$$

where $I(r)$ is the intensity as a function of the beam radius, I_0 is the peak intensity at the center of the beam, r is the radial distance from the beam center, and w is the beam waist. The radial distance in rectangular coordinates is

$$r = \sqrt{x^2 + y^2} \quad (4.2)$$

Total power in the beam is the integral of Eq. (4.1).

$$P_{Tot} = \int_0^{\infty} \int_0^{2\pi} I(r) r dr d\theta \quad (4.3)$$

Combining Eqs. (4.1) and (4.3) and integrating, one finds the total power in the beam.

$$P_{Tot} = I_0 \int_0^{\infty} \int_0^{2\pi} e^{-(2r^2/w^2)} r dr d\theta = \pi/2 I_0 w^2 \quad (4.4)$$

P_{Tot} is generally a known parameter. Then Eq. (4.4) can be solved for I_0 .

To obtain the scattered power on the photodiode, Eq. (4.1) can be multiplied by the differential scattering cross-section and integrated with a solid angle.

$$P_{scat} = \int_0^{\Delta\Omega} I(r) \frac{dC}{d\Omega} d\Omega \quad (4.5)$$

In Eq. (4.5), $\Delta\Omega$ is the solid angle the photodiode makes with the particle position in the beam.

Assuming $\frac{dC}{d\Omega}$ is constant in the small ($\pm 5^\circ$) collection-angle range,

$$P_{scat} = I_0 e^{-(2r^2/w^2)} \frac{dC}{d\Omega} \Delta\Omega \quad (4.6)$$

The photodiode gives an output voltage V_i , which can be obtained by

$$V_i = P_{scat} * R(\lambda) * K \quad (4.7)$$

In the above equation, $R(\lambda)$ is the photodiode responsivity and K is the conversion factor of the photodiode amplifier.

Since we considered a diamond-shaped beam, we need to take the new beam parameters into account. The parameters in Figure 4.2 can be related as

$$d_i = v * t_i = d_3 - 2x_i \quad (4.8)$$

In Eq. (4.8), v is the average velocity of the particle and t_i is the time of flight of a particle passing through any x_i position in the beam. We will assume the particles are delivered to the scattering volume with the same velocity.

Since peak-scattered intensity is desired for a given velocity and time of flight, and the peak-scattered intensity can be on the x axis for the particles being dropped vertically and passing through any x_i position, we assume the y component of r in Eq. (4.2) to be zero. Thus, only the x component of r can play a role in that equation. Solving Eq. (4.8) for x_i , and substituting it for r into Eq. (4.6), Eq. (4.9) is obtained.

$$I_0 e^{-(2x_i^2/w^2)} dC/d\Omega \Omega_c = I_0 e^{(-(d_3-vt_i)^2/2w^2)} dC/d\Omega \Omega_c \quad (4.9)$$

4.2 Optimum Scattering Angle for Refractive-Index Independency

When a particle passes through an optical beam, it scatters light over a 4π steradian solid angle. The amount of light scattered by the particle is characterized by the scattering cross-section. The scattering cross-section can be a function of many variables including scattering angle, excitation wavelength, particle size, and refractive index. The total scattering cross-section for different spherical particle sizes and two refractive indices is presented in Figure 4.3. This figure was plotted for a 0.532- μm wavelength using the MiePlot online program developed by Laven (2010). The figure shows the total scattering cross-section to be strongly dependent on particle size and weakly dependent on the real refractive index when the particle diameter is $d \geq 1\mu\text{m}$. The total scattering cross-section also depends on the refractive index for particles smaller than the

wavelength, i.e., in the Rayleigh-scattering regime; however, it is independent of the refractive index for particles much greater than the wavelength.

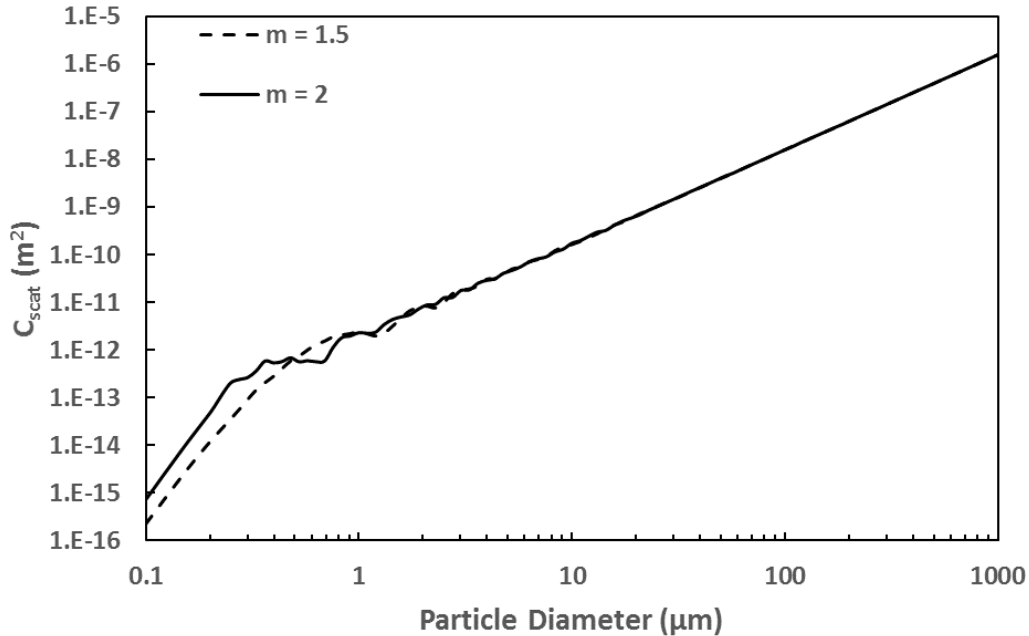


Figure 4.3 Total scattering cross-section for spherical particles scattering light with a wavelength of 0.532 μm , replotted (Waez et al., 2018)

In practical light-scattering systems, only a portion of the scattered light is gathered by a photodiode, which rests at a given angle. Such measurements are related to the differential-scattering cross-section. The photodiode was used to collect light over a 10° scattering-angle range. It is instructive to check and see if the same dependence on particle size and refractive index holds for the smaller scattering angles.

Figures 4.4 – 4.10 show the differential-scattering cross-section averaged over the 10° range when the detector is centered at the angle indicated. These figures are plotted based on unpolarized light. The situation is shown to be much more complex as a strong functional relationship with the refractive index is now seen. For particle-sizing applications, the refractive

index is not known ahead of time, so this dependence is problematic. Fortunately, at a scattering angle of $37\pm 5^\circ$, the differential cross-section still shows relative independence of the refractive index. On the other hand, the differential-scattering cross-section shows a strong dependence on the real refractive indices for scattering angles other than 37° . Therefore, a good strategy to build an optical particle-sizing instrument is to use a 37° scattering angle so that the refractive index, hence particle composition, need not be known.

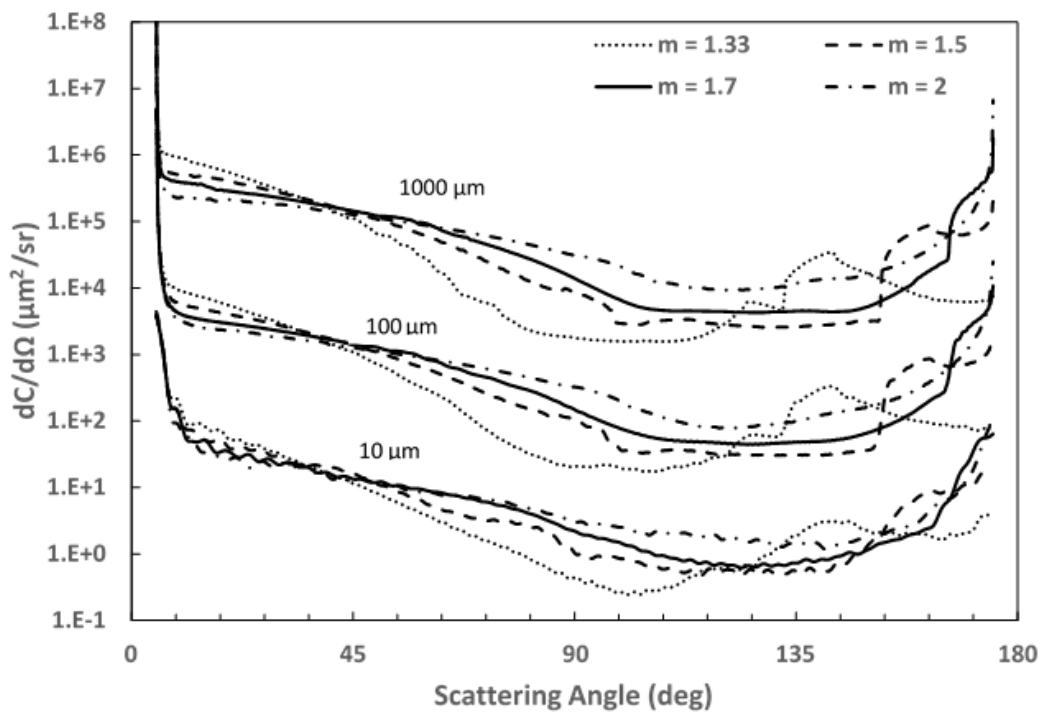


Figure 4.4 Average differential-scattering cross-section over a 10° scattering angle for four different refractive indices and three different particle diameters (10,100 and 1000 μm), replotted (Waez et al., 2018)

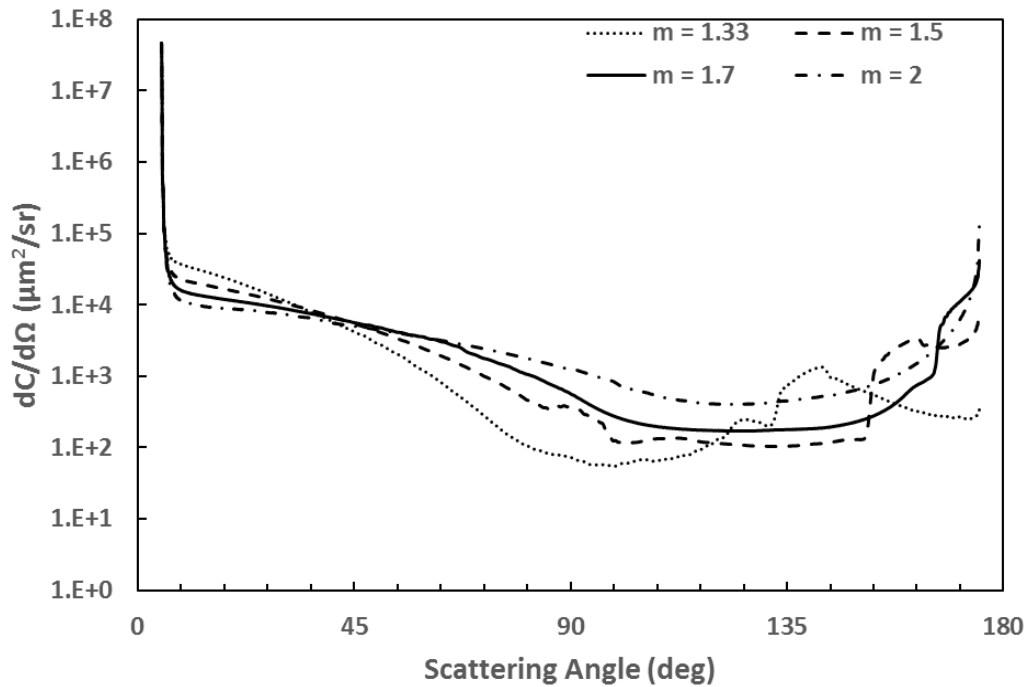


Figure 4.5 Average differential-scattering cross-section over a 10° scattering angle for four different refractive indices (200- μm particle diameter)

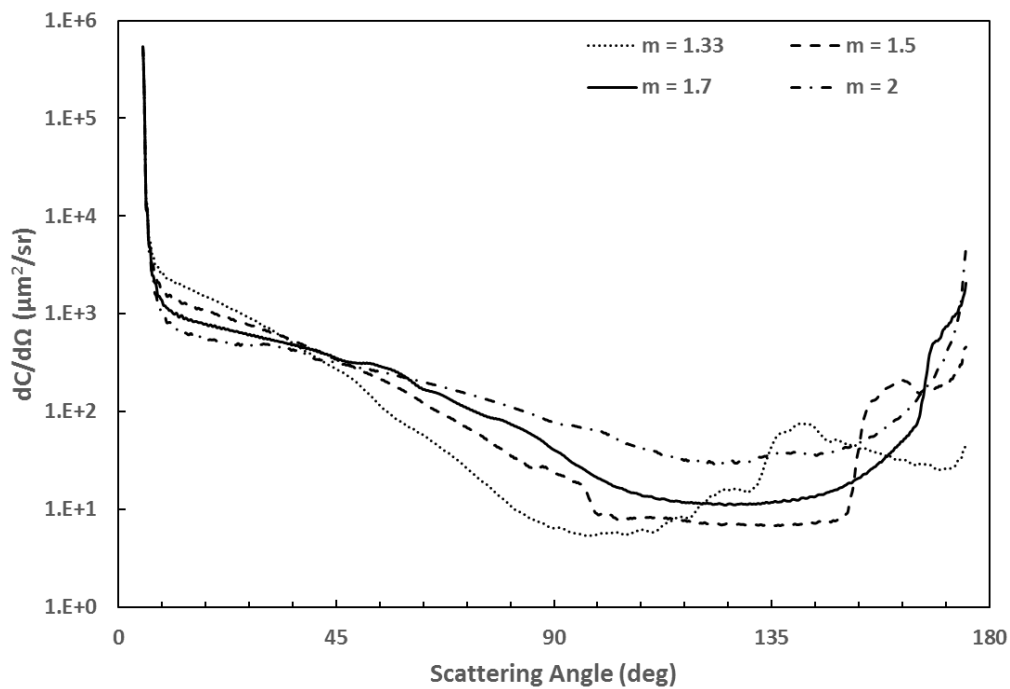


Figure 4.6 Average differential-scattering cross-section over a 10° scattering angle for four different refractive indices (50- μm particle diameter)

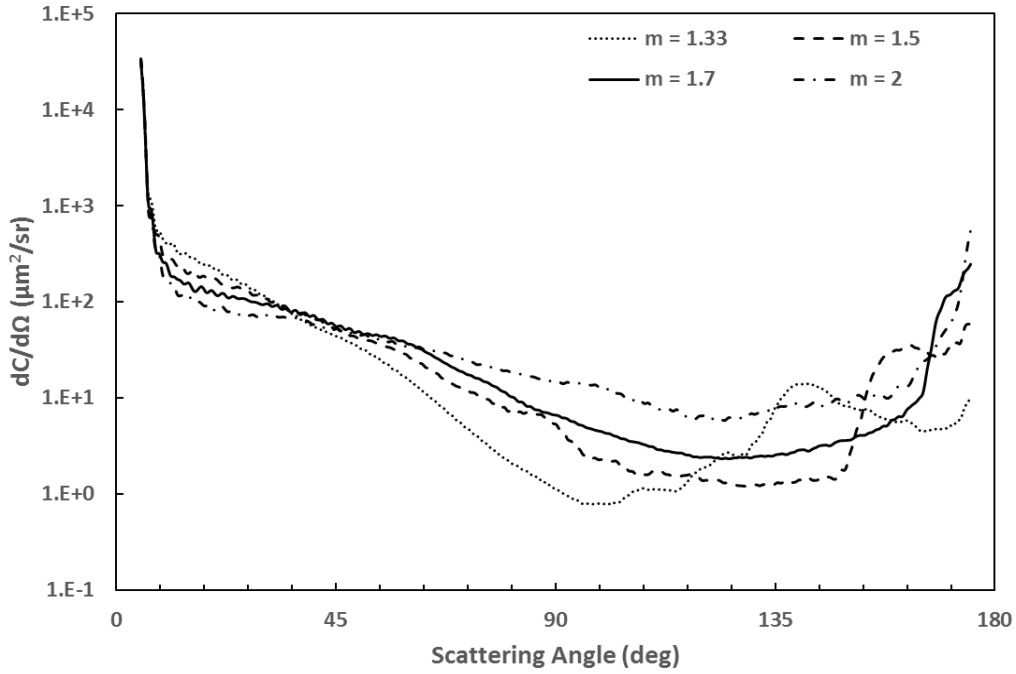


Figure 4.7 Average differential-scattering cross-section over a 10° scattering angle for four different refractive indices (20- μm particle diameter)

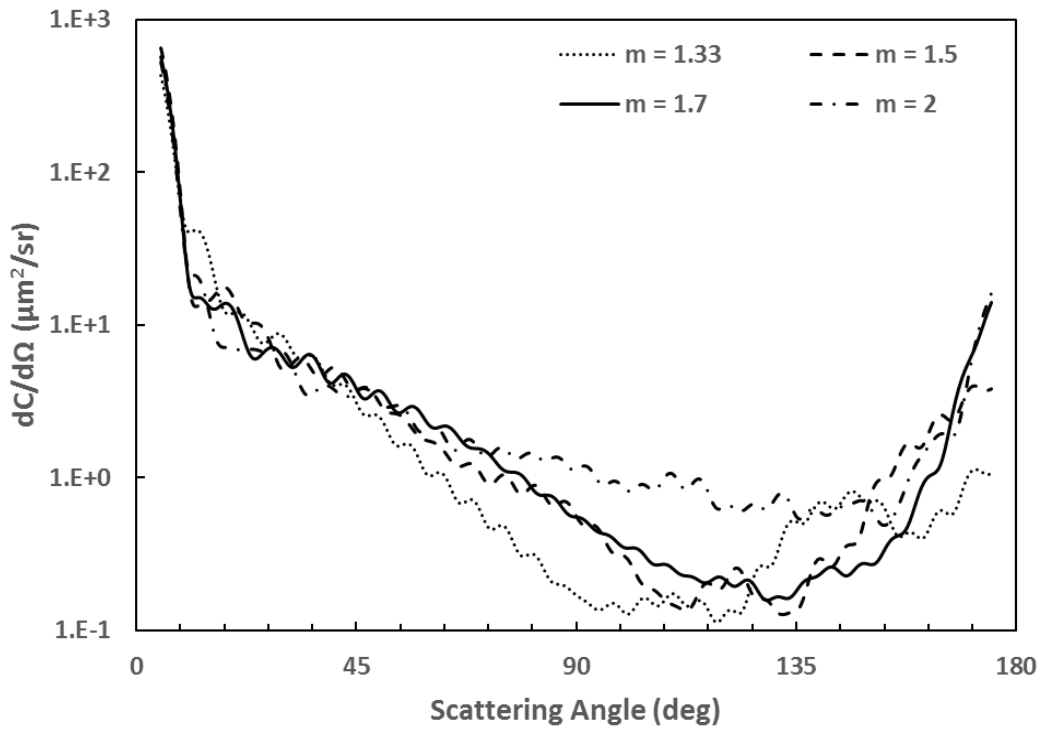


Figure 4.8 Average differential-scattering cross-section over a 10° scattering angle for four different refractive indices (5- μm particle diameter)

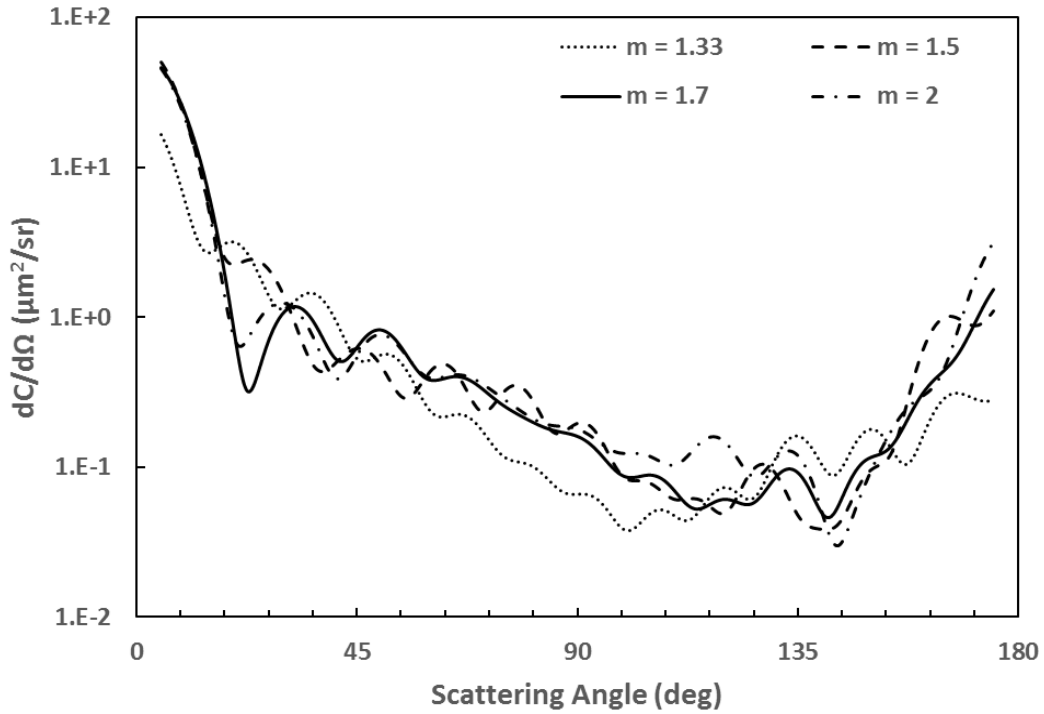


Figure 4.9 Average differential-scattering cross-section over a 10° scattering angle for four different refractive indices ($2\text{-}\mu\text{m}$ particle diameter)

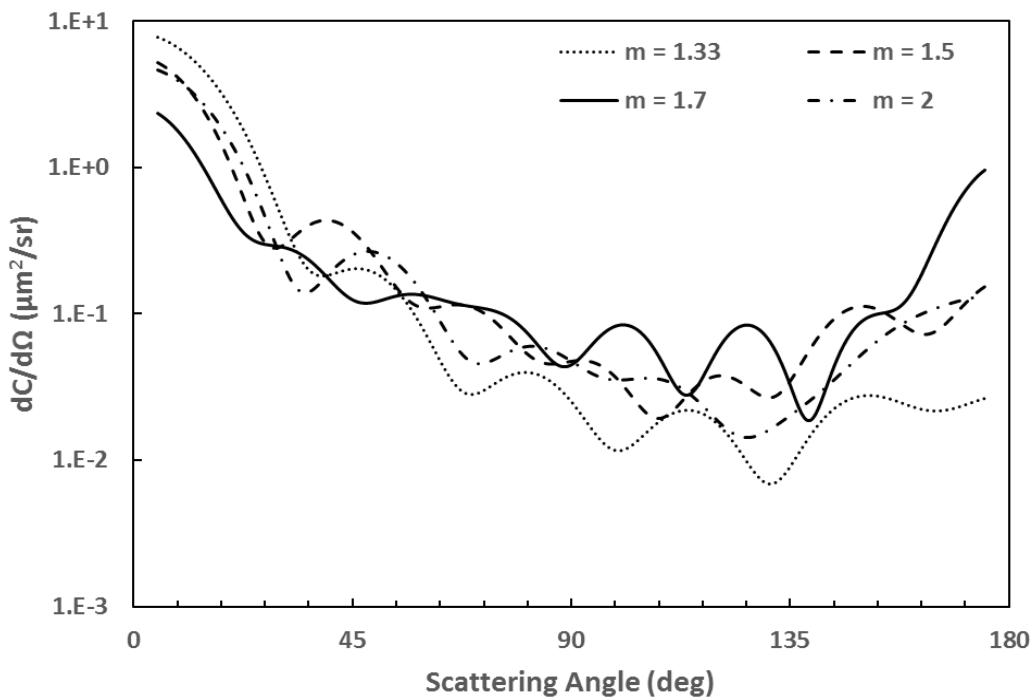


Figure 4.10 Average differential-scattering cross-section over a 10° scattering angle for four different refractive indices ($1\text{-}\mu\text{m}$ particle diameter)

Actual differential scattering cross-sections for each particle diameter and four different refractive indices were obtained using an online program, Laven (2006). Using actual values of $dC/d\Omega$, an equation was found by regression analysis for the differential-scattering cross-section vs. particle diameter for particle sizes of 1 μm and above (Waez et al., 2018).

$$dC/d\Omega = 0.18d^2 \quad (4.10)$$

Combining Eqs. (4.4), (4.7), (4.9), and (4.10), Eq. (4.11) was found (Waez et al., 2018).

$$d(t_i, v, V_i, \Omega) = \left\{ \frac{2.78 * 10^6 \pi w^2 V_i}{P_{tot} R(\lambda) K} \text{Exp} \left[\frac{(d_3 - vt_i)^2}{2w^2} \right] \frac{\Omega_i}{\Omega_c^2} \right\}^{0.5} \quad (4.11)$$

Eq. (4.11) is used to determine the diameter d of the particle. In this equation, Ω_c and Ω_i are the solid angles the photodiode makes with the center “c” of the beam and any x_i position in the beam, respectively. The term 10^6 is a conversion factor that gives the particle diameter in μm .

Here it is important to acknowledge the refractive index can be complex and hence written as $m = n + i\kappa$. In our analysis above, we have taken the imaginary part to be zero, i.e. $\kappa = 0$. We expand this study to consider complex refractive indices in Chapter 5.

4.3 Uncertainty Analysis

We now present an uncertainty analysis by applying the propagation of error to Eq. (4.11). Initially, we compared actual and predicted differential-scattering cross-sections to determine the uncertainty in the coefficient of the fitted equation, i.e., Eq. (4.10), for predicting the differential-scattering cross-section. Figure 4.11 shows the comparison for different particle sizes and four refractive indices. It can be seen that the uncertainty in the coefficient of the fitted equation is

smaller for particle sizes of 10 μm and above; however, it gets larger as the particle size becomes smaller than 10 μm .

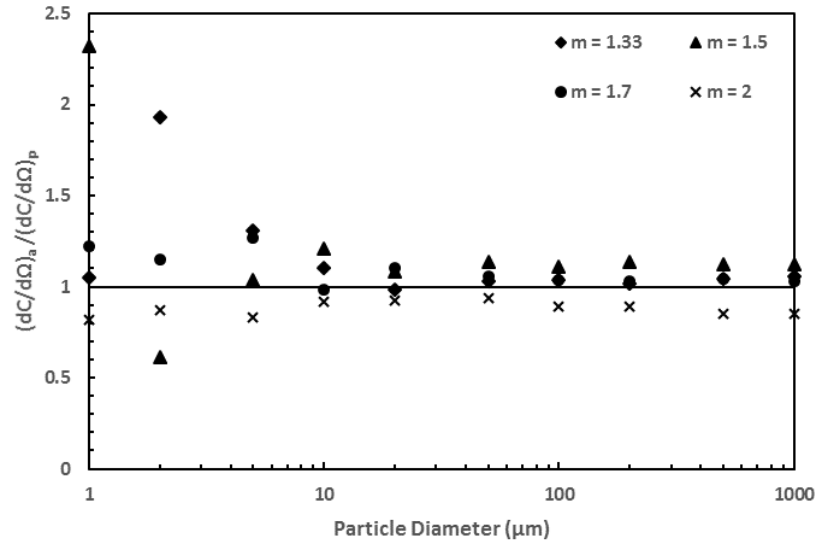


Figure 4.11 Comparison of actual to predicted differential-scattering cross-sections, replotted (Waez et al., 2018)

Applying the propagation of error method to Eq. (4.11), we obtained an equation to define the total uncertainty in the predicted particle size in dimensionless form. We plotted the equation in Figure 4.12 to graphically represent the uncertainty distribution for each particle size. In our analysis, the uncertainty in the coefficient of Eq. (4.10) was dominant.

In Figure 4.12, we can see the uncertainty is less than 10% for particles greater than 10 μm . However, for particles smaller than 10 μm , the uncertainty increases above 10%. Overall, the uncertainty range is 6% – 32%, with $\pm 6\%$ for a 20- μm particle and $\pm 32\%$ for a 2- μm particle.

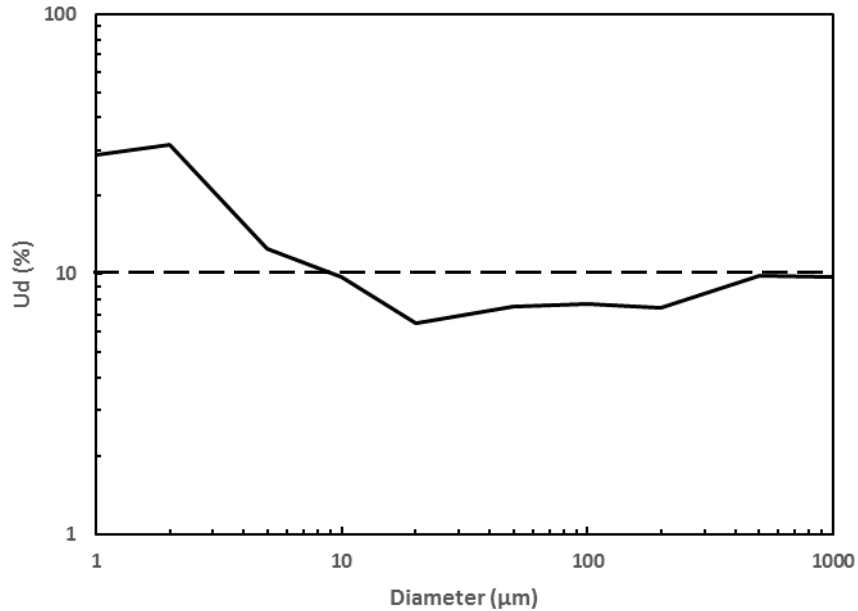


Figure 4.12 Uncertainty in predicted particle size, replotted (Waez et al., 2018)

Finally, note the particles we used below are 0.5 mm in diameter and the diamond-shaped aperture is at most $d_3 = 7.07$ mm wide, but narrows to zero width, see Figure 4.2. Thus at some point for large x_i , the size of the particle dominates the transit time. However, simple geometry implies there is a band of width $2x_i = 5$ mm centered on the aperture where the particle diameter is 10% or less of the transit length d_i , hence the transit time of 71% of all particles will not be significantly affected. In most situations, the particles will be smaller, or if necessary, the aperture can be made bigger to control this possible uncertainty.

4.4 Experimental Setup

The experimental setup uses a Laserglow BDG005XXX, 5-mW, 532-nm wavelength laser as a light source to illuminate the particles; a collimating lens with a focal length of 290 mm to collimate the beam and make it uniform in diameter of 7.5 mm; an aperture to make a diamond-shaped beam profile with dimensions of 5mm x 5mm; and two Thorlabs SM05PD1A photodiodes with a responsivity of $R(532 \text{ nm}) = 0.32 \text{ A/W}$ positioned at $\pm 37^\circ$ scattering angle to detect the

scattered light by particles simultaneously for as long as the particles were in the beam. The photodiodes have an active area of 13 mm^2 and were positioned at a distance of 18 mm from the center of the beam, thus making a solid angle of 0.04 steradian corresponding to the center of the beam. Two Thorlabs PDA200C photodiode amplifiers with a conversion coefficient of $1 \times 10^7 \text{ V/A}$ were used to display the scattered-light signal detected by the photodiodes. A National Instruments (NI) SCXI-1000 data acquisition system was connected to the photodiode amplifiers and LabVIEW program to record the data. Additionally, a ramp was used overhead of the photodiodes to help drop a particle on demand at exact positions of the beam. There was a spacing of 1.25 mm between the grooves in the ramp. Based on our beam dimensions, we could use five particles (one in each groove) to drop at five positions on the beam. More information about the equipment is provided in Figures 4.13 – 4.17.

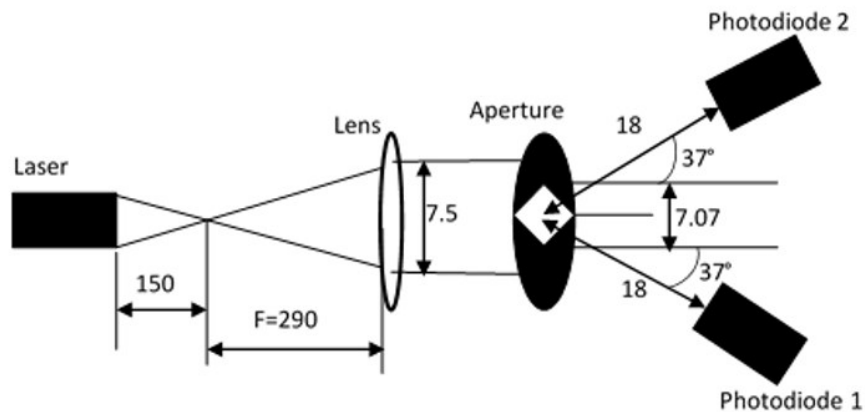


Figure 4.13 Schematic diagram of the experimental setup, dimensions (mm), replotted (Waez et al., 2018)

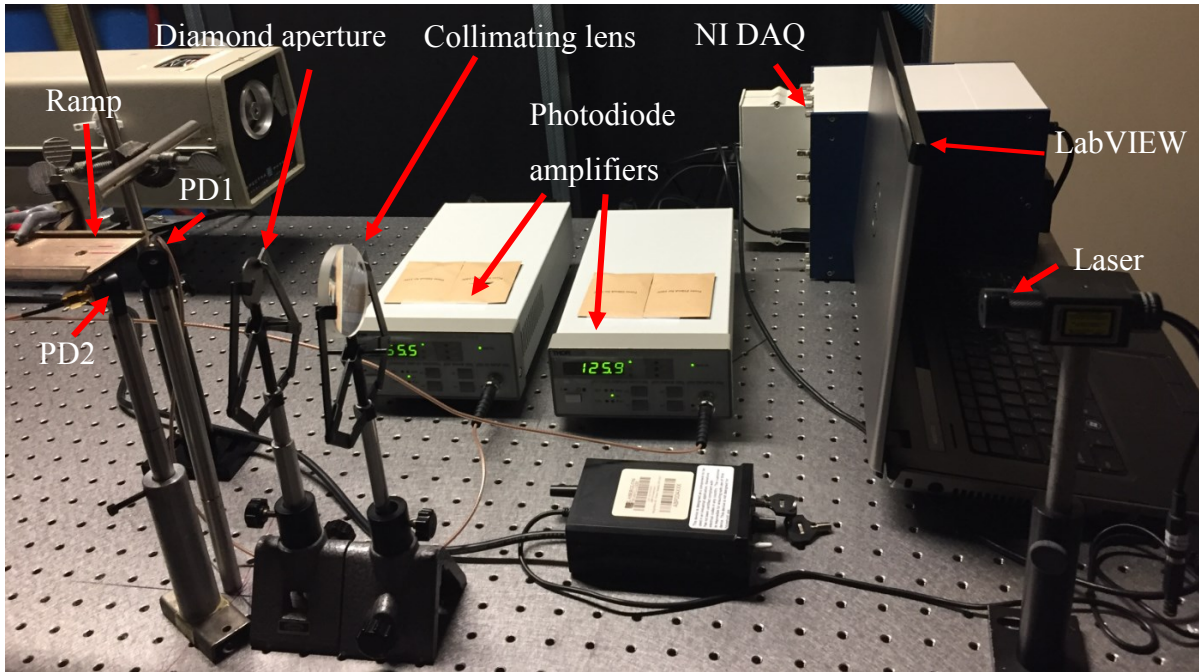


Figure 4.14 Picture of the experimental apparatus

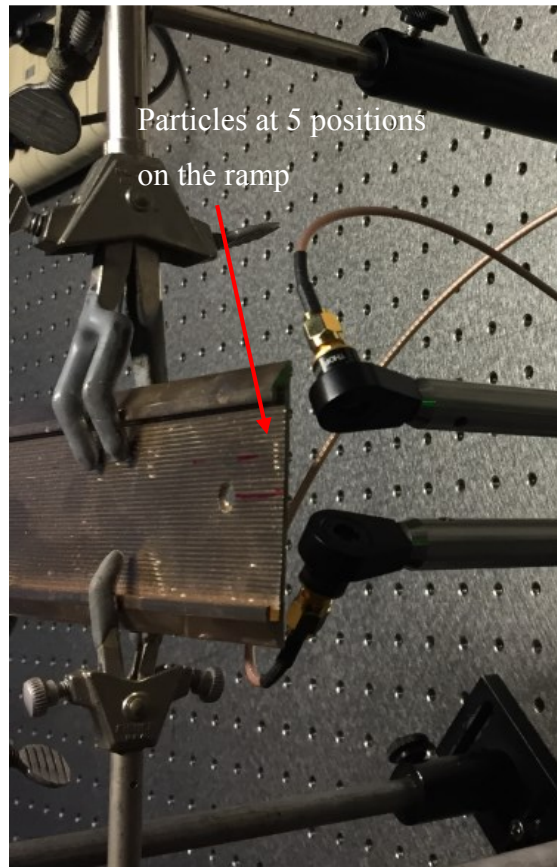


Figure 4.15 Portion of the apparatus to show the particles on the ramp

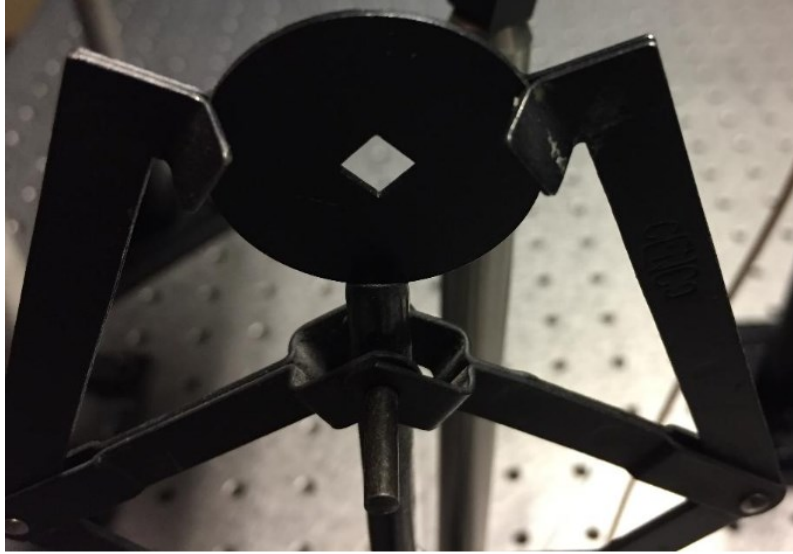


Figure 4.16 Diamond-shaped aperture

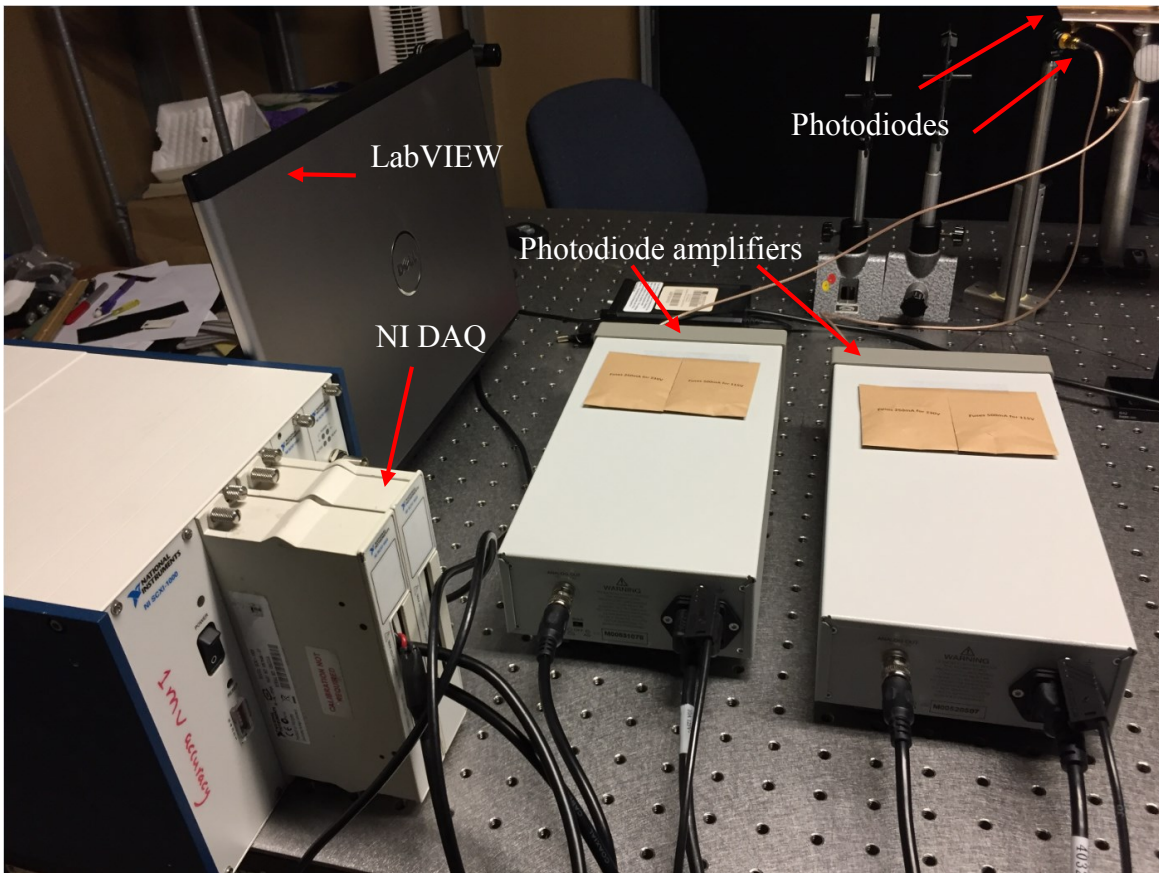


Figure 4.17 Connection of the devices

4.5 Results and Discussion

To validate this research and compare the experimental results to the theory, particles of two different materials, i.e., barium titanate glass-compound (BTGC) and glass beads 500 ± 10 - μm in diameter, were dropped through the center of the beam. The photodiodes positioned at $\pm 37^\circ$ scattering angles, recorded instantaneously the scattered-light intensity and time of flight for each particle as shown in Figure 4.18. Since the particles were dropped at the center of the beam, both photodiodes recorded identical outputs. However, if the particles had been dropped at different positions on the beam, the photodiode closer to the particle's position would obviously record a higher output. In that case, output of the photodiode with the greater peak voltage would be used as the optimum value in Eq. (4.11) to predict the particle size.

Figure 4.18 confirms the independence of the data to the refractive index at a 37° scattering angle since two different types of particles, i.e. BTGC ($m = 1.9$) and glass ($m = 1.5$), provided identical outputs. The consistent repeatability of our data can also be seen in this figure. If we consider any of these particles with its corresponding peak voltage and time of flight, using Eq. (4.11), we can predict the particle size within the $\pm 10\%$ uncertainty as indicated in Figure 4.12 for 500 - μm particles. This can be seen in Table 4.1.

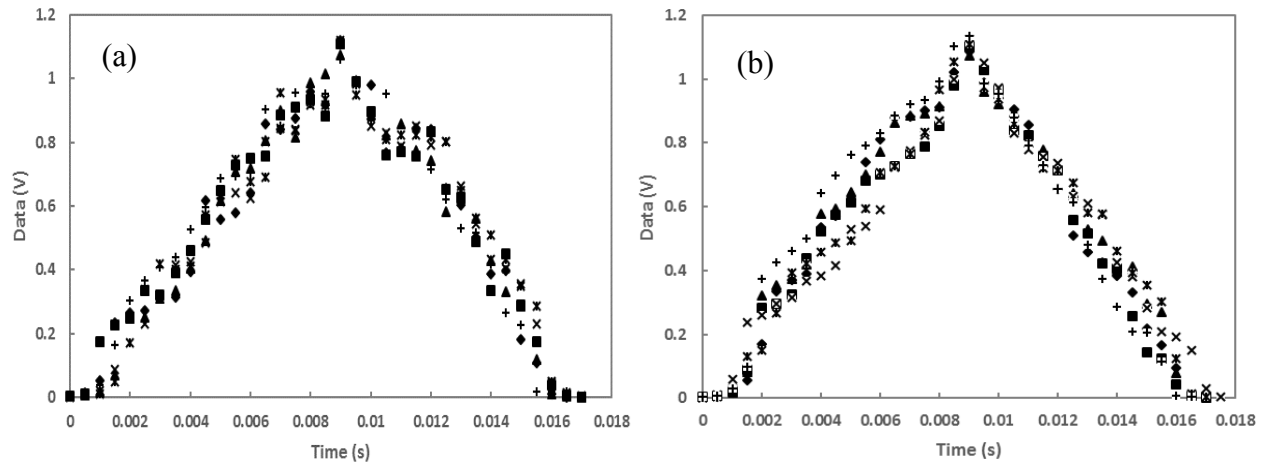


Figure 4.18 Experimental data for 500- μm particles at 37° scattering angle. Each symbol indicates a different particle — (a) BTGC ($m = 1.9$), (b) glass ($m = 1.5$), replotted (Waez et al., 2018)

Table 4.1 Comparison of actual to predicted particle diameters

Particles	Actual Diameter ($\pm 10\mu\text{m}$)		Predicted Diameter (μm)		Uncertainty (%)	
	Glass (μm)	BTGC (μm)	Glass	BTGC	Glass	BTGC
1	500		468	452	6.4	9.5
2	500		463	465	7.4	7
3	500		455	463	9	7.4
4	500		454	465	9	7
5	500		465	455	7	9
6	500		467	463	6.6	7.4

To check for the refractive-index dependency, we repeated the same experiment as we had done in Figure 4.18, but for a 90° scattering angle as shown in Figure 4.19. Unlike Figure 4.18, in Figure 4.19 we can see the peak voltages for BTGC ($m = 1.9$) and glass ($m = 1.5$) are very different from each other. On average, the peak voltage is different by a factor of 3, which obviously confirms that scattered-light intensity depends on a refractive index at a 90° scattering angle. It can also be seen in Figure 4.4 that for a 90° scattering angle, the larger the refractive index, the larger the differential scattering cross-section, which quantitatively agrees with the following experimental data.

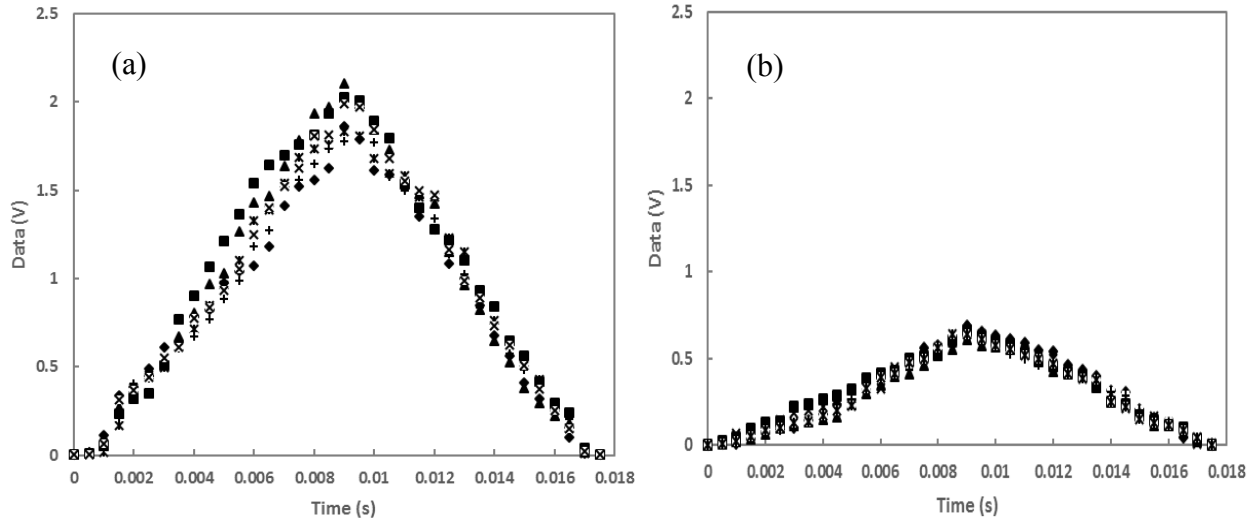


Figure 4.19 Experimental data for 500- μm particles at a 90° scattering angle. Each symbol indicates a different particle — (a) BTGC ($m = 1.9$), (b) glass ($m = 1.5$), replotted (Waez et al., 2018)

Similarly, in Figures 4.20 and 4.21, we can see that five particles of 500 and 600 μm in diameter were dropped at five different positions in the beam and the scattered-light signals were recorded only by one of the photodiodes. The gray lines, which show the maximum signal with the longest time of flight, have passed through the center of the beam; however, the orange and yellow lines show the signals of the particles that have passed a little bit off center of the beam but since their time of flights are identical, we can confirm that both of them have passed at symmetric positions from the center. The signal in the orange is higher compared to the yellow line, which indicates the position of the photodiode was closer to the orange, thus making a larger solid angle. The same argument is true with light blue and dark blue lines, except these particles have passed at positions closer to the edge of the beam since their time of flights are smaller as well. Table 4.2 compares the actual and predicted particle sizes in Figure 4.20. Since the particles with yellow and dark blue lines have passed at positions closer to the second photodiode, output voltages of the mentioned particles recorded by the second photodiode were identical to the orange and light blue

lines, respectively. Then the maximum voltages read by the second photodiode, i.e., 0.9 volts for yellow and 0.53 volts for dark blue, were used in the calculations shown in Table 4.2.

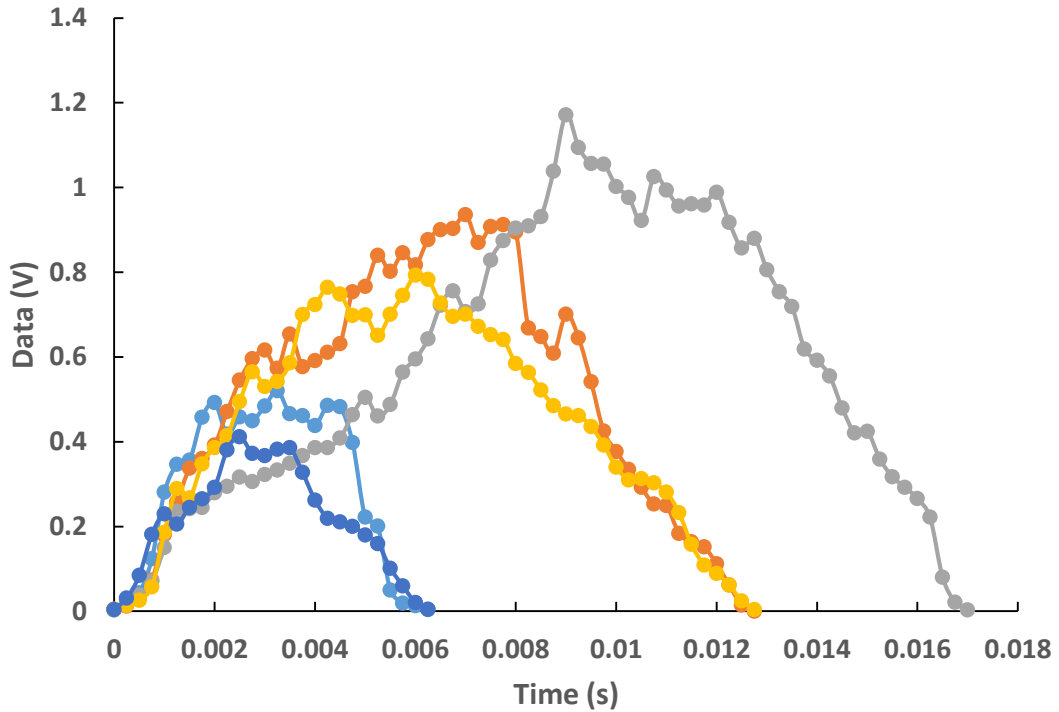


Figure 4.20 Experimental data for 500- μm particles at five different positions in the beam

Table 4.2 Comparison of actual to predicted particle diameters for 500- μm particles passed at five different positions

Particles	Actual Diameter ($\pm 10\mu\text{m}$)	Predicted Diameter (μm)	Uncertainty (-%)
Gray	500	475	5
Orange	500	465	7
Yellow	500	456	8.8
Light Blue	500	469	6.2
Dark Blue	500	474	5.2

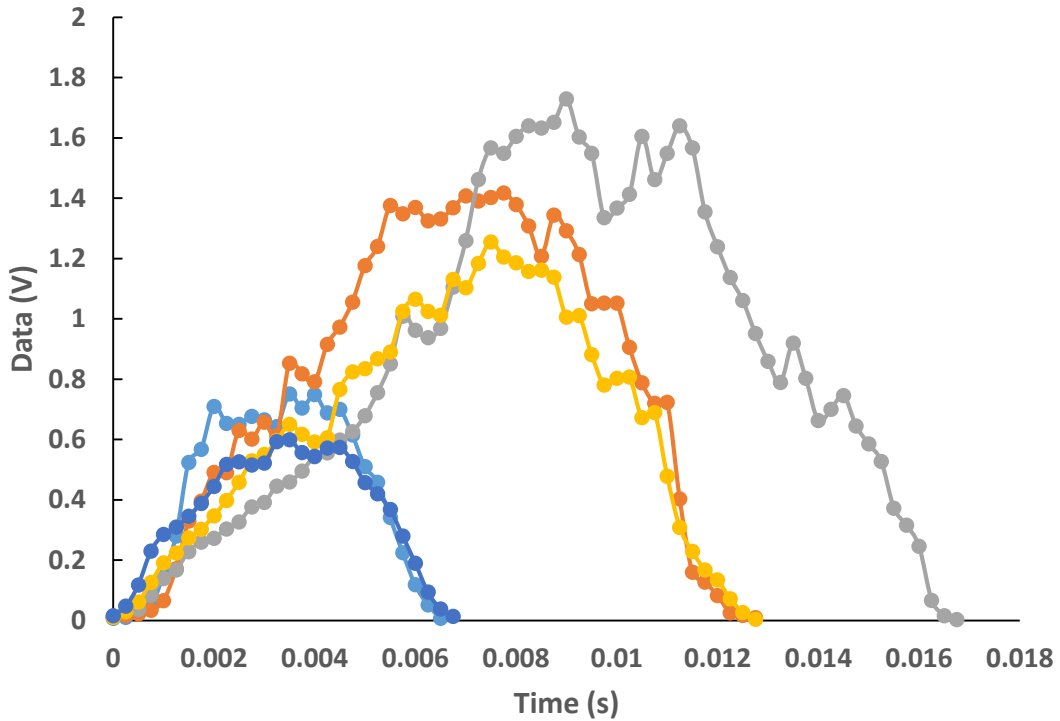


Figure 4.21 Experimental data for 600- μm particles at five different positions in the beam

Similarly, maximum voltages for the 600- μm particles read by the second photodiode, i.e., 1.37 volts for yellow and 0.73 volts for dark blue, were used in the calculations as shown in Table 4.3.

Table 4.3 Comparison of actual to predicted particle diameters for 600- μm particles passed at five different positions

Particles	Actual Diameter ($\pm 10\mu\text{m}$)	Predicted Diameter (μm)	Uncertainty (-%)
Gray	600	573	4.7
Orange	600	568	5.3
Yellow	600	563	6.2
Light Blue	600	563	6.2
Dark Blue	600	556	7.3

4.6 Conclusions

Tables 4.1 – 4.3 show that particle-sizing uncertainty is less than 10%, which agrees with our uncertainty analysis for 500- and 600- μm particles. In Figure 4.19, we can see that same-size particles, but different refractive indices, can be sized significantly differently if their scattered light is recorded at a 90° scattering angle. In order to accurately size the particles, it is recommended to use both photodiodes at $\pm 37^\circ$ to record the scattered light of the particles simultaneously. If the particle passes through the center of the beam, then both photodiodes will record identical or nearly identical outputs. In that case, the average value of the peak output voltages of the photodiodes should be used as the optimum output voltage in calculations. If the particle passes off-center of the beam, then the photodiodes will record different outputs. The output of the photodiode closer to the particle position in the beam will be higher due to the larger solid angle formed between the photodiode and the particle position in the beam. In this case, the output of the photodiode with the larger peak value should be used as the optimum value in calculations. To further confirm the consistency and repeatability of our measurements, we have included some more experimental data in Appendix A.

Chapter 5 - Determination of Size and Complex Index of Refraction of Single Particles

5.1 Optimum Scattering Angles

Considering the complex index of refraction of particles, actual differential-scattering cross-sections averaged over a 10° scattering angle are plotted for three different particle diameters and four different complex refractive indices using the Mie online program (Laven, 2010) as shown in Figures 5.1 - 5.4. It is important to acknowledge the effects of the imaginary part of the refractive index, κ , become significant only if its product to the size parameter, $\pi d/\lambda$, also defined as κkR (G. Wang, Chakrabarti, & Sorensen, 2015), is greater than or equal to 0.1, i.e., $\kappa kR \geq 0.1$, where λ is the wavelength, R is the radius of the particle, and k is the wave number. In Figures 5.1 - 5.4, we can see a strong functional relationship with the complex refractive index, and the differential-scattering cross-section, $dC/d\Omega$, is relatively independent of κ at a scattering angle of $115 \pm 5^\circ$. However, it depends on both the real and the imaginary components at other angles, but its dependence is more consistent and distinguishable at $80 \pm 5^\circ$, which also agrees with Figure 4.4. Using actual values of $dC/d\Omega$, Eq. (4.10) is modified to consider the dependence on κ at 37° , and two other equations are found for the $dC/d\Omega$ vs. particle diameter for the 80° and 115° scattering angles.

This work is limited to spheres. Calculations for non-spherical particles are more labor intensive and will be pursued in the future. Nevertheless, it is worthwhile to note non-spherical particle light-scattering has many properties semi-quantitatively similar to those of spheres including a strong forward-scattering diffraction regime, a hump regime as uncovered by Q-space analysis (Sorensen, 2013), and enhanced backscattering. See for example (Heinson et al., 2016).

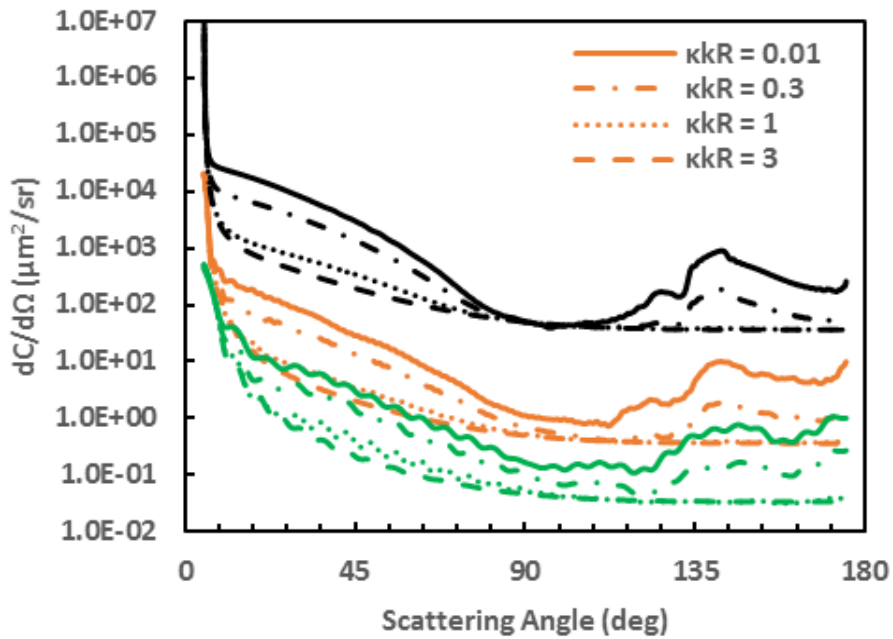


Figure 5.1 Average differential-scattering cross-section over a 10° scattering angle for $m = 1.33 + ik$ and three different particle diameters (5-, 17- and 170- μm), the legend in orange is also valid for the same line types in black and green.

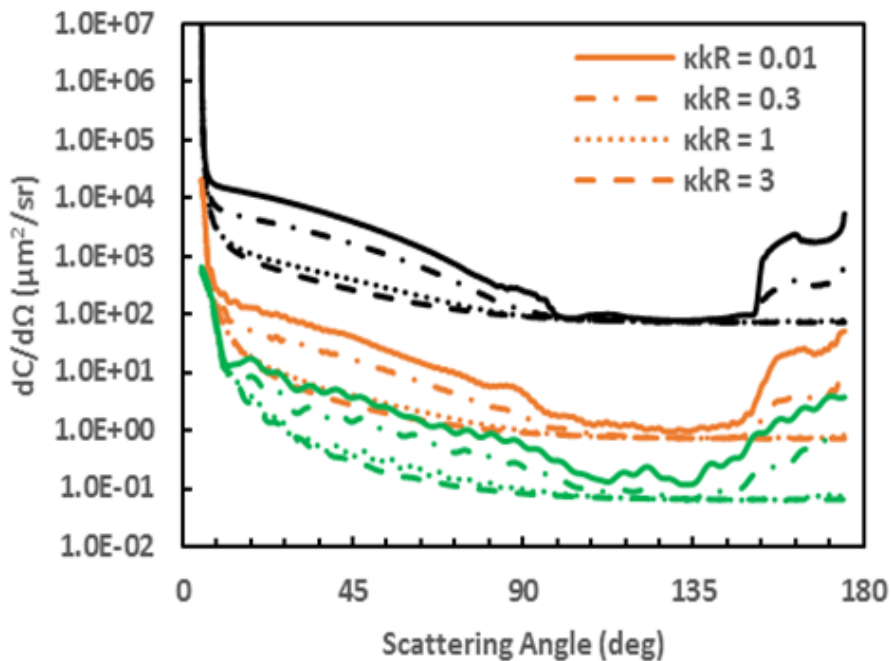


Figure 5.2 Average differential-scattering cross-section over a 10° scattering angle for $m = 1.5 + ik$ and three different particle diameters (5-, 17- and 170- μm), the legend in orange is also valid for the same line types in black and green.

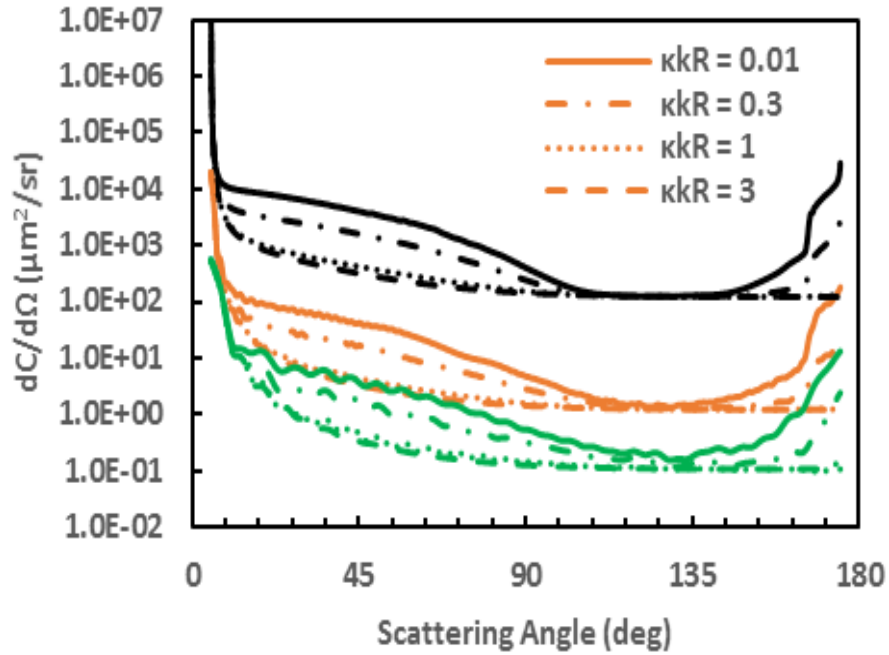


Figure 5.3 Average differential-scattering cross-section over a 10° scattering angle for $m = 1.7 + i\kappa$ and three different particle diameters (5-, 17- and 170- μm), the legend in orange is also valid for the same line types in black and green.

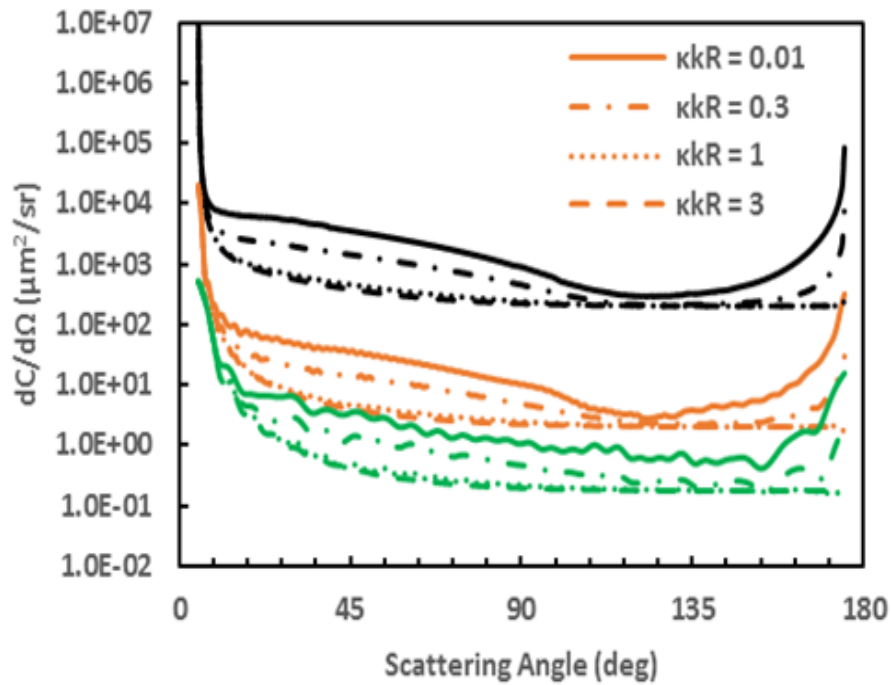


Figure 5.4 Average differential-scattering cross-section over a 10° scattering angle for $m = 2 + i\kappa$ and three different particle diameters (5-, 17- and 170- μm), the legend in orange is also valid for the same line types in black and green.

To modify Eq. (4.10), the coefficient, 0.18, is replaced by a coefficient, C_1 , which is the differential-scattering cross-section normalized by d^2 , and is now a function of κ . Figure 5.5 shows the variation of the coefficient C_1 as a function of κkR . The curve fit line is on the top of the data points for $\kappa kR = 0.1$; however, it is in the bottom of the data points for $\kappa kR = 0.3$ and 1, which is due to some uncertainties in the fitted equation. In fact, this is the best fit we can get for these data points, which still has a good functionality.

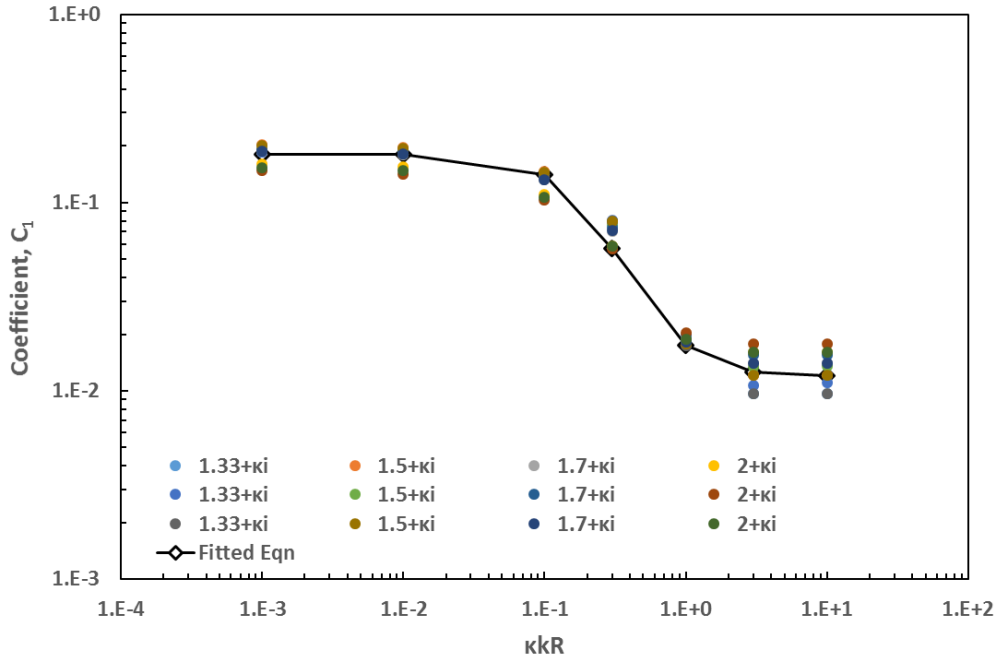


Figure 5.5 Variation of coefficient, C_1 vs. κkR for particle diameters ($d = 17, 170,$ and $500 \mu\text{m}$), and different refractive indices

In Figure 5.5, C_1 represents the $dC/d\Omega$ at a 37° scattering angle normalized by the square of particle diameter. Thus, it is a dimensionless parameter. Eq. (5.1) shows the fitted equation for C_1 .

$$C_1 = \frac{0.168}{30 * (\kappa kR)^2 + 1} + 0.012 \quad (5.1)$$

Now, Eq. (5.1) can be substituted for the coefficient of Eq. (4.10) to obtain Eq. (5.2).

$$dC/d\Omega (37^\circ) = \left[\frac{0.168}{30 * (\kappa kR)^2 + 1} + 0.012 \right] d^2 \quad (5.2)$$

For the 80° scattering angle at which the differential-scattering cross-section depends on both real and imaginary parts of the refractive index and the diameter, using Figure 5.6, an equation is fitted in the form of Eq. (5.3). To decrease the uncertainty and help for the curve fitting, in Figure 5.6, differential-scattering cross-section was normalized by d^2 and $(\kappa kR)^{-0.38}$. The power -0.38 was obtained by trial and error as an optimum value that made the data points closer and hence reduced the error in the fitted equation.

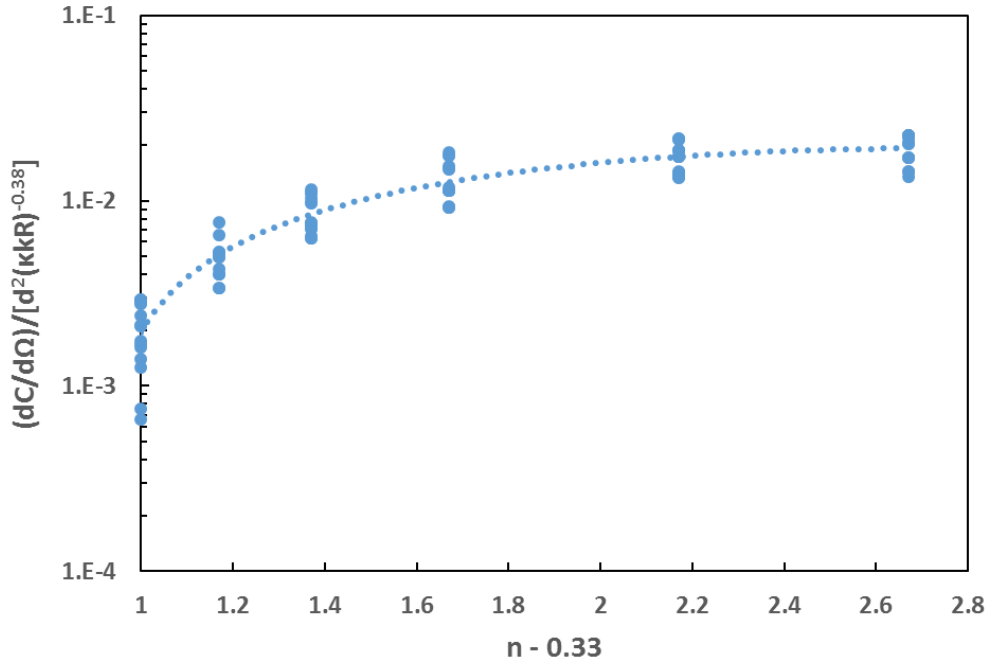


Figure 5.6 $(dC/d\Omega)/[d^2(\kappa kR)^{-0.38}]$ vs $(n - 0.33)$ at 80° scattering angle for 17-, 170-, and 500- μm particles with $\kappa kR = (0.01, 0.1, 0.3, 1 \ \& \ 3)$

$$dC/d\Omega (80^\circ) = [-0.0056(n - 0.33)^2 + 0.031(n - 0.33) - 0.0233]d^2(\kappa kR)^{-0.38} \quad (5.3)$$

Similarly, for the 115° scattering angle at which the differential-scattering cross-section depends only on the real part of the refractive index, using Figure 5.7, an equation is fitted in the form of Eq. (5.4). Differential-scattering cross-section was normalized by $d^{1.9}$ as an optimum value to get the points closer and make the best curve fit.

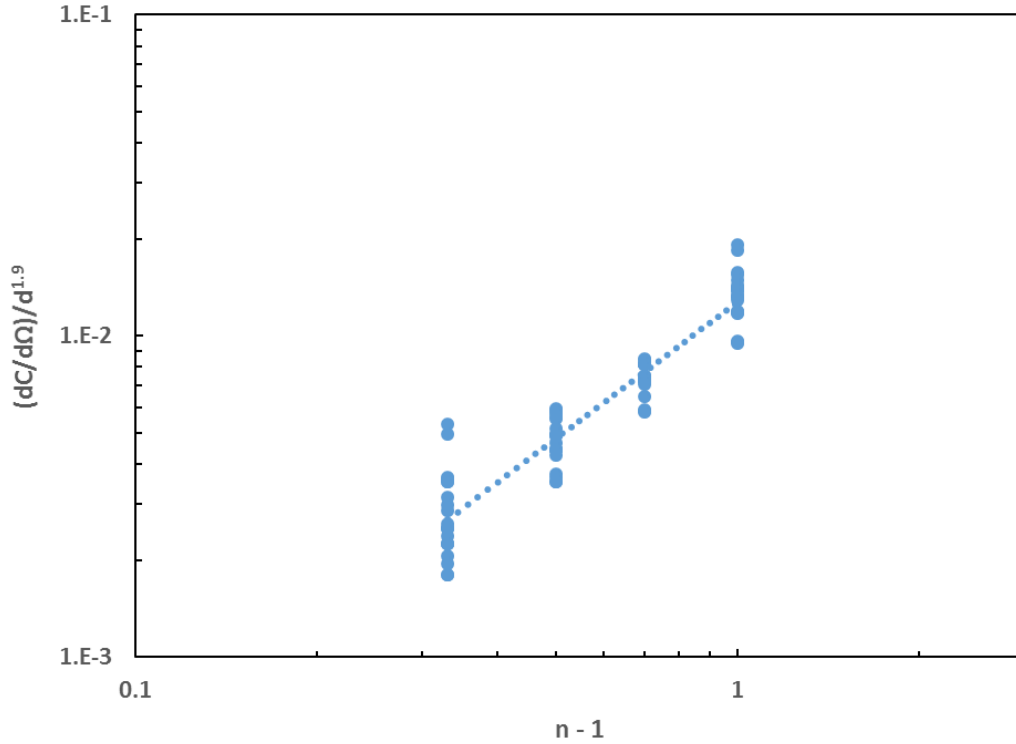


Figure 5.7 $(dC/d\Omega)/d^{1.9}$ vs $(n-1)$ at 115° scattering angle for (17-,170- and 500- μm) particles

$$dC/d\Omega (115^\circ) = 0.0127(n - 1)^{1.4}d^{1.9} \quad (5.4)$$

Combining Eqs. (4.4), (4.7), (4.9), and (5.2), we get

$$V_i(37^\circ) = \frac{2P_{Tot}}{\pi w^2} e^{-(d_3 - vt_i)^2/2w^2} \left[\frac{0.168}{30 * (\kappa k R)^2 + 1} + 0.012 \right] d^2 \Omega_i R(\lambda) K \quad (5.5)$$

Combining Eqs. (4.4), (4.7), (4.9), and (5.3), we get

$$V_i(80^\circ) = \frac{2P_{Tot}}{\pi w^2} e^{-(d_3 - vt_i)^2 / 2w^2} [-0.0056(n - 0.33)^2 + 0.031(n - 0.33) - 0.0233] d^2 (\kappa k R)^{-0.38} \Omega_i R(\lambda) K \quad (5.6)$$

Combining Eqs. (4.4), (4.7), (4.9), and (5.4), we get

$$V_i(115^\circ) = \frac{2P_{Tot}}{\pi w^2} e^{-(d_3 - vt_i)^2 / 2w^2} [0.0127(n - 1)^{1.4}] d^{1.9} \Omega_i R(\lambda) K \quad (5.7)$$

Eqs. (5.5), (5.6), and (5.7) can be solved simultaneously and iteratively to determine diameter d of the particle, $\kappa k R$, and the real part of the refractive index, n . Once $\kappa k R$ and d have been determined, we can simply predict κ . To iteratively solve these non-linear system of equations, we used the well-known Newton's method of iteration. It took six iterations or less for the models to converge.

5.2 Experiments

In order to validate the theory and our developed mathematical models, we conducted some experiments on droplets of two different solutions, i.e., nigrosine solution-water and nigrosine powder-toluene. Initially, we dissolved nigrosine solution in water and nigrosine powder in toluene at different concentrations. Then we measured scattered-light intensities by droplets of each solution for the three different scattering angles. We then used the peak scattered intensities with the total time of flights to iteratively solve for, d , n , and $\kappa k R$. As a prerequisite test, we experimentally measured the κ for different concentrations of nigrosine-to-water and nigrosine-to-toluene solutions in order to have some known values of κ to compare to the predicted values

iteratively obtained by our mathematical models. The real refractive index, n , is 1.33 for water and 1.497 for toluene. Since a small amount of nigrosine was mixed with water and toluene, and the mole fraction of nigrosine was very small compared to the mole fractions of water and toluene, we didn't notice any changes in the real part, n , of each solution and thus the values of n for water and toluene remained the same. Monodisperse droplets of these solutions were generated by nanofil syringes and needles that were measured under a microscope before they were released from the needle tip. Once actual values of n , κ , and d had been determined, they were then compared to the predicted values iteratively obtained by our models. The experimental procedures are explained in detail as follows.

5.2.1 Measuring the Imaginary Part of the Refractive Index, κ

For each solution, κ was measured using a light-extinction mechanism (Baron & Willeke, 2001). The schematic diagram and actual picture of the setup are shown in Figures 5.8 and 5.9, respectively.

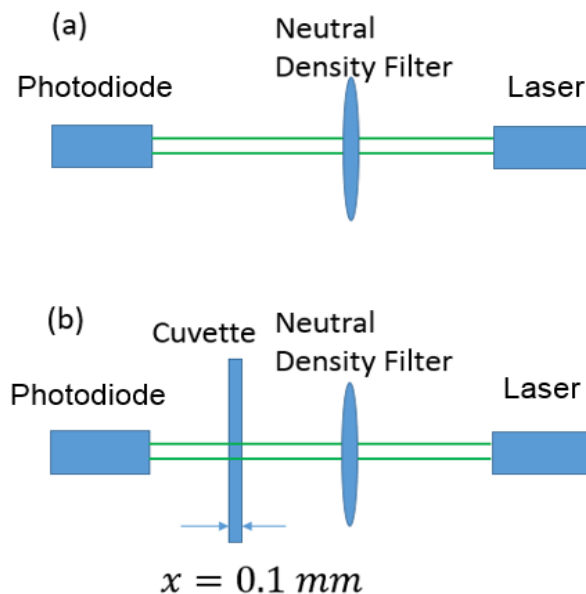


Figure 5.8 Schematic of the setup for measuring κ , (a) without solution, (b) with solution

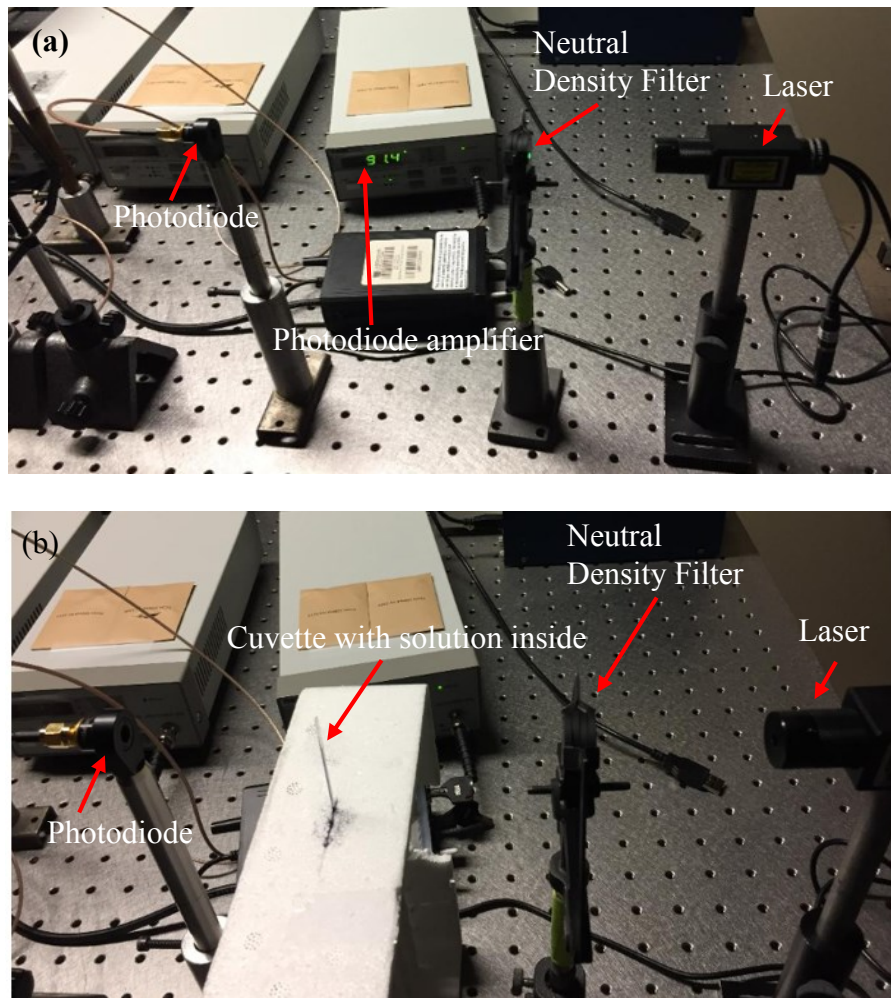


Figure 5.9 Picture of the setup for measuring κ , (a) without solution, (b) with solution

The experimental setup has a 532-nm wavelength laser, a neutral density filter to attenuate the light in order to protect the photodiode from saturation, and a photodiode to record light intensity. In Figure 5.9 (a), the photodiode recorded the initial intensity, I_0 , and in Figure 5.9 (b), the photodiode recorded the light intensity, I_1 , after a 0.1-mm cuvette with the solution inside was placed along the beam. Then the parameters were related using Lambert Beer's law in order to find κ .

$$I_1 = I_0 e^{\frac{-x}{x_0}} \quad (5.8)$$

$$\kappa = \frac{\lambda}{2\pi x_0} \quad (5.9)$$

Eq. (5.8) was solved for x_0 and then Eq. (5.9) was solved for κ . Figures 5.10 and 5.11 show the values of κ for different concentrations of nigrosine solution-to-water and nigrosine powder-to-toluene, respectively. The $\pm 9\%$ uncertainty indicates the resolution error due to photodiode readings for I_0 and I_1 .

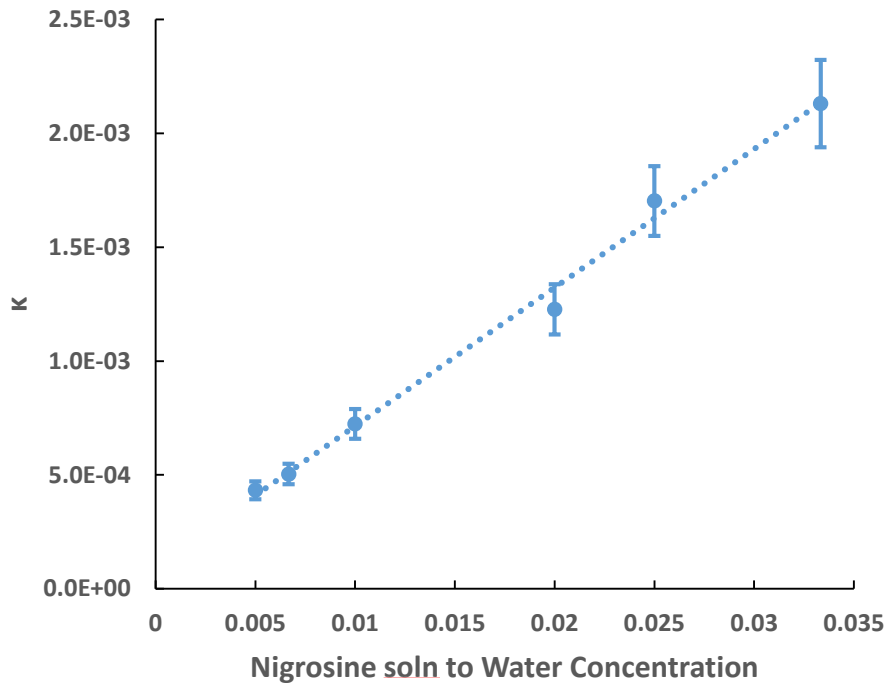


Figure 5.10 Imaginary part of the refractive index, κ vs. nigrosine solution-to-water concentration ($\kappa \pm 9\%$)

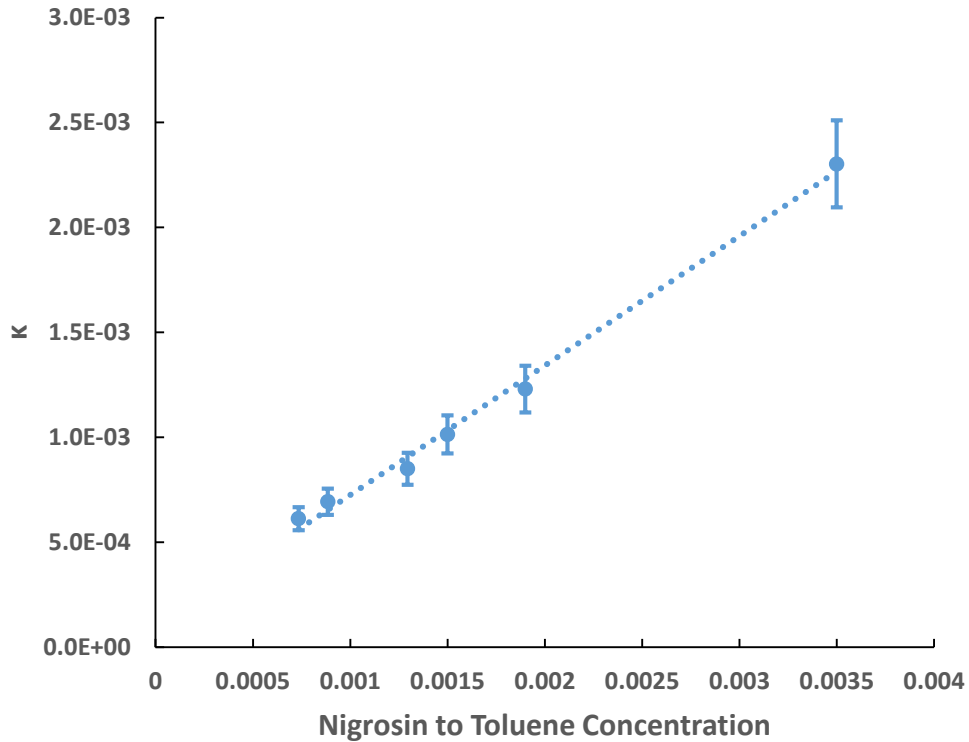


Figure 5.11 Imaginary part of the refractive index, κ vs. nigrosine powder-to-toluene concentration ($\kappa \pm 9\%$)

In Figures 5.10 and 5.11, we can see that κ increases with concentration. This means the higher the nigrosine concentration, the darker the solution and hence the higher the absorption. In other words, as the nigrosine concentration goes to zero, i.e., pure water and pure toluene, κ approaches to zero as well, which indicates the value of κ is very small or close to zero for water and toluene.

As mentioned previously, the values of κ become significant only if $\kappa kR \geq 0.1$. In order to choose the optimum values of κkR for our experiments, we plotted the % difference between the actual values and theoretically calculated values of κkR using our models for known values of n and d , as can be seen in Figure 5.12.

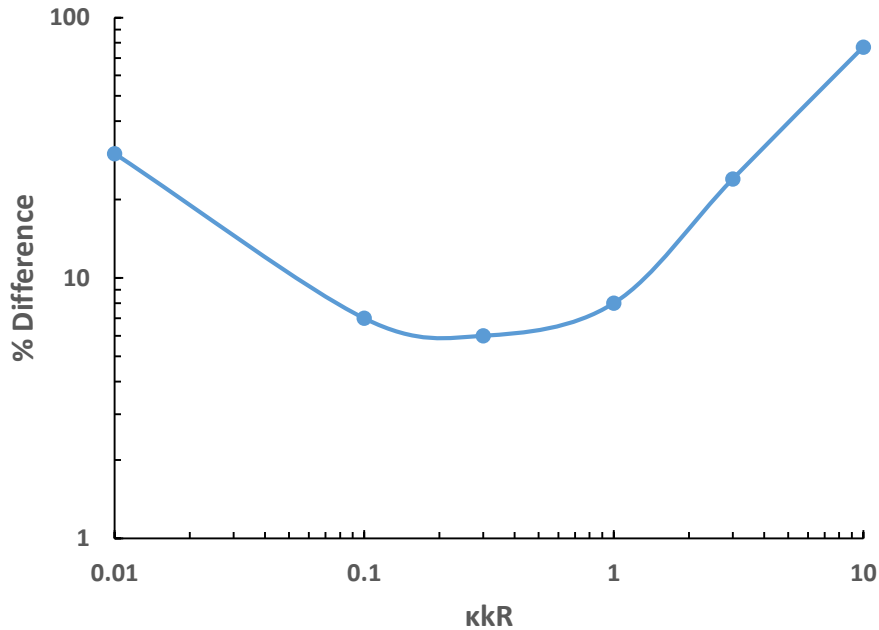


Figure 5.12 Percent difference between actual and predicted values of $\kappa\kappa R$ for a 100- μm particle with $m = 1.6 + i\kappa$

In Figure 5.12, we can see the smallest percent difference for $\kappa\kappa R$ is when $0.1 \leq \kappa\kappa R \leq 1$. Since $\kappa\kappa R$ depends on droplet diameter, we have plotted the values of $\kappa\kappa R$ vs. droplet diameter for different concentrations of nigrosine-to-water and nigrosine-to-toluene solutions as shown in Figures 5.13, and 5.14, respectively. From these figures, we can choose the solution concentration in order to get the optimum values of $\kappa\kappa R$ for our experiments based on the known droplet diameter.

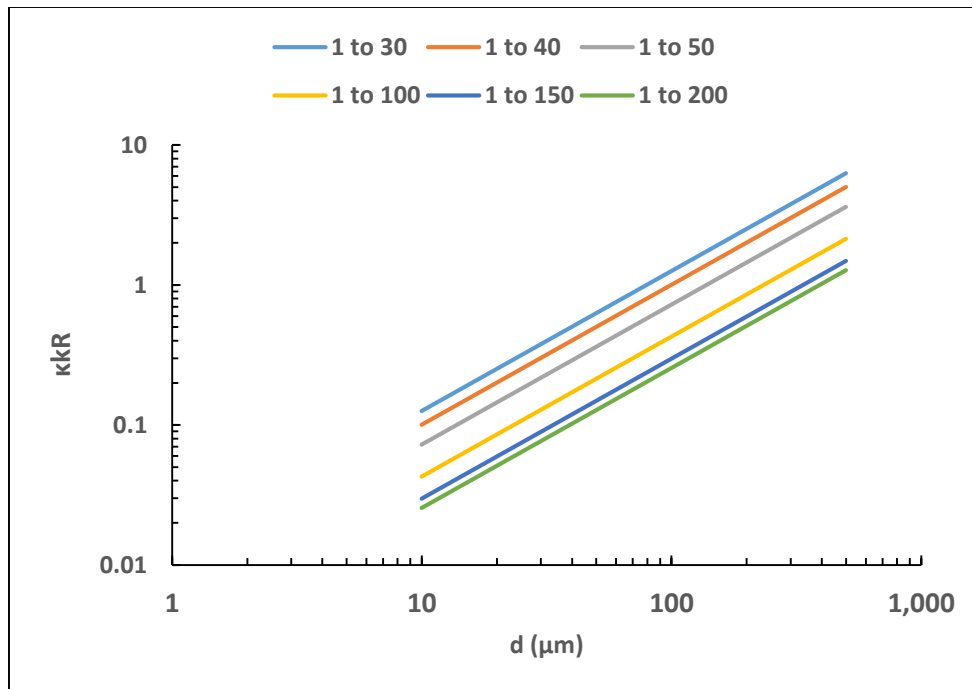


Figure 5.13 $\kappa k R$ vs. droplet diameter for different nigrosine solution-to-water concentrations

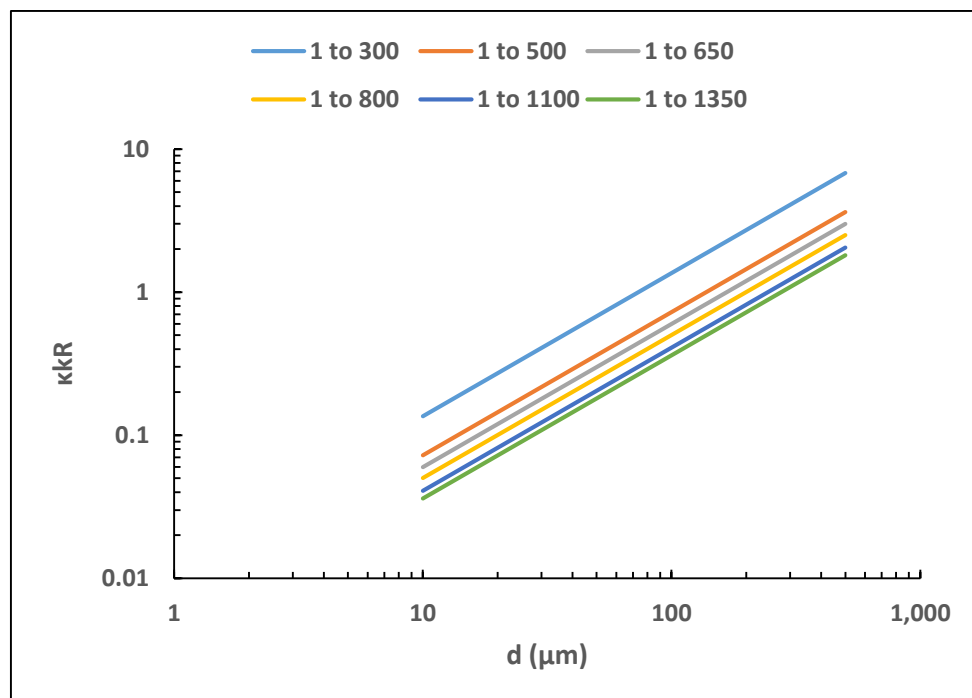


Figure 5.14 $\kappa k R$ vs. droplet diameter for different nigrosine-to-toluene concentrations

5.2.2 Light-Scattering Experimental Setup

In order to detect the scattered light by droplets at three scattering angles, we modified the experimental setup in Chapter 4 by adding a focusing lens and two more photodiodes at 80° and 115° scattering angles as shown in Figure 5.15.

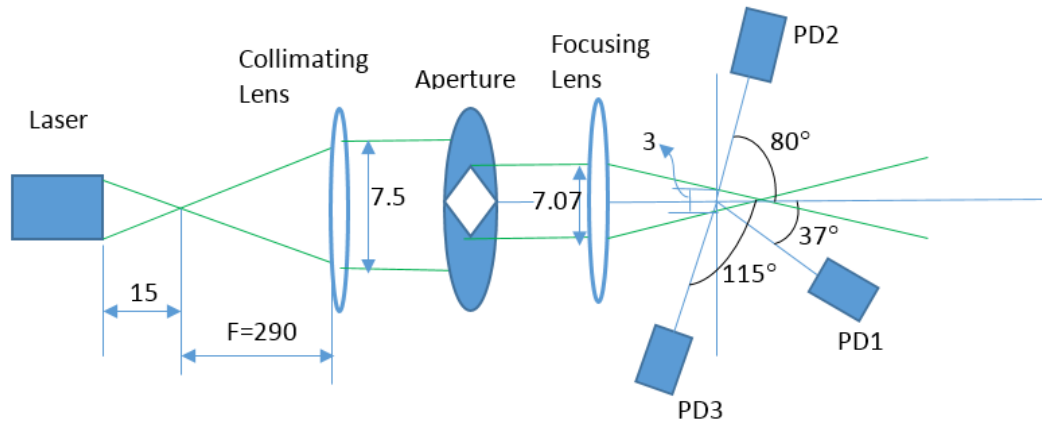


Figure 5.15 Schematic diagram of light-scattering experimental setup, dimensions (mm)

The experimental setup uses a Laserglow BDG005XXX, 5-mW, 532-nm wavelength laser as a light source to illuminate the particles; a collimating lens with a focal length of 290 mm to collimate the beam and make it uniform in diameter of 7.5 mm; an aperture to make a diamond-shaped beam profile with dimensions of 5mm x 5mm; and three Thorlabs SM05PD1A photodiodes with a responsivity of $R(532\text{ nm}) = 0.32\text{ A/W}$ positioned at 37°, 80°, and 115° scattering angles to detect the scattered light by particles simultaneously for as long as the particles were in the beam. The photodiodes have an active area of 13 mm² and were positioned at a distance of 18 mm from the center of the beam, so they made a solid angle of 0.04 steradian corresponding to the center of the beam. Three Thorlabs PDA200C photodiode amplifiers with a conversion coefficient of $1 \times 10^7\text{ V/A}$ were used to display the scattered-light signal detected by the

photodiodes. A National Instruments (NI) SCXI-1000 data acquisition system was connected to the photodiode amplifiers and LabVIEW program to record the data. A nanofil syringe with a 36G beveled-shape needle (35- μm inner diameter and 120- μm outer diameter) was used to drop a droplet of nigrosine-water solution or nigrosine-toluene solution on a 3-mm focused beam. Additionally, a ramp with a hole was used overhead of the photodiodes so the luer lock of the needle fitted in the hole and made the syringe stable, which helped the droplets pass through the exact position of the beam. Further information about the equipment is provided in Figures 5.16 – 5.19.

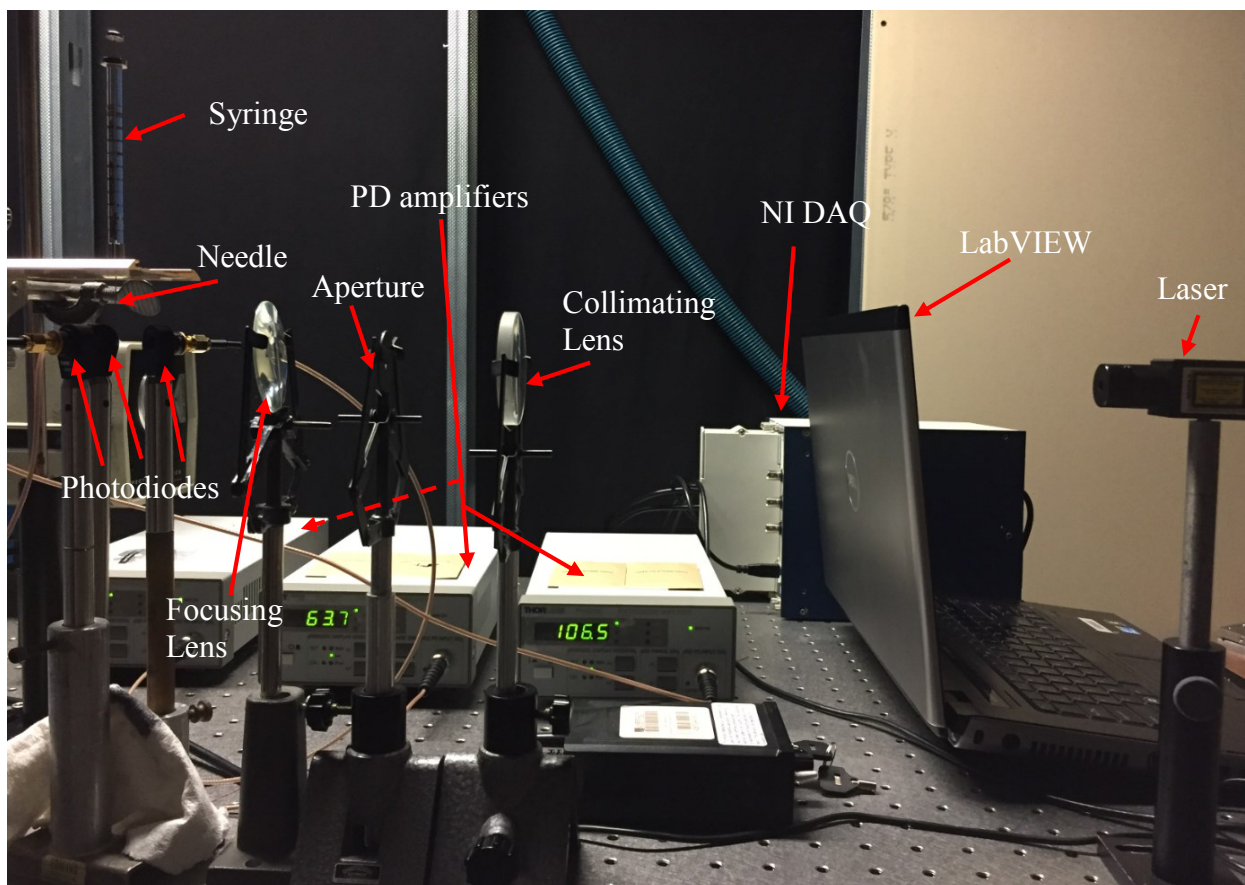


Figure 5.16 Picture of the light-scattering experimental apparatus

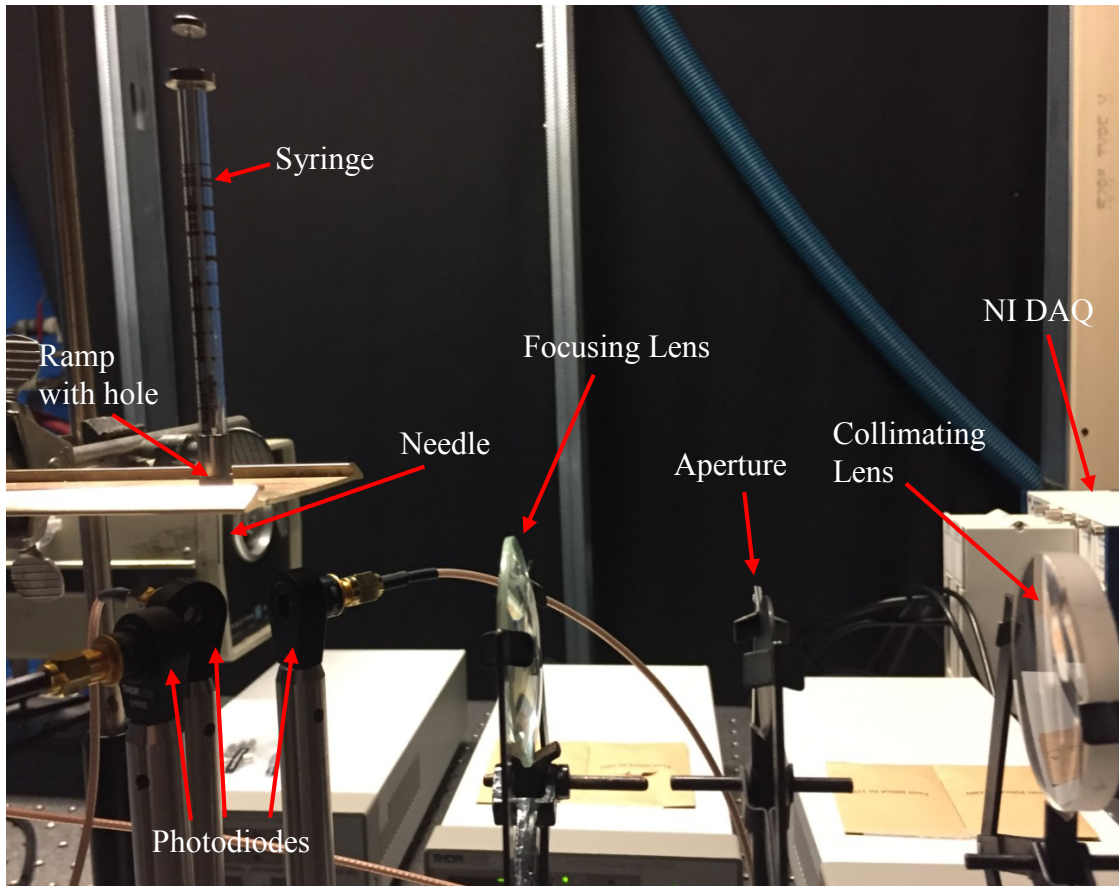


Figure 5.17 Portion of the light-scattering experimental apparatus

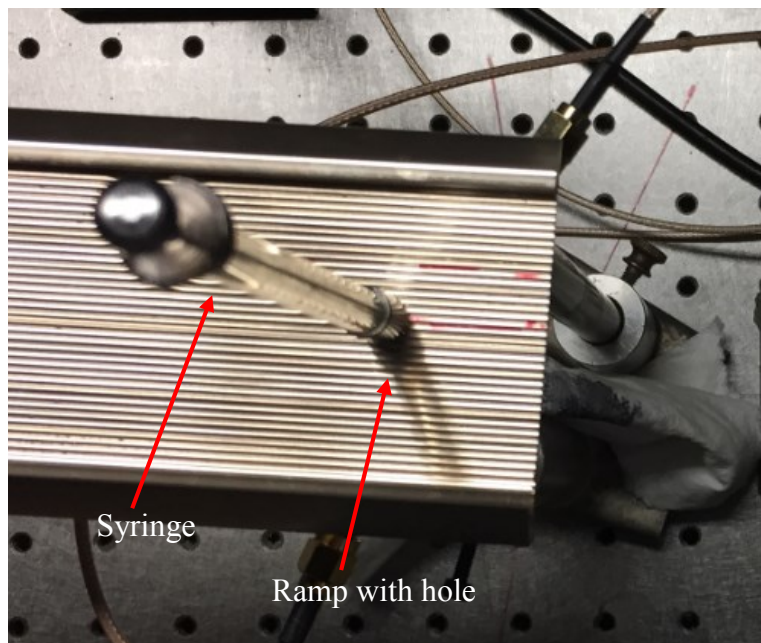


Figure 5.18 Portion of the experimental apparatus (top view)

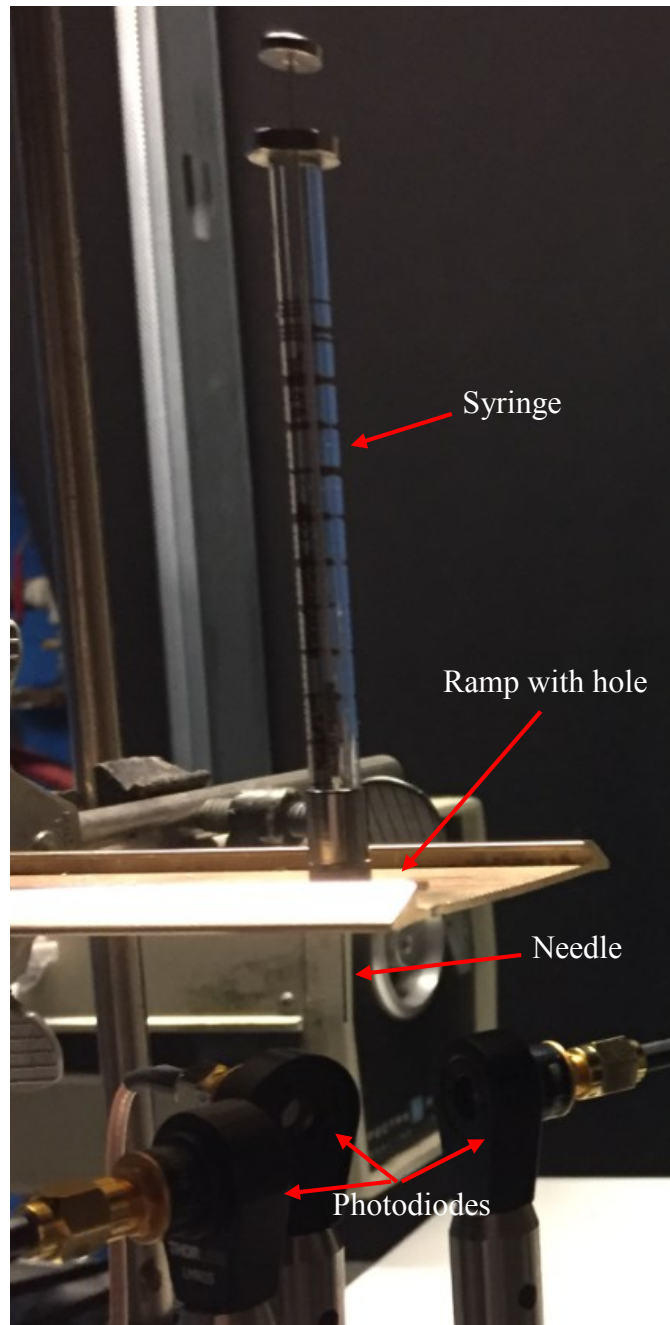


Figure 5.19 Portion of the experimental apparatus (side view)

5.3 Results and Discussion

To validate this research and compare the experimental results to the theory, we conducted some experiments on droplets of solutions of nigrosine-to-water and nigrosine-to-toluene of known n and κ . The droplets were measured 300 μm in diameter for the solution of nigrosine-to-water and 220 μm in diameter for the solution of nigrosine-to-toluene by a microscope with a resolution of 10 μm just before they were dripped off the tip of a 35 μm in diameter needle. We dropped the droplets through the center of the beam, which was focused to 3 mm as shown in Figure 5.15. The photodiodes positioned at 37°, 80°, and 115° scattering angles, recorded instantaneously the scattered-light intensity and time of flight for each droplet as shown in Figures 5.20 – 5.29 for the solution of nigrosine-to-water and in Figures 5.30 – 5.39 for the solution of nigrosine-to-toluene. These data were selected based on the longest time of flight. Since the beam dimension was largest at the center, it was assumed the particles with the longest time of flight should have passed through the center. The velocity of the droplets was calculated as 0.485 mm/ms for the droplets being released at a height of 12 mm on the beam. With the beam dimension of 3 mm at the center, time of flight was about 6 ms for the particles to pass through the center of the beam. Since the photodiodes, PD1, PD2, and PD3, were positioned at identical solid angles from the center of the beam, the droplets were dropped at the center of the beam. In this particular setup, if the droplets were dropped at any other positions of the beam, then the solid angles would increase/decrease with PD1 and PD3, and decrease/increase with PD2 as they were positioned at two opposite sides of the beam. This would make the photodiodes record unexpected outputs. In our experiments, we had to consider this geometry due to the space restrictions for the photodiode stands/holders on the optical table. However, to build the actual device, it is possible to position

all three photodiodes at one side of the beam since there will be no need for the photodiode stands/holders and the photodiodes will be unmounted as well.

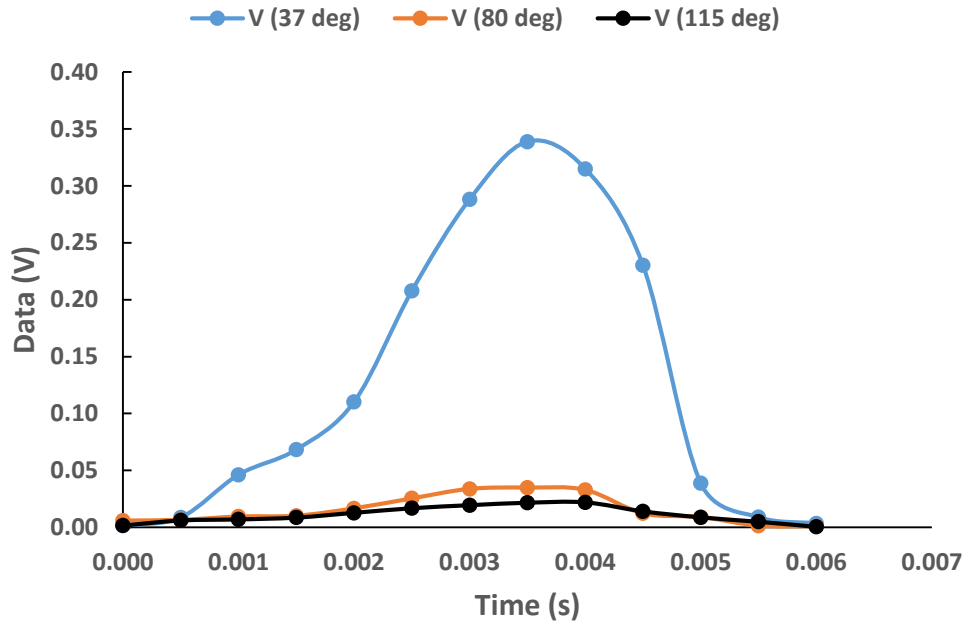


Figure 5.20 Photodiodes outputs vs. time of flight for a 300- μ m droplet of nigrosine solution to water (1:150)

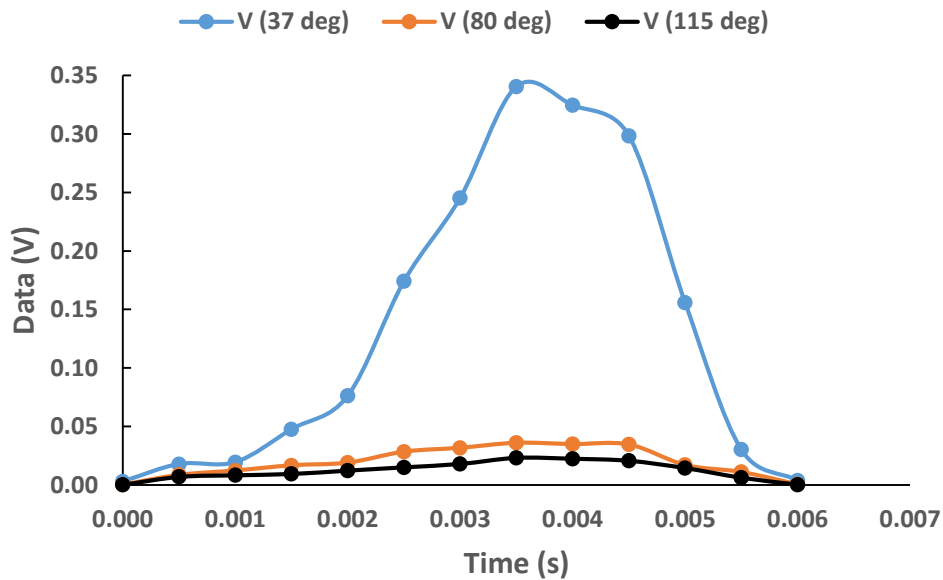


Figure 5.21 Photodiodes outputs vs. time of flight for a 300- μ m droplet of nigrosine solution to water (1:150)

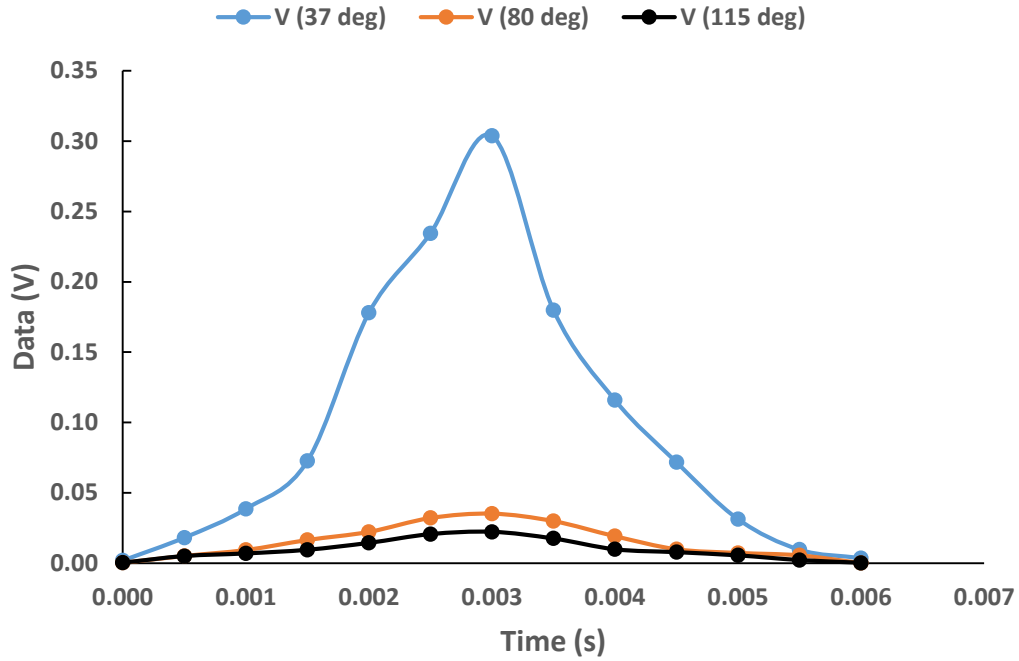


Figure 5.22 Photodiodes outputs vs. time of flight for a 300- μ m droplet of nigrosine solution to water (1:150)

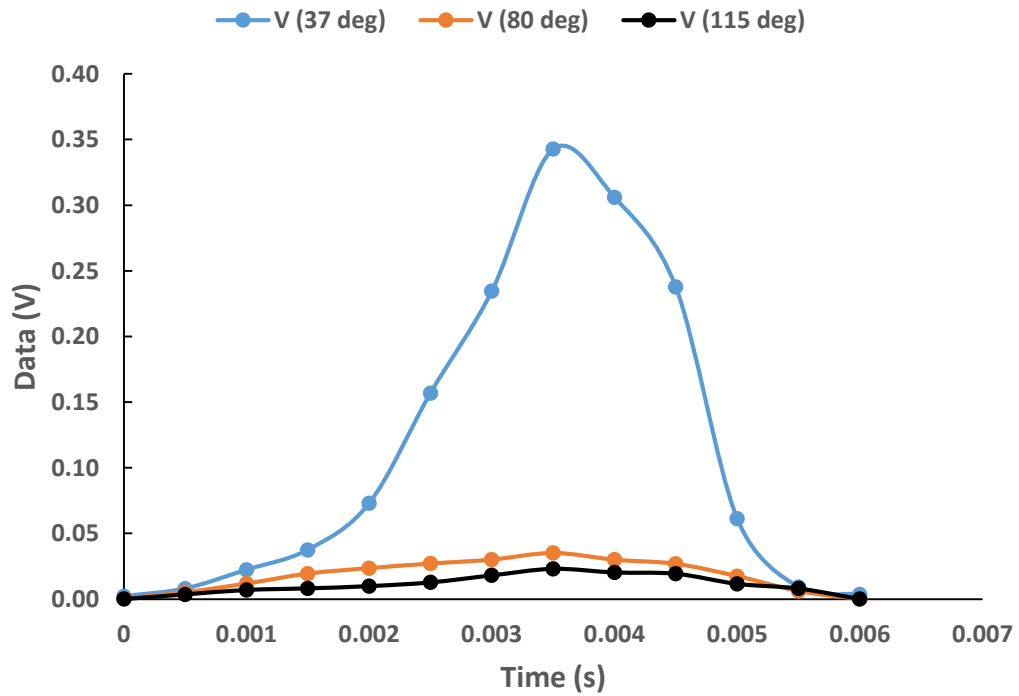


Figure 5.23 Photodiodes outputs vs. time of flight for a 300- μ m droplet of nigrosine solution to water (1:150)

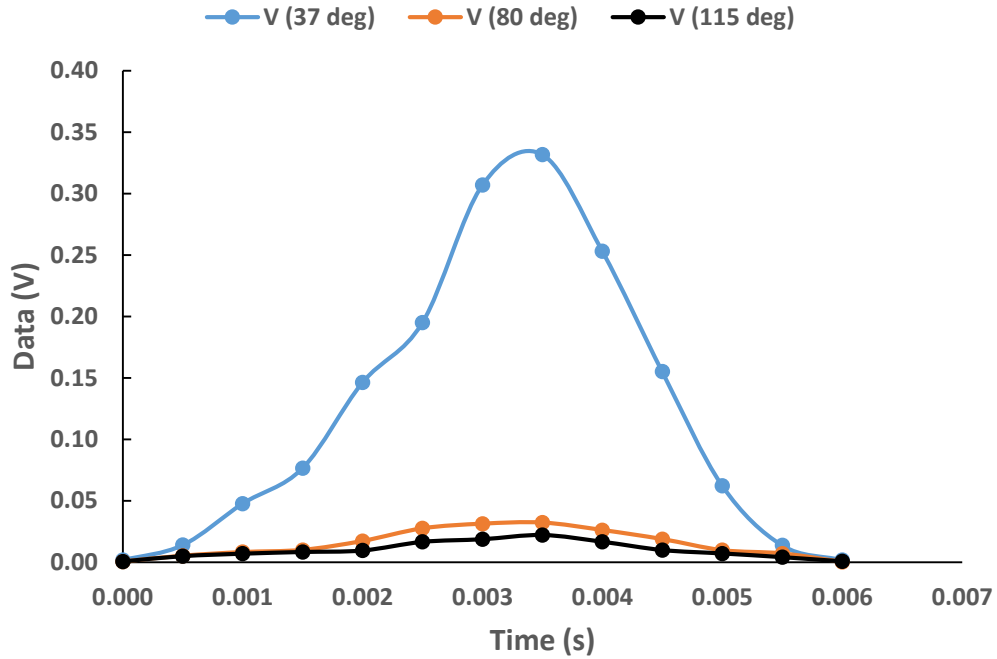


Figure 5.24 Photodiodes outputs vs. time of flight for a 300- μ m droplet of nigrosine solution to water (1:150)

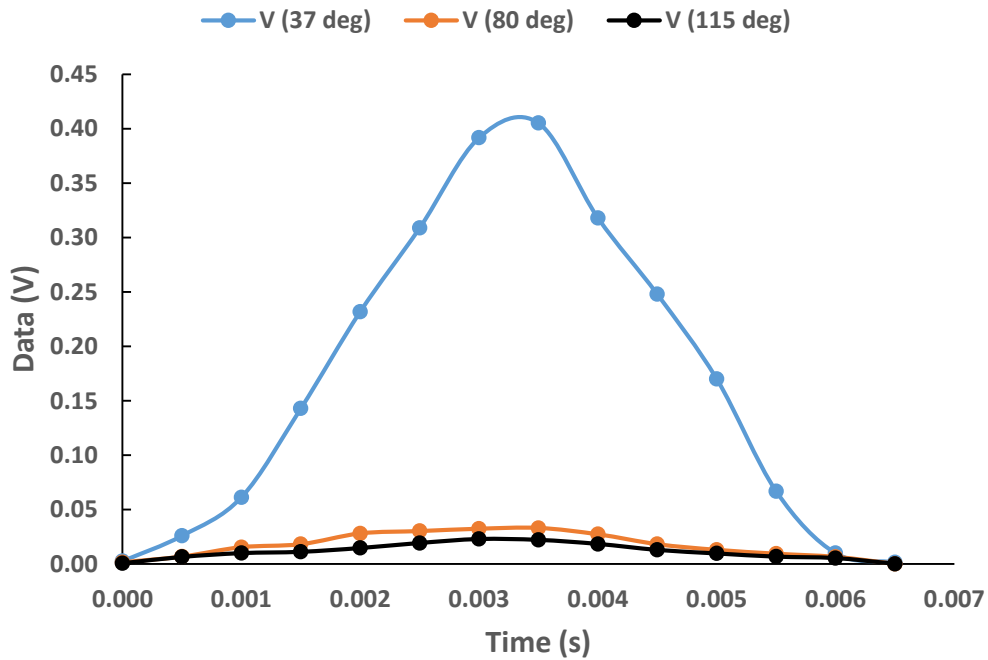


Figure 5.25 Photodiodes outputs vs. time of flight for a 300- μ m droplet of nigrosine solution to water (1:200)

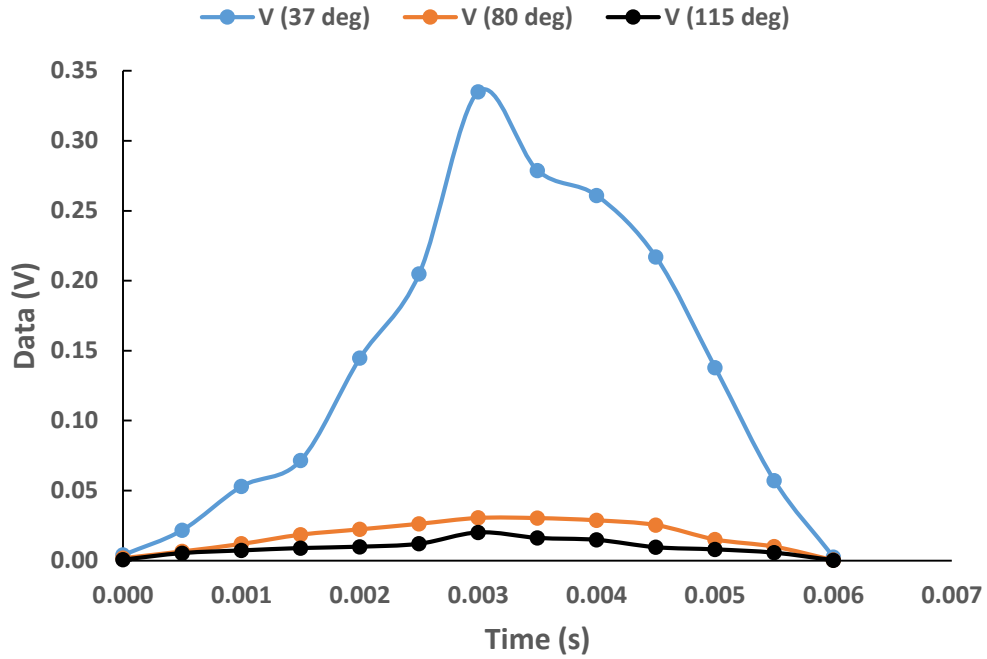


Figure 5.26 Photodiodes outputs vs. time of flight for a 300- μm droplet of nigrosine solution to water (1:200)

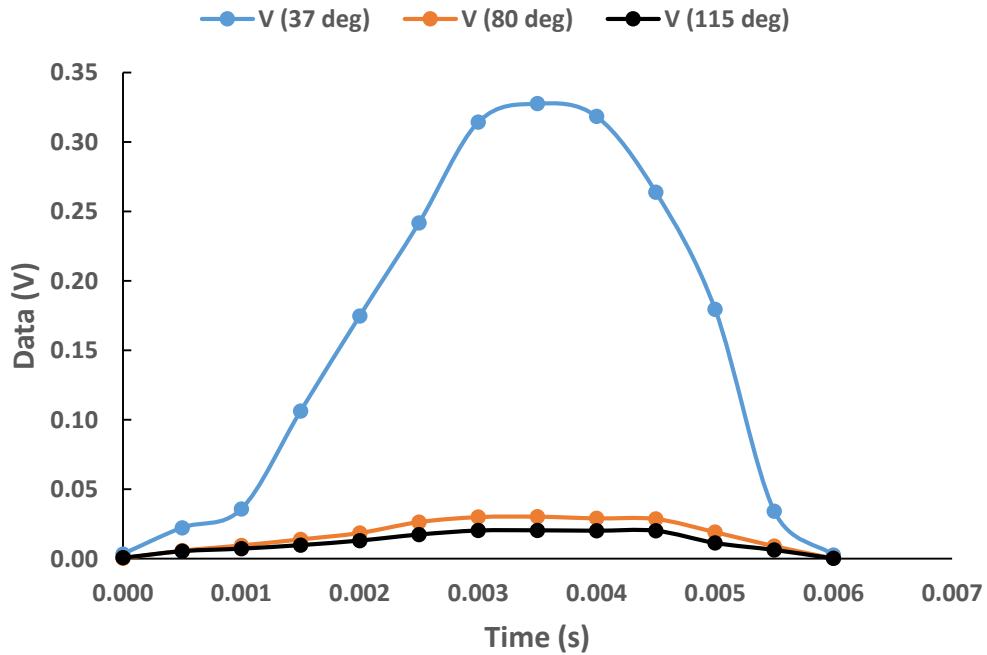


Figure 5.27 Photodiodes outputs vs. time of flight for a 300- μm droplet of nigrosine solution to water (1:200)

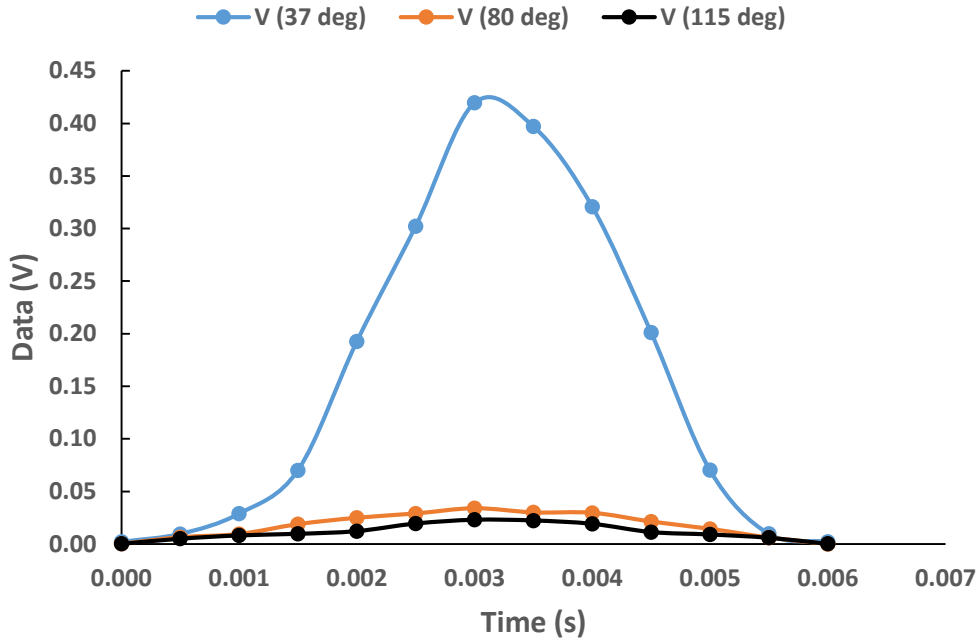


Figure 5.28 Photodiodes outputs vs. time of flight for a 300- μ m droplet of nigrosine solution to water (1:200)

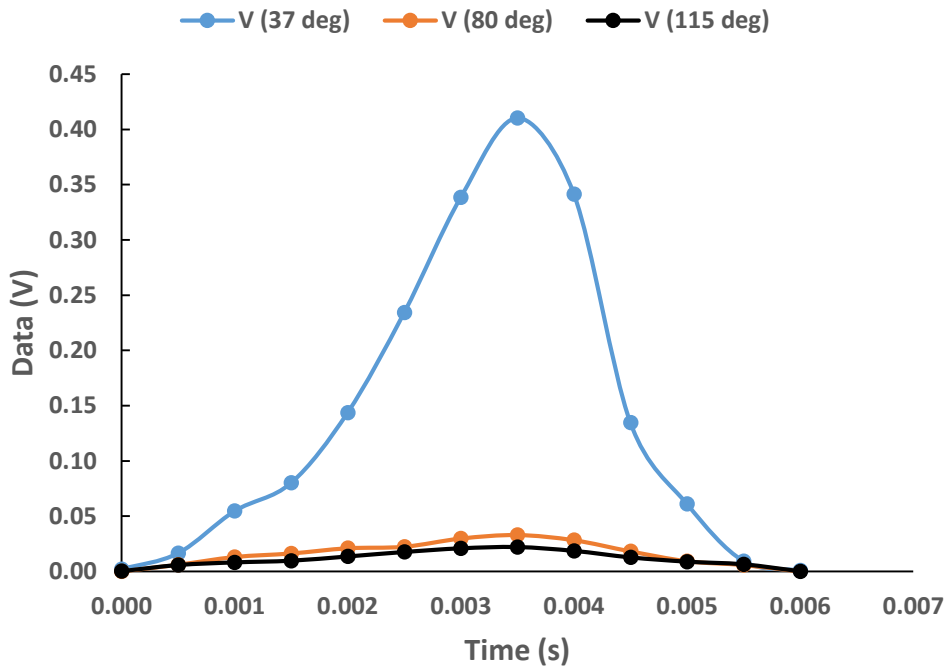


Figure 5.29 Photodiodes outputs vs. time of flight for a 300- μ m droplet of nigrosine solution to water (1:200)

Peak values of the output voltage and total time of flights in Figures 5.20 – 5.29 were used in Eqs. (5.5), (5.6), and (5.7) to iteratively solve for the droplet diameter, d , $\kappa\kappa R$, and n . Then, the predicted and the actual values were compared as summarized in Table 5.1. At most, it took six iterations for the models to converge.

Table 5.1 Comparison of actual to predicted values of droplet diameter, d , $\kappa\kappa R$, and n for nigrosine solution-to-water

Fig. (Conc.)	d_{actual} ($\pm 10 \mu\text{m}$)	d_{pred} (μm)	$\kappa\kappa R_{act}$ ($\pm 9 \%$)	$\kappa\kappa R_{pred}$	n_{actual}	n_{pred}	Uncertainty (%)		
							d	$\kappa\kappa R$	n
5.20 (1:150)	300	286.2	0.893	0.721	1.33	1.326	-5	-19	-0.3
5.21 (1:150)	300	286.7	0.893	0.714	1.33	1.329	-4	-20	0
5.22 (1:150)	300	275.5	0.893	0.747	1.33	1.336	-8	-16	+0.45
5.23 (1:150)	300	289.4	0.893	0.729	1.33	1.327	-4	-18	-0.23
5.24 (1:150)	300	285.5	0.893	0.732	1.33	1.318	-5	-18	-1
5.25 (1:200)	300	291.6	0.766	0.612	1.33	1.313	-3	-20	-1
5.26 (1:200)	300	274.2	0.766	0.653	1.33	1.317	-9	-15	-1
5.27 (1:200)	300	272.5	0.766	0.677	1.33	1.318	-9	-12	-1
5.28 (1:200)	300	296.7	0.766	0.615	1.33	1.311	-1	-20	-1
5.29 (1:200)	300	292.2	0.766	0.609	1.33	1.308	-3	-20	-2
RMS Average							5.72	17.98	0.97

We repeated the same experiments for the droplets of the solutions of nigrosine-to-toluene 220 μm in diameter of known n and κ to check for the validity of our models for a different material with a different refractive index. The results are shown in Figures 5.30 – 5.39, and the predicted and actual values are compared in Table 5.2.

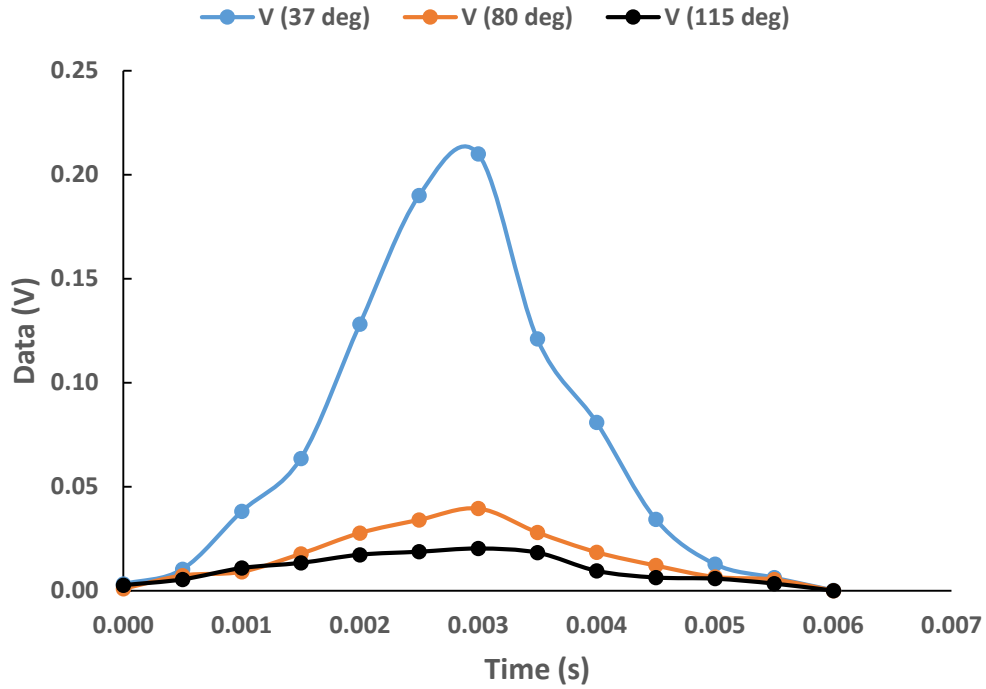


Figure 5.30 Photodiodes outputs vs. time of flight for a 220- μm droplet of nigrosine-toluene solution (1:1350)

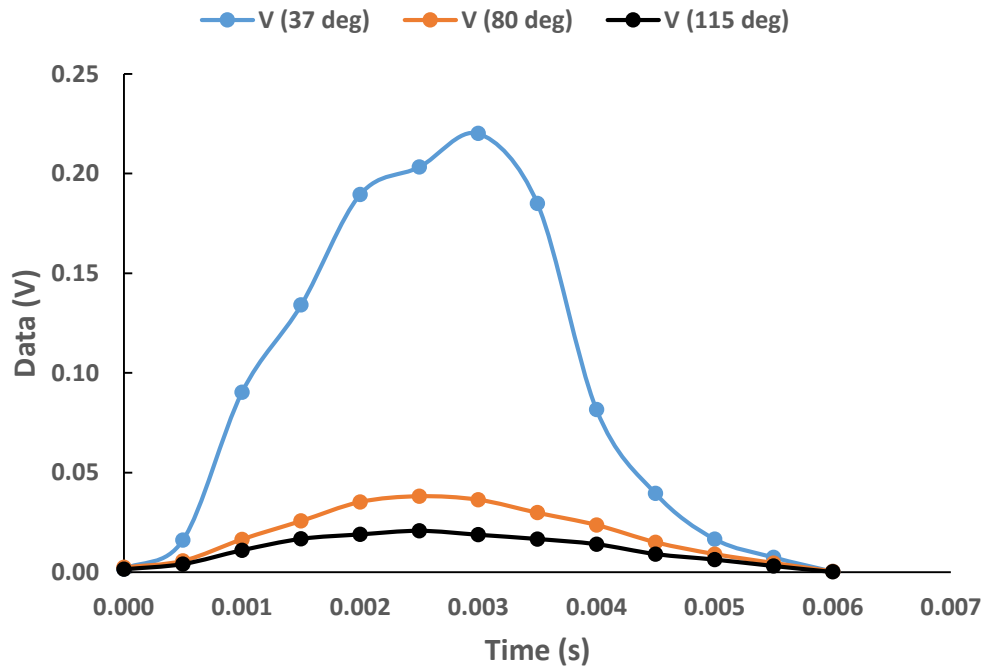


Figure 5.31 Photodiodes outputs vs. time of flight for a 220- μm droplet of nigrosine-toluene solution (1:1350)

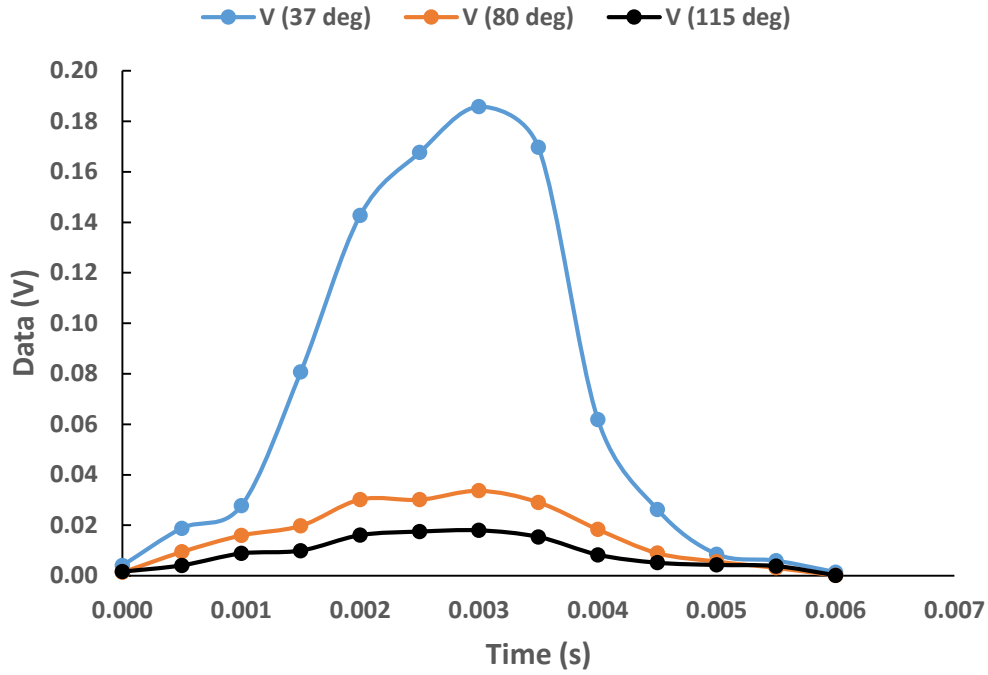


Figure 5.32 Photodiodes outputs vs. time of flight for a 220- μm droplet of nigrosine-toluene solution (1:1350)

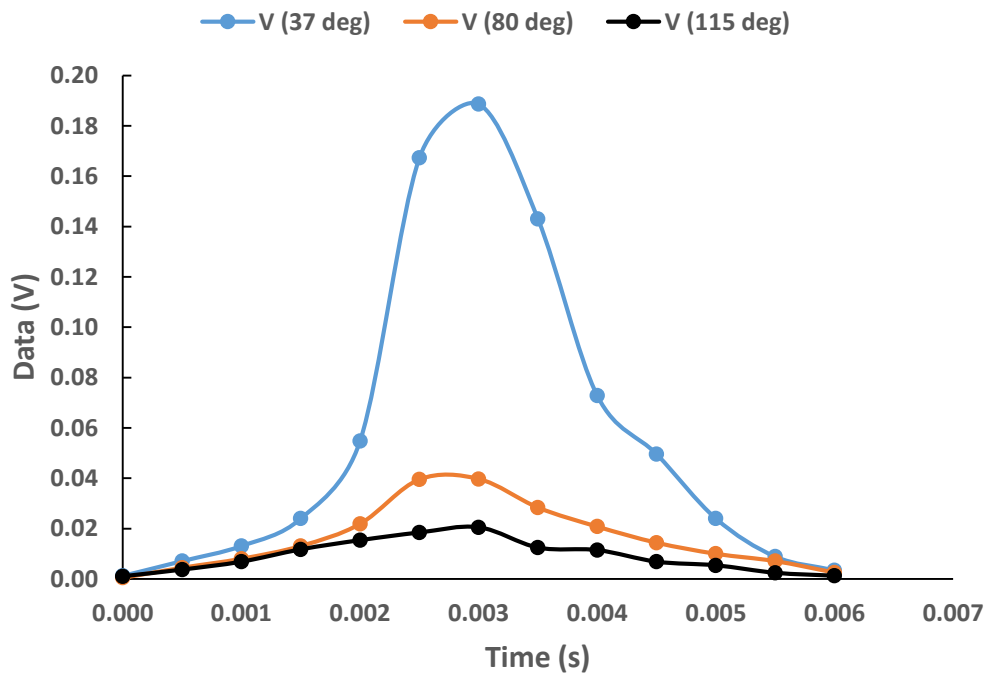


Figure 5.33 Photodiodes outputs vs. time of flight for a 220- μm droplet of nigrosine-toluene solution (1:1350)

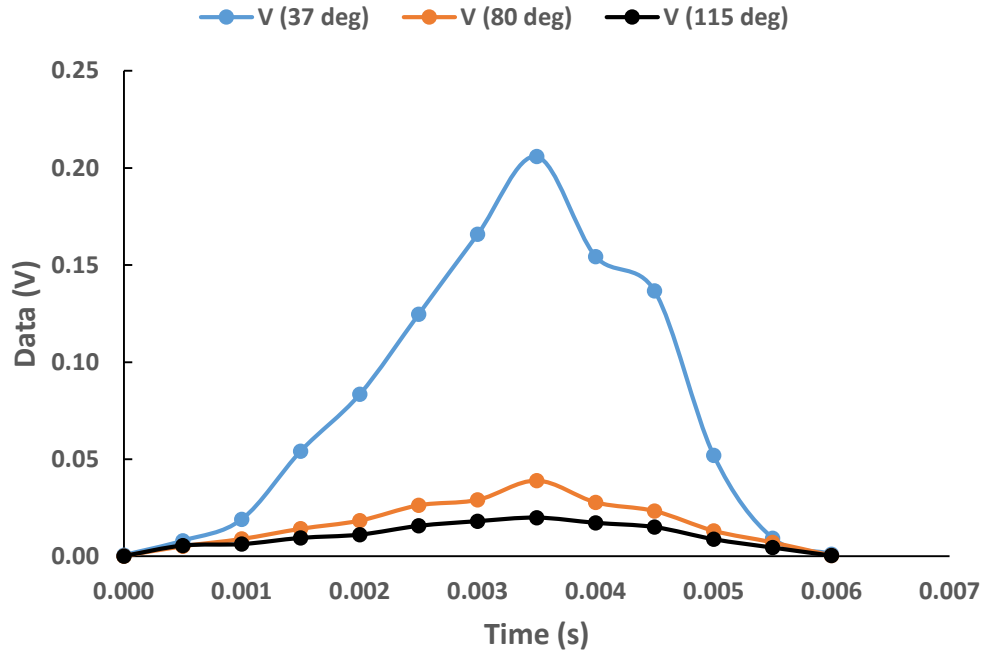


Figure 5.34 Photodiodes outputs vs. time of flight for a 220- μm droplet of nigrosine-to-toluene solution (1:1350)

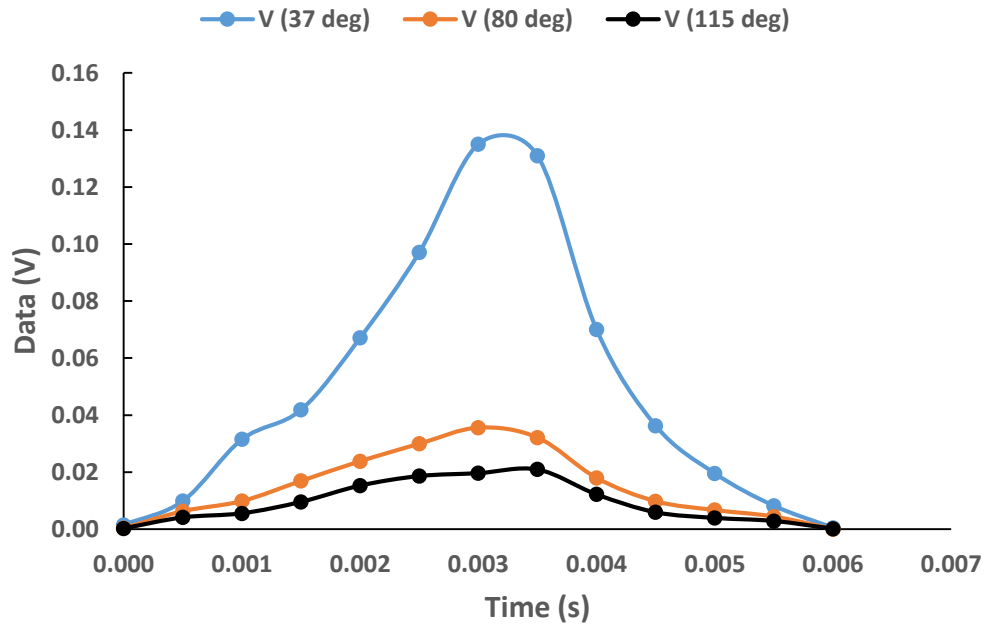


Figure 5.35 Photodiodes outputs vs. time of flight for a 220- μm droplet of nigrosine-to-toluene solution (1:800)

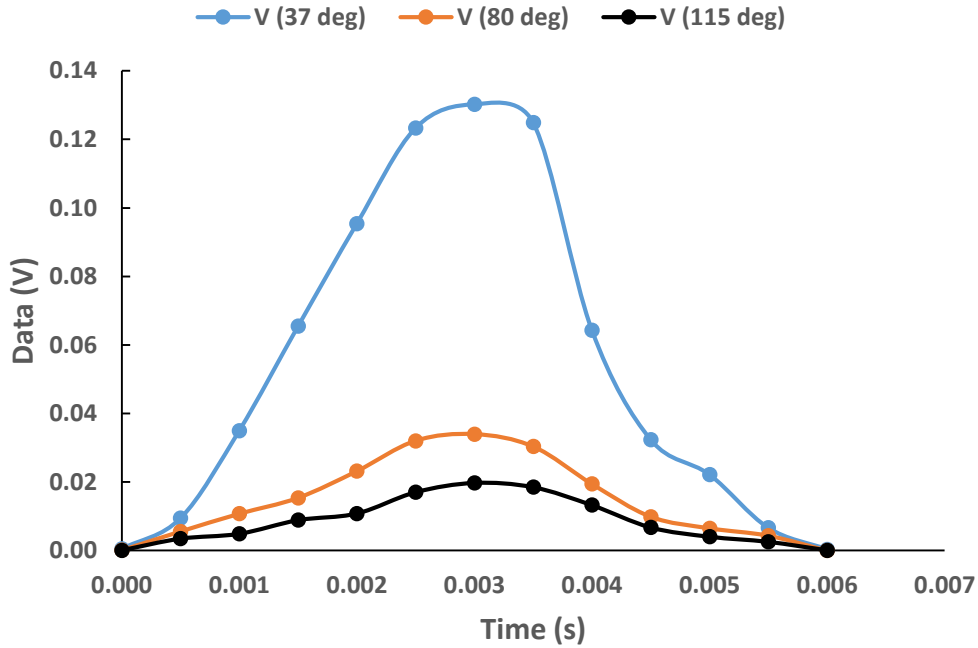


Figure 5.36 Photodiodes outputs vs. time of flight for a 220- μm droplet of nigrosine-to-toluene solution (1:800)

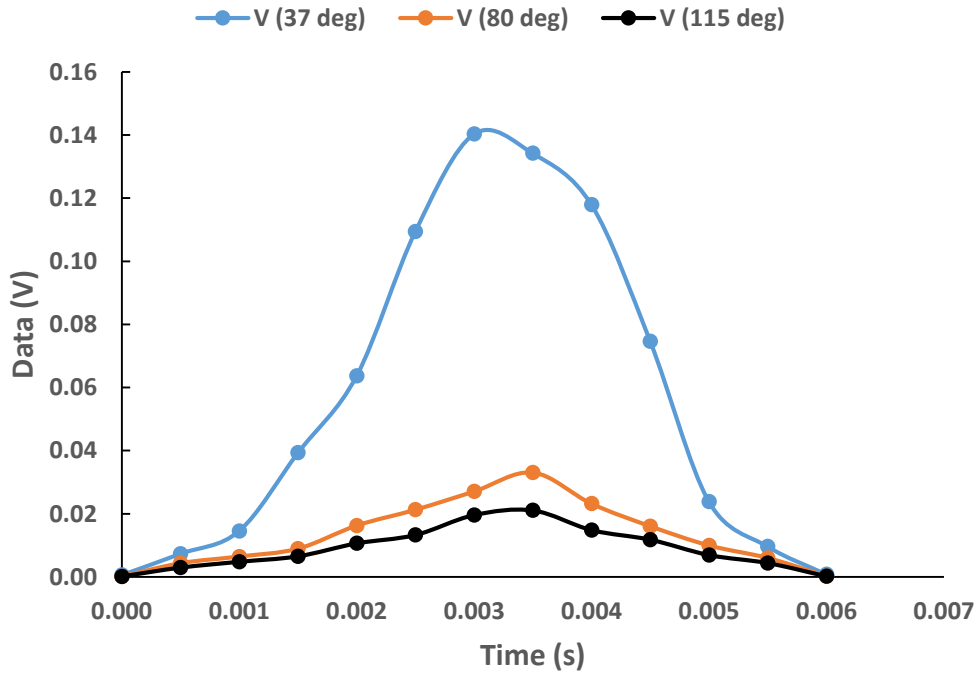


Figure 5.37 Photodiodes outputs vs. time of flight for a 220- μm droplet of nigrosine-to-toluene solution (1:800)

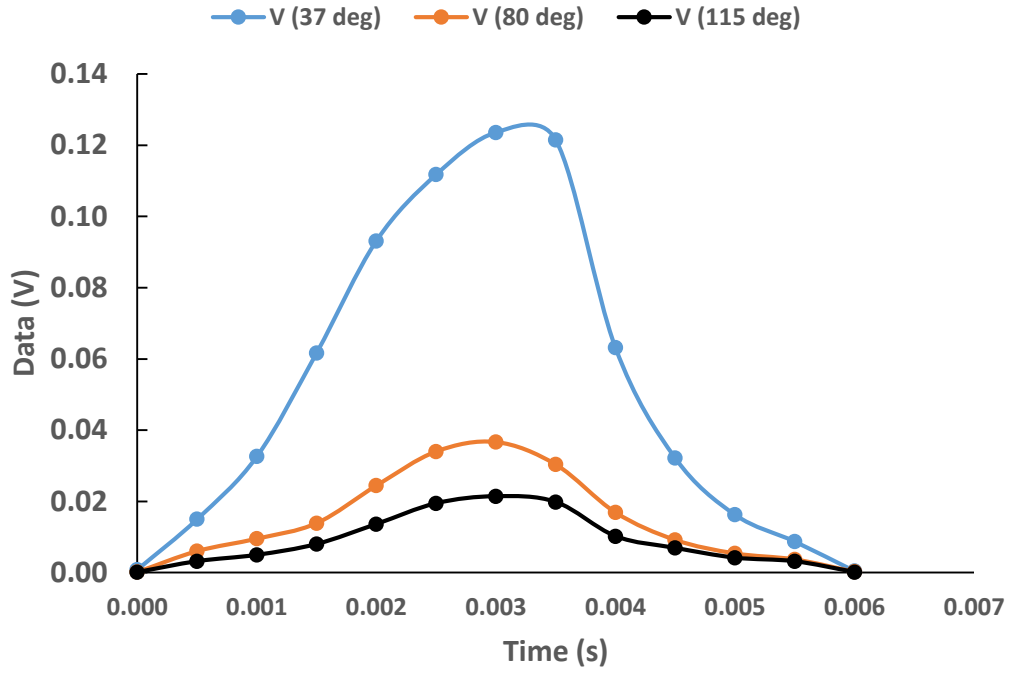


Figure 5.38 Photodiodes outputs vs. time of flight for a 220- μm droplet of nigrosine-to-toluene solution (1:800)

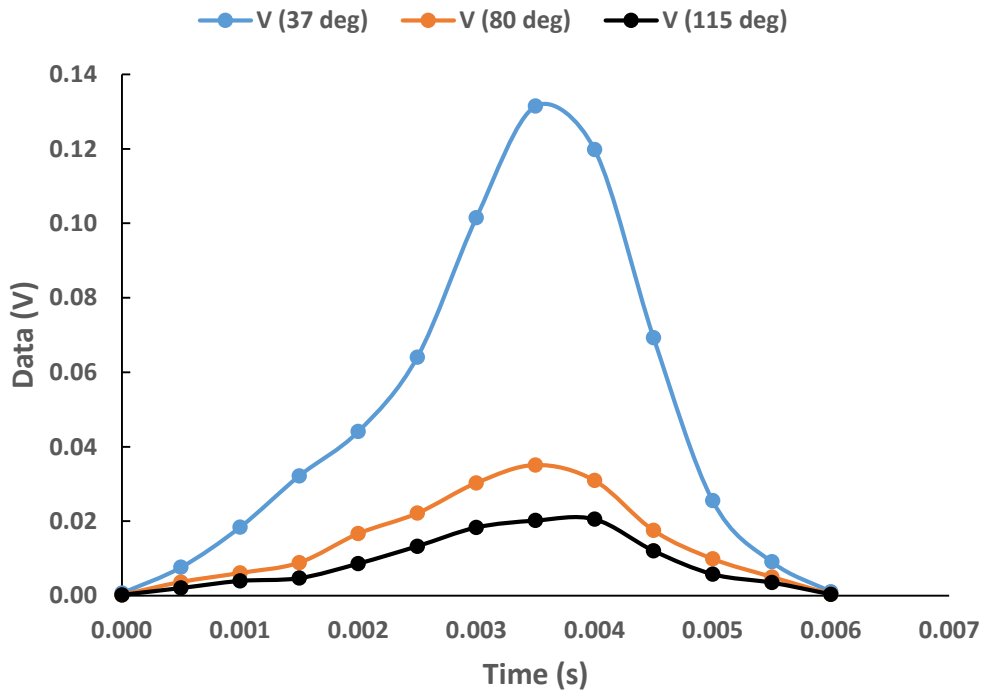


Figure 5.39 Photodiodes outputs vs. time of flight for a 220- μm droplet of nigrosine-to-toluene solution (1:800)

Table 5.2 Comparison of actual to predicted values of droplet diameter, d , $\kappa\kappa R$, and n for nigrosine-to-toluene solution

Fig. (Conc.)	d_{actual} ($\pm 10 \mu\text{m}$)	d_{pred} (μm)	$\kappa\kappa R_{act}$ ($\pm 9 \%$)	$\kappa\kappa R_{pred}$	n_{actual}	n_{pred}	Uncertainty (%)		
							d	$\kappa\kappa R$	n
5.30 (1:1350)	220	223.1	0.795	0.703	1.497	1.414	+1	-12	-6
5.31 (1:1350)	220	228.3	0.795	0.742	1.497	1.402	+4	-7	-6
5.32 (1:1350)	220	214.5	0.795	0.738	1.497	1.404	-2	-7	-6
5.33 (1:1350)	220	216.6	0.795	0.742	1.497	1.431	-2	-7	-4
5.34 (1:1350)	220	218.6	0.795	0.707	1.497	1.411	-1	-11	-6
5.35 (1:800)	220	214.1	1.104	1.201	1.497	1.454	-3	+9	-3
5.36 (1:800)	220	207.8	1.104	0.992	1.497	1.44	-6	-10	-4
5.37 (1:800)	220	217.7	1.104	1.194	1.497	1.428	-1	+8	-5
5.38 (1:800)	220	205.1	1.104	1.242	1.497	1.488	-7	+13	-1
5.39 (1:800)	220	210.2	1.104	1.185	1.497	1.457	-4	+7	-3
RMS Average							3.7	9.4	4.7

The predicted droplet diameters are not uniform in size as we can see in Tables 5.1 and 5.2. This is because the peak values of output voltages are different for the droplets as shown in their corresponding figures. The peak values of output voltages for smaller predicted droplets are obviously smaller than the ones for larger droplets.

5.4 Conclusions

In Tables 5.1 and 5.2, we can see our models have predicted d , n , and $\kappa\kappa R$ ($\kappa\pi d/\lambda$); however, we are interested to determine κ . Once the values of d and $\kappa\kappa R$ have been predicted, knowing that $\lambda = 0.532 \mu\text{m}$ in our case, we can simply determine κ . In order to accurately predict d , n , and $\kappa\kappa R$, it is recommended to position three photodiodes on one side and three photodiodes on the other

side of the beam at $\pm 37^\circ$, $\pm 80^\circ$, and $\pm 115^\circ$, and then record the scattered-light intensities of the particles by all six photodiodes simultaneously. If the particle passes through the center of the beam, then each pair of the photodiodes will record identical or near-identical outputs. In that case, use the average of the maximum outputs of each pair as the optimum value in mathematical models to iteratively solve for the unknowns indicated. If the particle passes through any other position of the beam, then compare the outputs of the three pairs of the photodiodes and choose the larger ones from each pair as the optimum values in the mathematical models to iteratively solve for the unknowns. Depending on the particle position in the beam, maximum outputs will always be recorded by the three photodiodes positioned on the same side. This is because the closer the particle to the photodiodes, the larger the solid angle, and thus the greater the photodiodes outputs.

Chapter 6 - Summary and Conclusions

In this dissertation, three main topics related to particulate-matter monitoring were investigated. The first topic dealt with calibration of low-cost particle sensors to be used for monitoring of indoor air quality in buildings. The second topic developed a single-particle detector for large, non-absorbing spherical particles so that particles could be sized independently of their refractive indices. The third topic determined the size and complex index of refraction of single particles simultaneously.

In the first topic, low-cost optical dust sensors GP2Y1010AU0F were calibrated using an aerodynamic particle sizer (APS) as a reference instrument. A container was built in a 3D printer for each sensor to make it air tight, protect it from ambient lights effects, and to connect it to the APS. Four sensors were connected in series with the APS and data were collected simultaneously on the downstream of a flow loop where the aerosol concentration was controlled. Sensors' performances were compared to each other as well as to the manufacturer's calibration data. Sensors were also exposed at two different positions in a controlled chamber to collect (1) indoor air data and (2) indoor air data with incense burning, and the results were compared to the calibration data. Initially, it was found that sensors' data were different from each other by $\pm 15\%$. This percentage was decreased to $\pm 5.9\%$ by adjusting the potentiometer on each sensor. Since the sensors work with light-scattering, it was found that their outputs were affected with the ambient lights levels causing uncertainties in the measured results. Sensors' data for indoor air (IA) with incense burning were affected by airflow. When connected in series to the APS with 5 L/min airflow passing through them, their data agreed with the calibration data; however, they did not agree when exposed to still air i.e., without airflow.

In order to use these sensors for monitoring of actual indoor air PM concentration, each sensor should be calibrated with a reliable PM instrument. During the calibration, these sensors will be exposed to the same amount of airflow as will be passing through the reference instrument, and the calibration curves will be developed accordingly. Therefore, in order to measure the indoor air concentration accurately, these sensors should be adjusted to an air-circulation mechanism preferably equal to the same amount of airflow that was passing through them during the calibration.

In the second topic, we modified the Gaussian incident beam profile to a diamond-shaped beam to eliminate the effect of the Gaussian intensity distribution so that the beam transit time of a particle passing through it can determine the true incident intensity for the scattering of the particle. Also using the Mie scattering program, we demonstrated the differential-scattering cross-section of spherical particles merged at $37 \pm 5^\circ$ for four different real refractive indices. This indicates that a differential-scattering cross-section is independent of the real refractive index at the mentioned scattering angle. Combining the modified Gaussian incident beam profile with detection of scattered light near $37 \pm 5^\circ$, we demonstrated a refractive-index independent measurement of single-spherical particles as they pass through the beam.

This system can be used to size any type of spherical particle in a wide range of diameters (1-1000 μm) with an uncertainty less than 10% for particles greater than 10 μm in diameter. For particles smaller than 10 μm , the uncertainty is greater than 10% but the method still has some merit down to 1 micron. This method can also be used to improve low-cost sensor technology by adding size information into concentration measurements. Then the low-cost sensor will be able to determine particle size within a similar uncertainty range as a more expensive instrument.

To validate the theory, particles, 500 μm in diameter, of two different types (glass beads, and barium titanate glass compound) with refractive indices of 1.5 and 1.9, respectively, were experimentally evaluated. It was found that peak scattered light for these two different particles was identical at a 37° scattering angle, and hence the particles were sized within $\pm 10\%$ uncertainty, which agreed well with our predicted uncertainty values for this size.

In order to accurately size any non-absorbing spherical particle, regardless of its type and material (chemical composition), this device would be a perfect choice. Additionally, this research is useful in a variety of applications such as designing new PM sensors with low-cost and accurate particle-sizing capability, sorting poly-disperse solid particles to get highly mono-disperse particles out of them, and sizing fuel particles that can be used in advanced nuclear reactors. Finally, it can also help sort microspheres and reduce production costs.

In the third topic, we have developed a sensor which determines the size and complex index of refraction of single particles simultaneously by measuring the scattered-light intensity of particles at three different scattering angles, i.e., $37 \pm 5^\circ$, $80 \pm 5^\circ$, and $115 \pm 5^\circ$.

Considering the scattered-light intensity at three angles, we have developed three mathematical models so that we could solve for the three unknowns, i.e., particle size, and real and imaginary components of the refractive index. In Chapter 4, we showed the differential-scattering cross-section was only independent of the real part of refractive index at $37 \pm 5^\circ$; however, in case of absorbing particles, it depends on the imaginary part as shown in Figures 5.1 – 5.4. In Chapter 5, we modified the mathematical model that was developed for $37 \pm 5^\circ$ by considering the effect of the imaginary component. At 115° , particles can be sized independently of the imaginary component; however, at 80° , it depends on both the real and the imaginary components. Although this dependence agreed at several angles, we selected 80° as an optimum angle because the

variation of the differential-scattering cross-section at this angle was more consistent compared to the other scattering angles, which is also confirmed in Figure 4.4.

To validate the third topic, we conducted some experiments by simultaneously measuring the scattered-light intensities of 300 μm in diameter droplets of nigrosine solution-to-water at the three scattering angles mentioned above. Then the peak scattered intensities and total time of flights were used in the models to predict the diameter, and the real and imaginary parts of the refractive indices. Initially, we conducted a prerequisite experiment to determine the imaginary part of the refractive index. Since a small amount of nigrosine was dissolved in water, the real component of the refractive index of the solution remained the same as the refractive index of water ($n = 1.33$). Once we had the known values for the diameter, and real and imaginary parts of the refractive index, we compared the actual values to the predicted values obtained by our models. We found, on average, the uncertainties were $\pm 5.72\%$, $\pm 0.97\%$, and $\pm 17.98\%$ for diameter, real, and imaginary parts of the refractive index, respectively.

We conducted the same experiments on 220- μm -in-diameter droplets of nigrosine–toluene solution. Since a small amount of nigrosine was dissolved in toluene, the real part of the refractive index of the solution remained the same as the refractive index of toluene ($n = 1.497$). Considering known values of the diameter, and the real and imaginary components, we compared our predicted values to the actual values. We found, on average, the uncertainties were $\pm 3.7\%$, $\pm 4.7\%$, and $\pm 9.4\%$ for diameter, real, and imaginary parts, respectively.

The third topic of our research can be useful in a variety of applications such as designing new PM sensors with low-cost, accurate particle sizing, and complex refractive index determination capability, sorting and identifying the type and material of poly-disperse solid particles to get highly mono-disperse particles of known material out of them and reducing their

production costs, detection and identification of particulate matter in bleed air in aircrafts, as well as the exhaust of internal combustion engines.

References

- Aerodynamic Particle Sizer, Model 3321. Retrieved from http://www.tsi.com/uploadedFiles/_Site_Root/Products/Literature/Brochures/3321%20Operation%20brochure%20A4-5001469_WEB.pdf
- Austin, E., Novosselov, I., Seto, E., & Yost, M. G. (2015). Laboratory Evaluation of the Shinyei PPD42NS Low-Cost Particulate Matter Sensor. *PLoS One*, *10*(9), e0137789. doi:10.1371/journal.pone.0137789
- Baron, P. A., & Willeke, K. (2001). *Aerosol measurement: principles, techniques, and applications*: Wiley.
- Bartl, P., Völkl, C., & Kaiser, M. (2008). Chemical characterization of polyol ester aviation lubricant residues. *Journal of Synthetic Lubrication*, *25*(1), 1-16. doi:10.1002/jsl.43
- Baumgardner, D., Dye, J. E., Gandrud, B., Barr, K., Kelly, K., & Chan, K. R. (1996). Refractive indices of aerosols in the upper troposphere and lower stratosphere. *Geophysical Research Letters*, *23*(7), 749-752. doi:10.1029/96GL00707
- Budde, M., El Masri, R., Riedel, T., & Beigl, M. (2013). Enabling low-cost particulate matter measurement for participatory sensing scenarios. 1-10. doi:10.1145/2541831.2541859
- Cooper, C. D., & Alley, F. C. (2010). *Air Pollution Control: A Design Approach, Fourth Edition*: Waveland Press.
- Ebert, M., Weinbruch, S., Hoffmann, P., & Ortner, H. M. (2004). The chemical composition and complex refractive index of rural and urban influenced aerosols determined by individual particle analysis. *Atmospheric Environment*, *38*(38), 6531-6545. doi:<https://doi.org/10.1016/j.atmosenv.2004.08.048>
- Eckels, S. J., Jones, B., Mann, G., Mohan, K. R., & Weisel, C. P. (2014). Aircraft Recirculation Filter for Air-Quality and Incident Assessment. *Journal of Aircraft*, *51*(1), 320-326. doi:10.2514/1.C032458
- Eidhammer, T., Montague, D. C., & Deshler, T. (2008). Determination of index of refraction and size of supermicrometer particles from light scattering measurements at two angles. *Journal of Geophysical Research: Atmospheres*, *113*(D16), n/a-n/a. doi:10.1029/2007JD009607
- Gao, R. S., Perring, A. E., Thornberry, T. D., Rollins, A. W., Schwarz, J. P., Ciciora, S. J., & Fahey, D. W. (2013). A High-Sensitivity Low-Cost Optical Particle Counter Design. *Aerosol Science and Technology*, *47*(2), 137-145. doi:10.1080/02786826.2012.733039
- Gorai, A. K., Tuluri, F., & Tchounwou, P. B. (2014). A GIS Based Approach for Assessing the Association between Air Pollution and Asthma in New York State, USA. *11*(5), 4845.

GP2Y1001AU. Retrieved from https://www.sparkfun.com/datasheets/Sensors/gp2y1010au_e.pdf

Gucker, F. T., O'Konski, C. T., Pickard, H. B., & Pitts, J. N. (1947). A Photoelectronic Counter for Colloidal Particles1. *Journal of the American Chemical Society*, 69(10), 2422-2431. doi:10.1021/ja01202a053

HEE-SIEW, H. (2014). System and method for converting optical diameters of aerosol particles to mobility and aerodynamic diameters. In: Google Patents.

Heinson, Y. W., Maughan, J. B., Ding, J., Chakrabarti, A., Yang, P., & Sorensen, C. M. (2016). Q-space analysis of light scattering by ice crystals. *Journal of Quantitative Spectroscopy and Radiative Transfer*, 185, 86-94. doi:<https://doi.org/10.1016/j.jqsrt.2016.08.021>

Hering, S. V., Stolzenburg, M. R., Quant, F. R., Oberreit, D. R., & Keady, P. B. (2005). A Laminar-Flow, Water-Based Condensation Particle Counter (WCPC). *Aerosol Science and Technology*, 39(7), 659-672. doi:10.1080/02786820500182123

Hinds, W. C. (1999). *Aerosol Technology* (Second ed.). United States of America.

Hirleman Edwin D, W. S. L. K. (1980). Multiple ratio single particle counter. Germany.

Holstius, D. M., Pillarisetti, A., Smith, K. R., & Seto, E. (2014). Field calibrations of a low-cost aerosol sensor at a regulatory monitoring site in California. *Atmospheric Measurement Techniques*, 7(4), 1121-1131. doi:10.5194/amt-7-1121-2014

Hu, H., Li, X., Zhang, Y., & Li, T. (2006). Determination of the refractive index and size distribution of aerosol from dual-scattering-angle optical particle counter measurements. *Applied Optics*, 45(16), 3864-3870. doi:10.1364/AO.45.003864

Johnson, K. K., Bergin, M. H., Russell, A. G., & Hagler, G. S. W. (2016). Using Low Cost Sensors to Measure Ambient Particulate Matter Concentrations and On-Road Emissions Factors. *Atmospheric Measurement Techniques Discussions*, 1-22. doi:10.5194/amt-2015-331

Jones, B. W., Amiri, S. N., Roth, J. W., & Hosni, M. H. (2017). *The Nature of Particulates in Aircraft Bleed Air Resulting from Oil Contamination* Paper presented at the ASHRAE Winter Conference.

Kelly, K. E., Whitaker, J., Petty, A., Widmer, C., Dybwad, A., Sleeth, D., . . . Butterfield, A. (2017). Ambient and laboratory evaluation of a low-cost particulate matter sensor. *Environ Pollut*, 221, 491-500. doi:10.1016/j.envpol.2016.12.039

Kolgotin, A., Müller, D., Chemyakin, E., & Romanov, A. J. E. W. o. C. (2016). Perspectives of the Explicit Retrieval of the Complex Refractive Index of Aerosols from Optical Data Taken with Lidar. *119*, 17016.

- Laven, P. (2006). MiePlot. Retrieved from <http://www.philiplaven.com/mieplot.htm#Download%20MiePlot>
- Laven, P. (2010). *Separating diffraction from scattering: The million-dollar challenge* (Vol. 4).
- Leander Molter, F. M. (1998). Device and method for measuring a particle flow in a fluid. (US5815265A).
- Mallik, S. (2014). *A Small Airborne Particulate Matter Sensor Using a Parabolic Mirror*. (Masters), Raleigh, North Carolina,
- Mann, G. W., Eckels, S. J., & W. Jones, B. (2014). Analysis of particulate size distribution and concentrations from simulated jet engine bleed air incidents. *HVAC&R Research*, 20(7), 780-789. doi:10.1080/10789669.2014.950922
- Mie, G. (1908). Beiträge zur Optik trüber Medien, speziell kolloidaler Metallösungen. *Annalen der Physik*, 330(3), 377-445. doi:10.1002/andp.19083300302
- Model 3080-Series Electrostatic Classifiers. Retrieved from http://www.tsi.com/uploadedFiles/Site_Root/Products/Literature/Spec_Sheets/3080.pdf
- Mordas, G., Kulmala, M., Petäjä, T., Aalto, P. P., Matulevicius, V., Grigoraitis, V., . . . Hämeri, K. (2005). Design and performance characteristics of a condensation particle counter UF-02proto. *Boreal environment research*, 10(6), 543-552.
- Nandasena, S., Wickremasinghe, A. R., & Sathiakumar, N. (2012). Respiratory health status of children from two different air pollution exposure settings of Sri Lanka: A cross-sectional study. 55(12), 1137-1145. doi:doi:10.1002/ajim.22020
- Optical Particle Sizer Model 3330. Retrieved from http://www.tsi.com/uploadedFiles/Site_Root/Products/Literature/Spec_Sheets/3330_5001323_Web.pdf
- Pfeifer, S., Birmili, W., Schladitz, A., Müller, T., Nowak, A., & Wiedensohler, A. (2014). A fast and easy-to-implement inversion algorithm for mobility particle size spectrometers considering particle number size distribution information outside of the detection range. *Atmos. Meas. Tech.*, 7(1), 95-105. doi:10.5194/amt-7-95-2014
- plantower-pms1003-manual_v2-5. Retrieved from http://www.aqmd.gov/docs/default-source/aq-spec/resources-page/plantower-pms1003-manual_v2-5.pdf?sfvrsn=2
- Pope , C. A. I., Ezzati , M., & Dockery , D. W. (2009). Fine-Particulate Air Pollution and Life Expectancy in the United States. *New England Journal of Medicine*, 360(4), 376-386. doi:10.1056/NEJMsa0805646

- Ren, Y., Qi, H., Chen, Q., Ruan, L., & Tan, H. (2015). Simultaneous retrieval of the complex refractive index and particle size distribution. *Optics Express*, 23(15), 19328-19337. doi:10.1364/OE.23.019328
- Ren, Y., Qi, H., Yu, X., & Ruan, L. (2017). A forward-angle-scattering method for the determination of optical constants and particle size distribution by collimated laser irradiation. *Optics Communications*, 389, 258-264. doi:<https://doi.org/10.1016/j.optcom.2016.12.060>
- Roth, J. (2015). *Bleed Air Oil Contamination Particulate Characterization*. (Master), Kansas State University, Manhattan, KS United States.
- Sorensen, C. M. (2013). Q-space analysis of scattering by particles: A review. *Journal of Quantitative Spectroscopy and Radiative Transfer*, 131, 3-12. doi:<https://doi.org/10.1016/j.jqsrt.2012.12.029>
- Specification sheet of PPD42NS. Retrieved from http://www.shinyei.co.jp/stc/optical/main_ppd42ns_e.html
- Sun, X., Tang, H., & Dai, J. (2007). Retrieval of particle size distribution in the dependent model using the moment method. *Optics Express*, 15(18), 11507-11516. doi:10.1364/OE.15.011507
- Tianhua, L., & Ying, W. (2014). Design of indoor dust concentration monitor based on light scattering detection method. *Scientific research and essays*, 9(9), 321-324.
- Underwood, E. (2017). The polluted brain. *Science*, 355(6323), 342-345. doi:10.1126/science.355.6323.342
- van Netten, C. (1999). Multi-elemental analysis of jet engine lubricating oils and hydraulic fluids and their implication in aircraft air quality incidents. *Sci Total Environ*, 229(1-2), 125-129.
- van Netten, C. (2005). Aircraft Air Quality Incidents, Symptoms, Exposures and Possible Solutions. In M. Hocking (Ed.), *Air Quality in Airplane Cabins and Similar Enclosed Spaces* (pp. 193-210). Berlin, Heidelberg: Springer Berlin Heidelberg.
- van Netten, C., & Leung, V. (2000). Comparison of the constituents of two jet engine lubricating oils and their volatile pyrolytic degradation products. *Appl Occup Environ Hyg*, 15(3), 277-283. doi:10.1080/104732200301593
- van Netten, C., & Leung, V. (2001). Hydraulic fluids and jet engine oil: pyrolysis and aircraft air quality. *Arch Environ Health*, 56(2), 181-186. doi:10.1080/00039890109604071

- Volckens, J., & Peters, T. M. (2005). Counting and particle transmission efficiency of the aerodynamic particle sizer. *Journal of Aerosol Science*, 36(12), 1400-1408. doi:<https://doi.org/10.1016/j.jaerosci.2005.03.009>
- Waez, M. S., Eckels, S. J., & Sorensen, C. M. (2018). A refractive-index and position-independent single-particle detector for large, nonabsorbing, spherical particles. *Aerosol Science and Technology*, 1-8. doi:10.1080/02786826.2018.1524133
- Wang, G., Chakrabarti, A., & Sorensen, C. M. (2015). Effect of the imaginary part of the refractive index on light scattering by spheres. *J Opt Soc Am A Opt Image Sci Vis*, 32(7), 1231-1235. doi:10.1364/josaa.32.001231
- Wang, X., Chancellor, G., Evenstad, J., Farnsworth, J. E., Hase, A., Olson, G. M., . . . Agarwal, J. K. (2009). A Novel Optical Instrument for Estimating Size Segregated Aerosol Mass Concentration in Real Time. *Aerosol Science and Technology*, 43(9), 939-950. doi:10.1080/02786820903045141
- Wang, Y. (2014). *Airborne Particle Sensing with Micro-optics*. (Masters), Raleigh, North Carolina,
- Wang, Y., Li, J., Jing, H., Zhang, Q., Jiang, J., & Biswas, P. (2015). Laboratory Evaluation and Calibration of Three Low-Cost Particle Sensors for Particulate Matter Measurement. *Aerosol Science and Technology*, 49(11), 1063-1077. doi:10.1080/02786826.2015.1100710
- Winder, C., & Balouet, J. (2001). *Aircrew Exposure to Chemicals in Aircraft: Symptoms of Irritation and Toxicity* (Vol. 17).
- Winder, C., & Balouet, J. (2002). *The Toxicity of Commercial Jet Oils* (Vol. 89).
- Ye, M., Wang, S., Lu, Y., Hu, T., Zhu, Z., & Xu, Y. (1999). Inversion of particle-size distribution from angular light-scattering data with genetic algorithms. *Applied Optics*, 38(12), 2677-2685. doi:10.1364/AO.38.002677
- Zarzana, K. J., Cappa, C. D., & Tolbert, M. A. (2014). Sensitivity of Aerosol Refractive Index Retrievals Using Optical Spectroscopy. *Aerosol Science and Technology*, 48(11), 1133-1144. doi:10.1080/02786826.2014.963498
- Zhu, X., Shen, J., Wang, Y., Guan, J., Sun, X., & Wang, X. (2011). *The reconstruction of particle size distributions from dynamic light scattering data using particle swarm optimization techniques with different objective functions* (Vol. 43).

Appendix A - Experimental Data at 37° Scattering Angle

In this section we show more experimental data related to the results in Chapter 4 to further confirm the consistency and repeatability of our measurements at a 37° scattering angle.

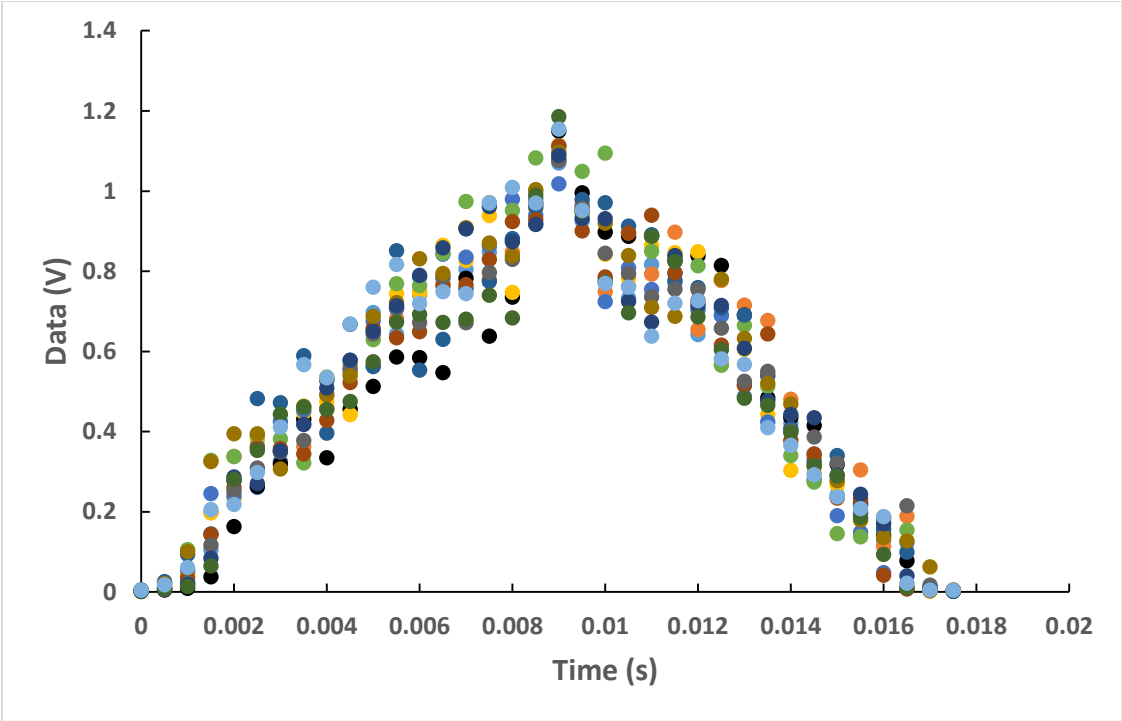


Figure A.1 Photodiodes outputs for 13 glass beads 500 μm in diameter

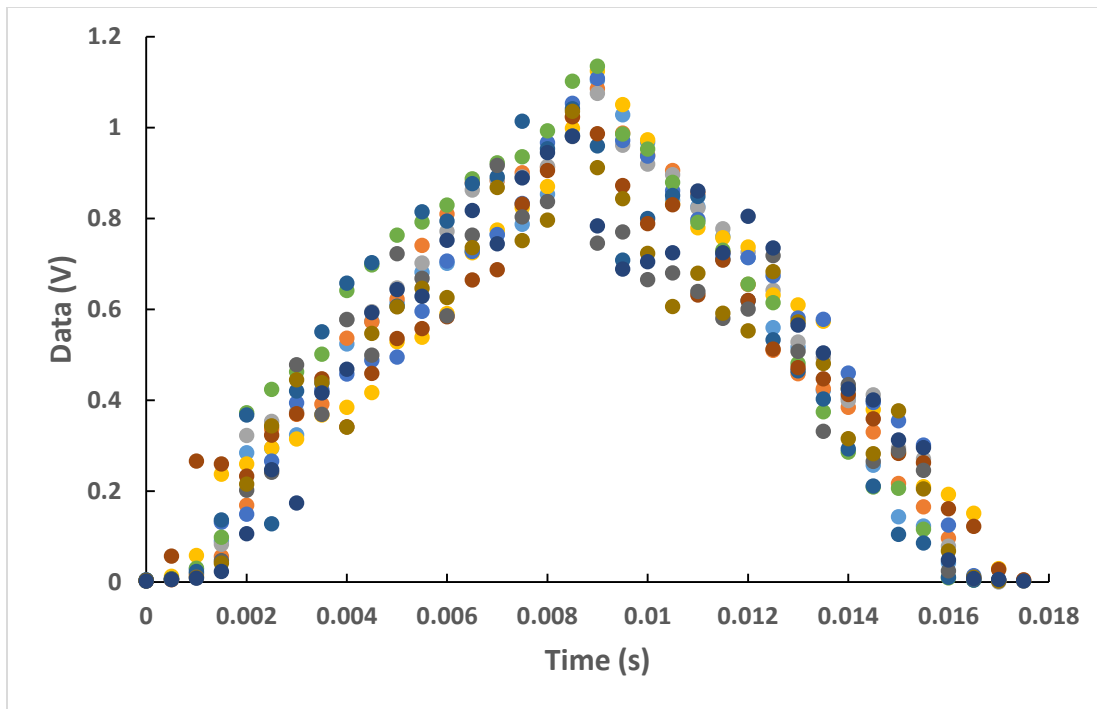


Figure A.2 Photodiodes outputs for 11 glass beads 500 μm in diameter

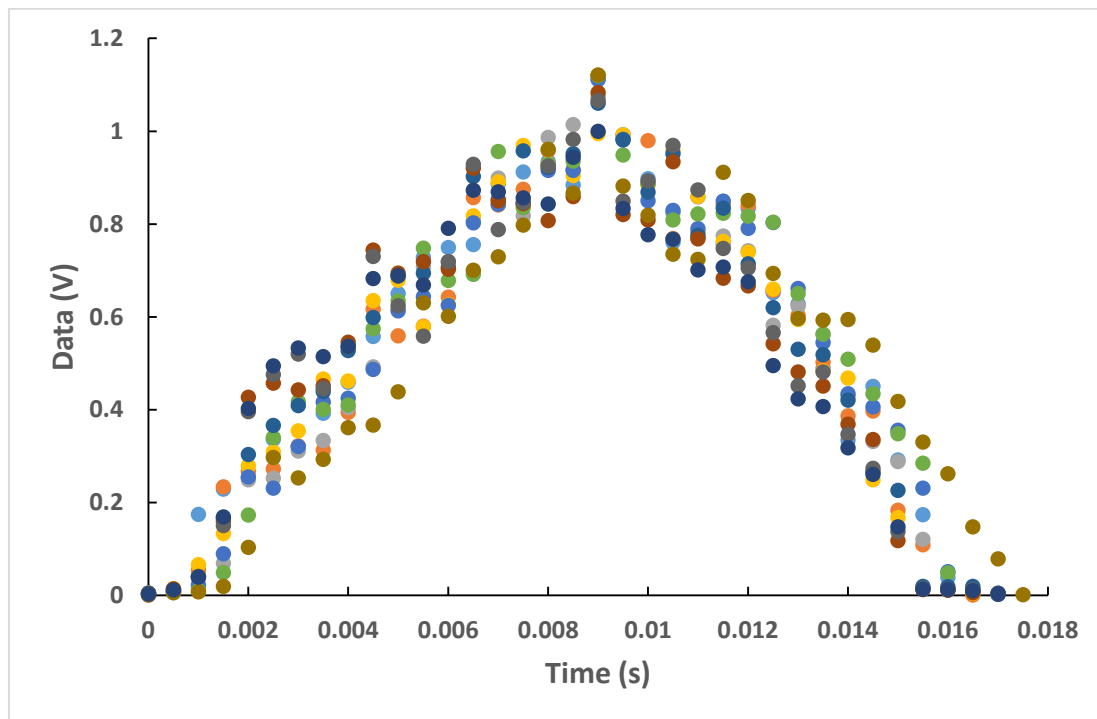


Figure A.3 Photodiodes outputs for 11 barium titanate glass compound (BTGC) beads 500 μm in diameter

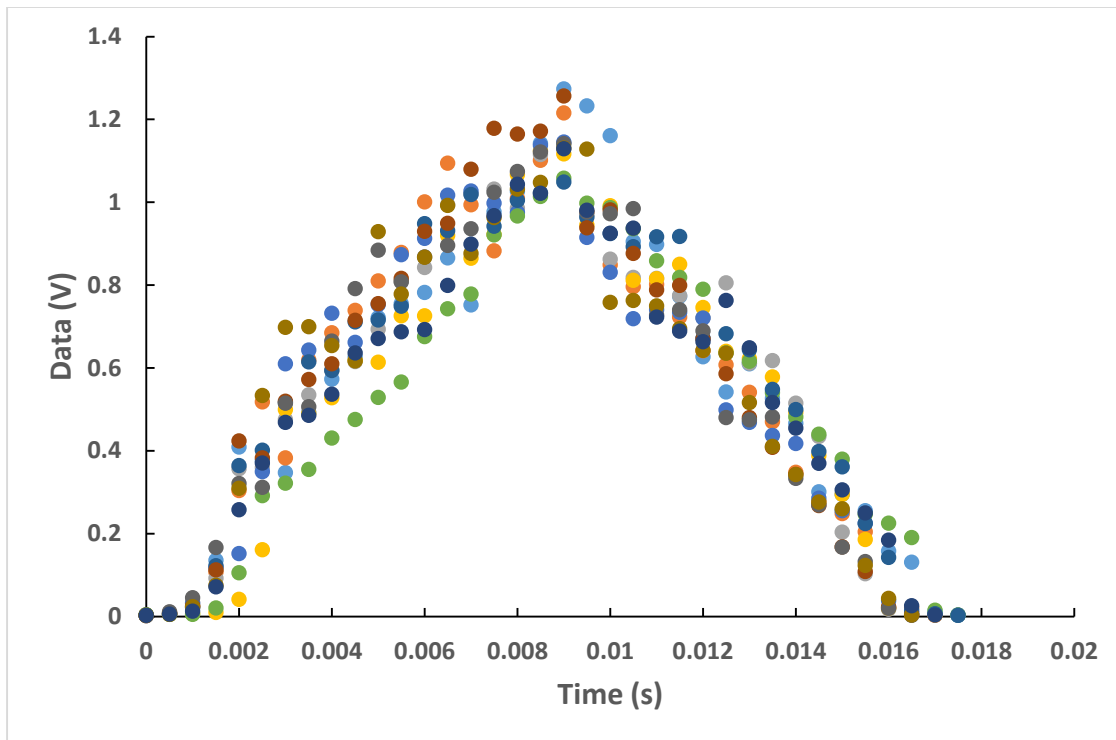


Figure A.4 Photodiodes outputs for 11 barium titanate glass compound (BTGC) beads 500 μm in diameter

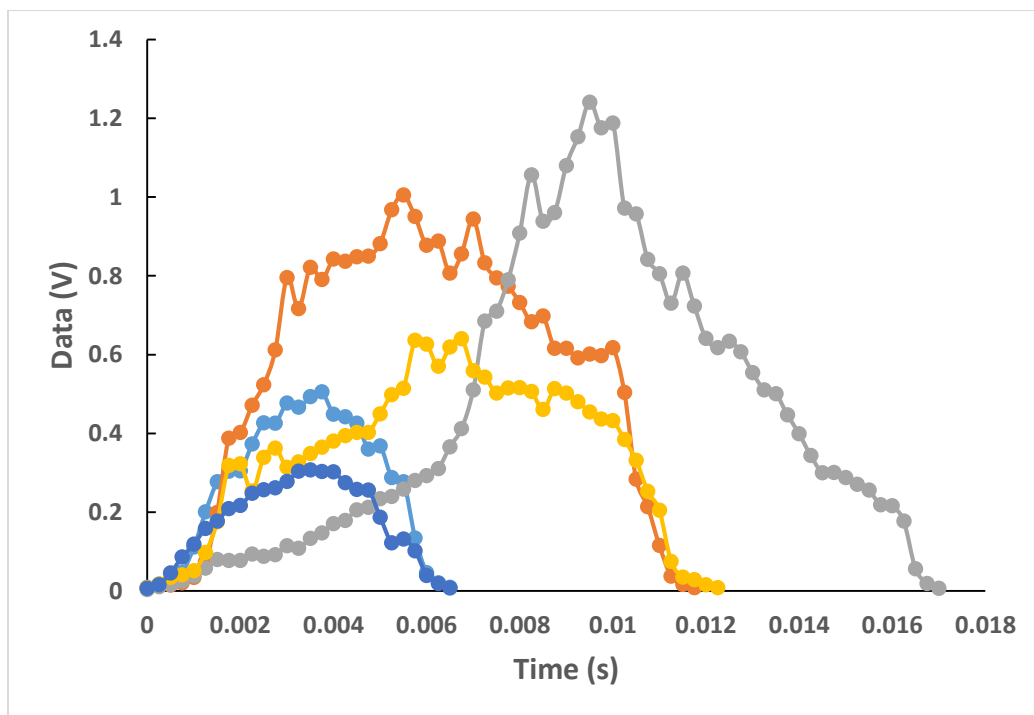


Figure A.5 Experimental data for 500- μm barium titanate glass compound (BTGC) beads at five different positions in the beam

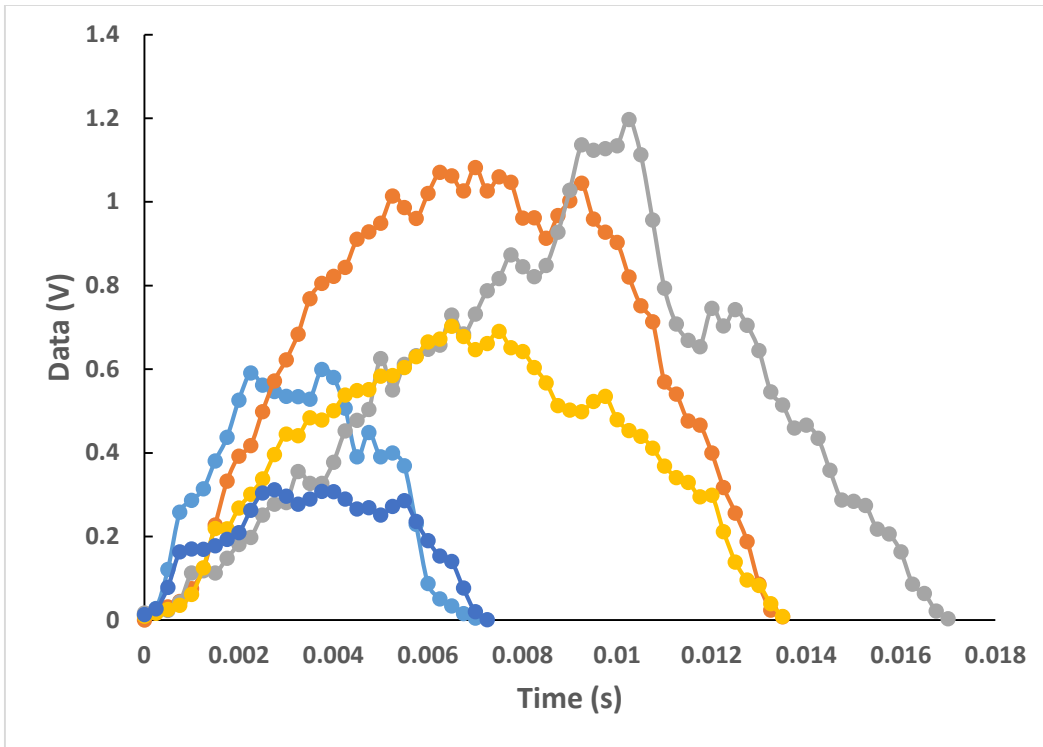


Figure A.6 Experimental data for 500- μm glass beads at five different positions in the beam

Appendix B - Permission from the American Association for Aerosol

Research to Reproduce Figures 2.4 and 2.5





Luba Slabyj <astoffice.luba@gmail.com>

Mon 6/17/2019 4:21 PM

To:  Mir Seliman Waez 



 Reply all | 

Mir Seliman Waez -

Please be advised you have permission to use the following:

1. Figure 2 from: <https://www.tandfonline.com/doi/full/10.1080/02786820500182123>
2. Figure 1 from: <https://www.tandfonline.com/doi/full/10.1080/02786826.2012.733039>

As part of the caption for each figure, you must include the following sentence: *Reproduced with permission from The American Association for Aerosol Research.*

Also, please ensure the article is properly cited on your references page.

If you have additional questions, please let me know.

Best,
Catherine Wenschlag

for:
Luba Slabyj
Aerosol Science & Technology Editorial Office
astoffice.luba@gmail.com

...

Appendix C - TSI Confirmation to Reuse Figures

Using Figures in my Dissertation



Elzey, Sherrie <sherrie.elzey@tsi.com>

Fri 6/14/2019 2:36 PM



Hi Seliman,
Yes, as long as you reference it that should be fine.

Good luck as you finish your degree!

Regards,
Sherrie

Sherrie Elzey, Ph.D. | Technical Sales Specialist
TSI Incorporated | Particle Instruments
Mobile: 651-208-2347 (phone or text) | sherrie.elzey@tsi.com

www.tsi.com



Great, thank you so much!

Thank you!

Thanks!

Report inappropriate text



Mir Seliman Waez

Fri 6/14/2019 12:19 PM

To: Elzey, Sherrie <sherrie.elzey@tsi.com> ↗



Reply all | ▾

Dear Sherrie,

I would like to use some figures from TSI instrument manuals into my dissertation and reference the TSI manuals. Is it Ok if I do that, or you would give me permission for using them?

Thanks,

Seliman